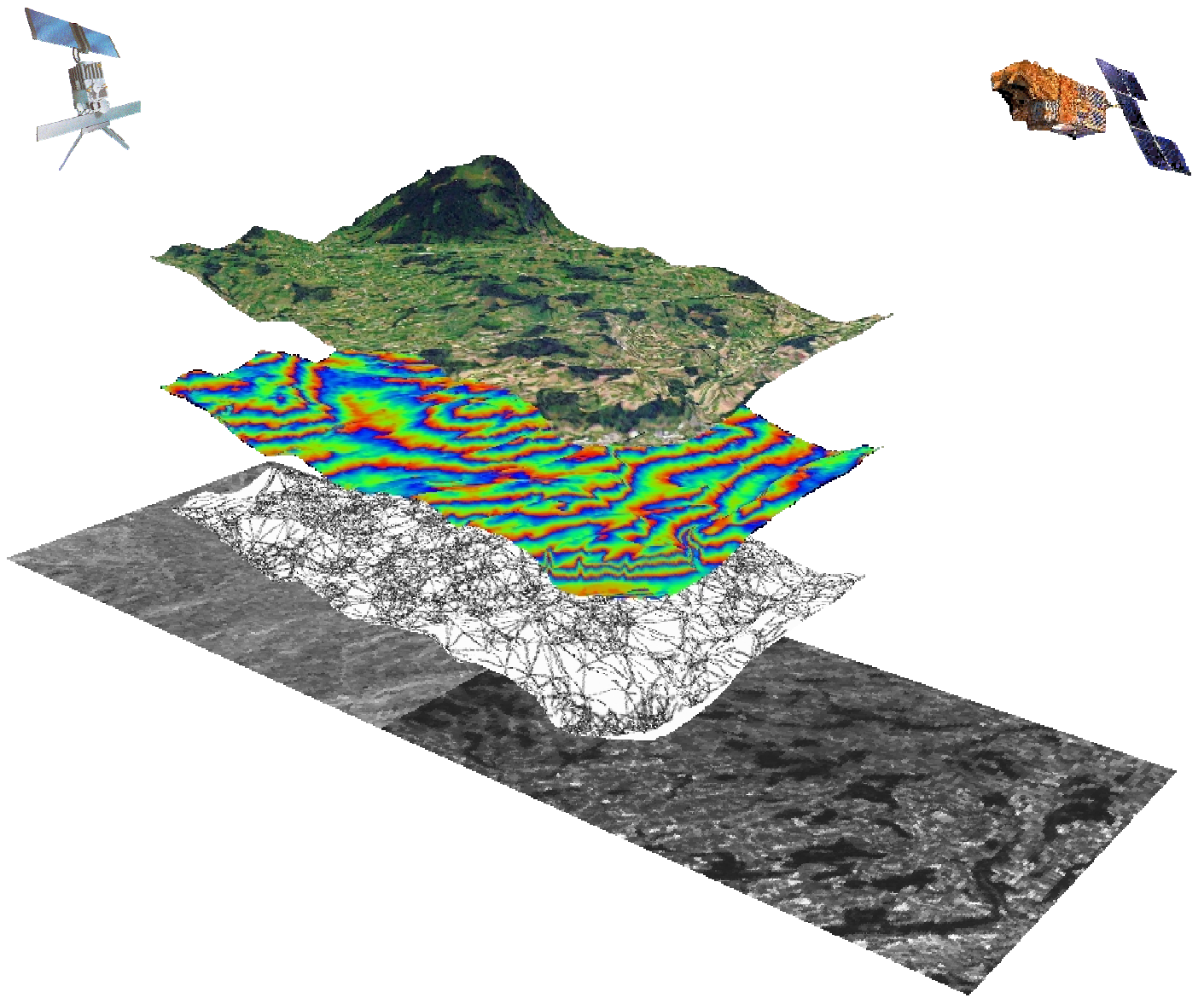# FUSION OF SPACEBORNE STEREO-OPTICAL AND INTERFEROMETRIC SAR DATA FOR DIGITAL TERRAIN MODEL GENERATION

Marc W. Honikel

IGP Mitteilung Nr. 76

Honikel, Marc Wolfgang

       Fusion of Spaceborne Stereo-Optical and Interferometric SAR Data

       for Digital Terrain Model Generation

DISS. ETH Nr. 14636

FUSION OF SPACEBORNE STEREO-OPTICAL AND INTERFEROMETRIC SAR DATA FOR DIGITAL TERRAIN MODEL GENERATION

ABHANDLUNG

zur Erlangung des Titels

DOKTOR DER TECHNISCHEN WISSENSCHAFTEN

der

EIDGENÖSSISCHEN TECHNISCHEN HOCHSCHULE ZÜRICH

Vorgelegt von

MARC WOLFGANG HONIKEL

Dipl.-Ing. Elektrotechnik, Universität Fridericiana zu Karlsruhe

geboren am 23. Februar 1969

von Deutschland

Angenommen auf Antrag von:

Prof. Dr. Armin Grün, Institut für Geodäsie und Photogrammetrie, ETH Zürich, Referent
Prof. Dr. Ian Dowman, Department of Geomatic Engineering, University College London, Koreferent

2002

ACKNOWLEDGMENT

CONTENTS

CHAPTER 5

CHAPTER 6

CHAPTER 7

KURZFASSUNG

Für die satellitengestützte Messung von digitalen Geländemodellen (DGMs) bietet sich sowohl die photogrammetrische Auswertung eines Bildpaares als auch die Radar Interferometrie (InSAR) an. Mit der photogrammetrischen Methode, bis heute überwiegend mit den französischen SPOT Satelliten durchgeführt, erreicht man im Normalfall DGM Genauigkeiten von 10m. Da bei SPOT die Aufnahmen bei zwei verschiedenen Überflügen gemacht werden (repeat pass), entstehen durch Veränderungen oftmals aber Probleme bei der Punktbestimmung und dadurch inakzeptabel grosse Messlücken im DGM. Wolkenbehang macht vielerorts eine Messung ganz unmöglich. Auf der anderen Seite können interferometrische SAR Messungen unabhängig von Wolkenbehang oder Tageszeit durchgeführt werden. Die Bilder der europäischen Fernerkundungssatelliten ERS-1/2 stellen hinsichtlich Verfügbarkeit, Anzahl und Genauigkeit der Messungen und Automatisierung (und damit Preis) eine echte Alternative zur traditionellen photogrammetrischen Geländemodellgenerierung in diesem Massstab dar. Laufzeitmessverfahren wie InSAR haben jedoch einige schwerwiegende Nachteile, die im wesentlichen aus der Aufnahmegeometrie, der notwendigen Genauigkeit bei der Bestimmung der Aufnahmeposition und der repeat pass Konstellation entstehen. Aus diesen Gründen erreichen interferometrische DGMs nur selten höhere absolute Genauigkeiten als die mit optischen Systemen gemessenen DGMs.

Die vorliegende Arbeit behandelt die Fusion von optischen und InSAR Daten zur DGM Generierung. Es wird untersucht, wie und inwieweit sich bereits bestehende SPOT DGMs eignen, um mit interferometrischen Messungen fusioniert zu werden. Zwei Optionen und dementsprechend zwei Geometrien bieten sich hierfür an: zum einen die Fusion während der interferometrischen Prozessierung in der SAR Bildgeometrie, zum anderen die auf Produktebene, dem DGM. In beiden Fällen werden die Daten zur Fusion zunächst in eine gemeinsame Geometrie überführt und anschliessend deren Ähnlichkeit bestimmt. Anhand ihrer Ähnlichkeit werden die Messungen einander zugeordnet bzw. verworfen. Die zugeordneten Messungen werden als Elemente des lokalen Beobachtungsvektors aufgefasst, aus dem in einem letzten Schritt die gesuchte Grösse, interferometrische Phase oder Geländehöhe, mit Hilfe einer Ausgleichung der Beobachtungen geschätzt wird. Je nach Anwendung bedient man sich hierzu der Methode der kleinsten Quadrate zur Prädiktion, Interpolation oder Filterung der Daten.

Durch die repeat pass Konstellation der ERS Satelliten kann es zwischen den Überflügen zu Änderungen in den atmosphärischen Bedingungen kommen. Diese bedingen einen Laufzeitunterschied der Mikrowellen und überlagern sich dem topographischen Anteil der Phase. Mit einem bestehenden DGM kann der Einfluss der atmosphärischen Änderungen auf die interferometrischen Messungen abgeschätzt und beseitigt werden. Man unterscheidet zwischen lokalen und systematischen atmosphärischen Effekten. Lokale Störungen werden aufgrund ihrer Varianz im Interferogramm detektiert und vom weiteren Messvorgang ausgeschlossen. Systematische Einflüsse erzeugen ausgedehnte zusätzliche Interferenzlinien, die sich dem Phasenanteil aus der Geländehöhe überlagern. Mit Hilfe des DGMs lässt sich diese niederfrequente Überlagerung detektieren und durch ein Polynom niederen Grades approximieren. Ähnlich lässt sich auch der Effekt eines fehlerhaft bestimmten Basisvektors beseitigen. Die hierfür benötigte Genauigkeit des DGMs ist abhängig von der interferometrischen Basislänge und wird für Messungen, die mit kürzerer Basislänge durchgeführt wurden, von SPOT leicht erreicht. Gleiches gilt für den Einsatz eines DGMs zur Beschränkung der Lösung der 2π Mehrdeutigkeit der interferometrischen Phase, der sogenannten Phasenabwicklung. Durch die Beschränkung lassen sich die Folgen der Rauschanfälligkeit der bestehenden Algorithmen vermeiden und eine kontinuierliche Lösung für die Phase für das gesamte Interferogramm bestimmen. Neben der reinen Beschränkung der Phasenabwicklung lässt sich mit Hilfe einer Interferogrammsimulation auch der Phasenverlauf selbst in verrauschten Regionen schätzen. Hierzu wird die Phase durch einen Wiener Filter geschätzt. Die Filterparameter werden mit der Simulation bestimmt. Der Schätzer wird durch die Phasenkohärenz gesteuert, adaptiert sich also an die Rauschgegebenheiten der interferometrischen Messungen. Auch bestehende DGMs geringerer Auflösung können hierzu verwendet werden, wenn mit einer Bildpyramide gearbeitet wird.

Die Daten können ebenfalls auf der DGM Produktebene mit der genannten Methode fusioniert werden. Die Optionen zur Fusion sowohl von DGMs in gleicher Rasterweite, als auch eines groben DGMs mit dem höher auflösenden InSAR DGM werden hierzu im Orts- und Frequenzraum untersucht. Liegen beide DGMs im gleichen Rasterabstand vor, eignet sich eine lokale Polynomapproximation der Oberfläche zur Kombination der Beobachtungen. Interpolation und Filterung mit der Methode der kleinsten Quadrate eignet sich besonders für den Fall, dass ein existierendes weitmaschiges DGM mit den InSAR Daten fusioniert werden soll. Hierbei wird mit dem groben DGM der Höhentrend entfernt, die Beobachtungen mit der Methode der kleinsten Quadrate anschliessend gefiltert und schliesslich die lokale Oberfläche interpoliert. Die Synergie der Daten hinsichtlich ihrer Fehlereigenschaften lässt sich auch im Frequenzraum nutzen. Während bei

InSAR DGMs eher die niederen Frequenzen durch Fehler belastet werden, weisen stereo-optische DGMs das umgekehrte Verhalten auf. Die DGMs lassen sich somit durch einen Austausch der jeweils fehlerbelasteten Frequenzbänder fusionieren, indem man ihre Fehlereigenschaften ausnutzt. Die Methode eignet sich auch zur Fusion von bestehenden DGMs grösserer Rasterweite mit neuen InSAR Daten.

Alle Verfahren wurden zur Fusion von ERS und SPOT Daten in drei Testgebieten in der Schweiz und Spanien angewendet und evaluiert. Die Gebiete wiesen eine voralpine bis alpine Topographie auf, wodurch Probleme speziell für die InSAR Höhenmessung entstanden. Durch Datenfusion mit den SPOT Daten wurde in allen Fällen eine vollständige Phasenabwicklung ermöglicht und so jeweils ein vollständiges InSAR DGM generiert, das mit dem SPOT DGM fusioniert werden konnte. Beim Vergleich mit den nationalen Referenzdaten lag die fusionierte DGM Genauigkeit mit 5 - 6m in allen Fällen deutlich über den Ausgangswerten, wobei in diesem Wert der Einfluss der Vegetation noch nicht berücksichtigt ist. Die Ergebnisse, jeweils erreicht durch die Fusion eines InSAR DGMs mit einem stereo-optischen DGM, belegen die Synergie der Daten und das Potential, das in deren Fusion liegt.

ABSTRACT

Both spaceborne photogrammetry and SAR interferometry (InSAR) offer the opportunity for digital terrain model (DTM) generation. The photogrammetric method, during the last two decades preferably carried out with the French SPOT satellite series, generally achieves a DTM accuracy of around 10m. As SPOT acquires the images in two different passes (repeat pass), matching problems due to changes between the passes result in unacceptable large measurement gaps in the DTM. Cloud coverage compromises photogrammetric DTM generation in many parts of the world. On the other hand, InSAR height measurement is feasible independently from sunlight and cloud coverage. Data from the European remote sensing satellites ERS-1 and ERS-2 present an alternative to photogrammetric DTM generation in respect to data availability, measurement density and accuracy and processing automatization (and hence price). As InSAR is based on the range distance measurement, it faces some shortcomings from the image acquisition geometry, the required precision of the sensor location tracking and the repeat pass constellation of the ERS satellites. For those reasons, current spaceborne InSAR DTMs hardly match the accuracy of photogrammetric systems.

The presented work deals with the fusion of optical and SAR data for DTM generation. It will be examined, how and to what extent existing SPOT DTMs can be fused with InSAR measurements. Two options and accordingly two geometries present themselves for that problem: either the fusion during the InSAR processing, or the fusion on the DTM product level. In order to fuse the data, they are first converted to a common geometry and afterwards associated or rejected according to their similarity. The associated measurements are elements of the local observation vector, with which the concerning entity, phase or height, is estimated in a final step. Depending on the application, the least squares method is used for that purpose in order to predict, interpolate or filter the data.

The influence of atmospheric artifacts on the interferometric measurements can be estimated and removed with the existing DTM. One distinguishes between local and systematic atmospheric effects. Local disturbances of the phase are detectable by their variance and are rejected from the further processing. Atmospheric changes may also cause a systematic influence by adding large fringes superimposing the topographic fringes. This low frequency superposition is detected and removed with a low polynomial approximation derived with the

existing DTM. The required DTM accuracy depends on the interferometric baseline and is easily achievable for short baseline measurements. The same is valid for employing the DTM in order to constrain the solution of the phase 2π ambiguity, the so-called phase unwrapping. With the unwrapping constraint, the performance limitation of existing phase unwrapping algorithms in presence of noise is avoided and a continuous solution for the whole interferogram is determined. Besides using the DTM as unwrapping constraint, the phase slope can be estimated in noise corrupted areas. The phase in those areas is estimated with a Wiener estimator, which is steered by the phase coherence, thus adapting to the interferometric noise conditions. Also DTMs of lower resolution are applicable, if a multigrid processing is performed.

The presented method also applies to data fusion on the DTM level. The fusion options both of DTMs of the same resolution and coarse with a high resolution DTMs are examined in the spatial and the frequency domain. If both DTMs are of similar resolution, a polynomial surface approximation is convenient for the combination of the observations. Least squares interpolation and filtering is suitable for the fusion of an existing coarse DTM with the InSAR measurements. For that purpose, the height trend is removed with the existing DTM from the InSAR measurements, which are afterwards filtered and used for the surface interpolation. The data synergy in respect to their error properties is also exploited in the frequency domain. While the lower frequencies of InSAR DTMs are generally more error corrupted, the stereo-optical DTMs behave inversely in the frequency domain. Hence, the DTMs are fused by an exchange of the corrupted frequency bands, by taking advantage of their error properties. Also low resolution and high resolution data sets can be fused in this way.

The methods have been tested for the fusion of SPOT and ERS data sets of three sites in Spain and Switzerland. The sites showed prealpine and alpine topography, causing problems especially for InSAR height measurement. Data fusion with the SPOT DTM enabled a complete unwrapping solution in all cases, allowing to fuse the InSAR height measurements with the SPOT counterparts. The achieved DTM accuracy of 5 - 6m after the fusion was in all cases significantly below the original values of the stand-alone data sets. The influence of the vegetation is not considered in these values. The results prove the synergy between the data and fusion potential of InSAR and stereo-optical DTMs.

C h a p t e r   1

INTRODUCTION AND OBJECTIVES

1.1 Introduction

A digital terrain model (DTM) consists of an ordered array of numbers, representing the point (N, E, H) coordinates, stored on a digital storing device. With the finite amount of points, the real, continuous 3D topographic surface is approximated. The generic term DTM dates back to the fifties when it was first employed for road planning. Since these early days of computerization, not only storage, but also data acquisition and subsequent processing has become more and more digital, which especially holds for satellite remote sensing data for obvious reasons.

Evolving from earlier weather forecast missions, civil spaceborne optical imagery for geographical purpose became available with the start of NASA's Landsat 1 mission in 1972. The images were of photographic quality and supplemented high resolution airborne data by covering a large region with a single take. Advancements in digital image sensor technology during the eighties led to the construction of electro-optical scanners such as MOMS-01 (operated on Space Shuttle 1983) and the French SPOT (Système Pour l' Observation de la Terre) satellite series (four satellites since 1986). Both sensors are linear array line sensors. For almost two decades now, the SPOT programme offers stereoscopic measurement capabilities, thus the opportunity to derive thematic and geometric information from this imagery. The CNES (Centre Nationale pour des Etudes Spatiales), operator of the SPOT series, is doing a regular business with SPOT DTMs around the world. The need for two cloud-free image acquisitions within a short repeat pass interval limits the use of across track stereo-optical measurements in many parts of the world and drew the attention to active Radar imaging, which is not affected by this limitation.

In parallel to the achievements in the field of optical remote sensing, Radar (SAR) remote sensing evolved from being experimental, with time limited missions (e.g. SEASAT, SIR), to a regular remote sensing information source. ESA's ERS-1, starting in 1991, became the first permanently operated civil satellite carrying a SAR sensor and made these data broadly available. The ERS-1 provided not only backscatter amplitude imagery, but also the phase information, which can be exploited for SAR interferometry, being applicable for DTM generation. The ERS-1 and ERS-2 tandem mission, operated in an one day interval, provided regular interferometric coverage from 1995 until the end of the ERS-1 mission in March 2000. Meanwhile, the shuttle Radar topography mission captured most part of the world landmass interferometrically and proved the unique capability of this method of measuring large areas. The resulting 3" worldwide DTM is expected to be delivered starting in 2002.

A widespread application for DTMs is the geocoding of imagery, i.e. the conversion from the distorted image geometry to the rectangular map coordinate system. A typical example in the spaceborne case is the necessity to correct the thematic information, retrieved e.g. from the Landsat TM series, geometrically and radiometrically with a DTM, before it may enhance the national databases. Other examples for spaceborne DTMs applications are found in the fields of hydrology, geology and seismology, where interferometry plays a valid role for measuring seismic displacements after earthquakes. For terrain visualization purposes, DTMs allow to model a virtual world by contributing the third dimension.

The following work aims at the fusion of spaceborne stereo-optical DTM information with InSAR measurements in order to generate DTMs superior to the individual sources. In order to have information of similar scale and accounting the current data situation (e.g. availability, price), this fusion approach is reasonably performed with SPOT and ERS data, although the proposed methods are capable to treat comparable data.

1.2 Motivation

Although both stereoscopy with optical imagery and SAR interferometry have existed in parallel for roughly a decade, delivering DTM data of comparable accuracy and grid, only little research has actually been done in the field of fusing this information. However, the opportunity for redundant use of these measurements is evident in many ways. SAR interferometry is capable to deliver a large amount of measurements, as it measures pixel-wise the range distance between point and sensor, while the grid is interpolated from the matched points in the stereo case. On the other hand, the required texture for matching often hinders interferometry, which works better over bare soil. One

may add that the SAR sensor is not able to resolve terrain, steeper than the viewing angle. Although stereo-optical height measurement is also problematic in steep terrain, the problems are less pronounced there. As it has already been stated, SAR interferometry is not affected by cloud occlusion, which is limiting optical DTM generation in many parts of the world.

While stereo-optical and SAR interferometric DTMs behave complementarily in respect to failure, the individual measurements offer the opportunity for redundant exploitation, as their quality is comparable. From a SPOT stereo-image pair, one can reasonably derive a DTM product with 25m post spacing. The vertical root mean square (rms) error is generally expected to be approximately 10m, depending on the type of terrain. ERS InSAR DTM product specifications are similar, with comparable grid size and rms, but strongly depending on the terrain shape, landcover and the repeat pass interval duration. In both cases, large portions of the site may remain inaccessible, due to the mentioned processing and sensor limitations. Many applications require DTMs of higher quality than these benchmarks. It will be examined, how this differently derived information is favorably combined in order to obtain a product of significant higher quality than the stand alone DTMs.

In this context, it has hardly been investigated, if and how an existing stereo DTM can be updated with InSAR height measurements. This approach makes sense especially in respect to the abundance of relatively recent data available since the ERS-1/2 tandem mission. Measurements, originating from a different sensor and technique provide the opportunity to further improve the existing data by adding independently measured information. The cost-benefit ratio for combining independent information is possibly higher than that for exploiting single sensor redundancy.

Finally, the need for evolving SAR interferometry to an operational stand-alone technique for DTM generation during the past years implied that it had to go without an existing DTM, which was in fact hardly available during the last ten years. Comparable measurements of that grid size originate mainly from national databases and were therefore used as reference for testing and calibration of the InSAR technique. This thinking of existing measurements as a reference is displayed in the current fusion approaches of ERS and SPOT measurements. SPOT DTMs are commonly applied for fringe flattening or even as reference measurements, without scrutinizing them. Hence, the introduction of a priori knowledge into the InSAR DTM generation process is hardly developed, although the whole process, which is very sensible in respect to systematic errors (e.g. atmospheric effects, phase unwrapping), certainly profits from any existing information.

1.3 Objective

The central objective of the work is the quality improvement of existing SPOT DTMs by means of fusing them with ERS InSAR data. Quality in this context means primarily accuracy and secondarily amount and distribution of the measurements. It will be examined, how these measurements can favorably be fused in order to not only overcome the individual limitations but also retrieve a best height estimate from combining both sources. The mathematical models, according to which these data are fused, are derived from the adjustment theory.

The addressed problem of fusing existing with recent positional measurements from different sensors has two formulations, depending on the level of processing. The existing measurements can be introduced during the InSAR DTM generation process as a priori information or can be fused with the InSAR DTM on product level. The solution approaches for both problems, comprising the setup of the fusion model and optimization criteria, differ and will be determined for each level separately.

For the fusion instance of integrating the SPOT data in the InSAR measurement process, the InSAR DTM processing steps are reviewed for optional introduction of existing measurements. If a priori knowledge is available, the most critical InSAR problems are at least mitigated. This applies especially for phase unwrapping, the reduction of the effects of atmospheric artifacts and the precise determination of the baseline. As the existing SPOT measurements can not be assumed to be of higher accuracy than their interferometric counterparts, an error leakage into the InSAR measurement process has to be avoided. The methods to be developed will take this into account by employing the existing SPOT information as processing constraint or for filtering purposes.

Besides the measurement process fusion option, the information can be fused on the DTM product level. The introduction of redundancy reduces not only the amount of outliers but also is expected to improve the general error statistic of the fused result. The different error properties need to be taken into account. The task is then to apply the methods of adjustment theory to solve the given problem. The favorable approach will be identified, which takes best advantage of the different properties of the data sources.

Both, fusion during InSAR DTM generation and on product level are reviewed for the quality requirement of the existing data set. Although it is convenient to use a SPOT data set for the fusion with ERS InSAR, other DTM sources, possibly of lower resolution and accuracy, are applicable.

The work comprises data, methods and techniques from both, photogrammetry and SAR interferometry. The result shall provide an interface between the techniques by fusing their data. Although facing comparable problems, the exchange between both research communities is hitherto limited. Hence, it is certainly an objective of the work to invoke and promote not only data, but also exchange knowledge between the research communities.

1.4 Overview

The work consists of 7 chapters. Chapter 2 delivers an introduction to state-of-the-art DTM generation. It focuses mainly on the InSAR DTM generation process, which is completely reviewed. The processing flow is presented, with each step being elaborated to some detail. The limitations of the technique and the error sources are stated. Besides, an introduction to spaceborne stereo DTM generation with optical imagery is given and subsequently confronted with InSAR in order to determine the individual strengths and shortcomings. The state of the art fusion techniques in the field of DTM fusion of optical and SAR sensors are reviewed at the end of that chapter.

A concept that is capable to tackle the problem of DTM fusion is proposed in chapter 3. The fusion of that type of geometric data is a problem, which requires special treatment of the multidimensionality of the data. DTM fusion is a special form of the common engineering problem of fusing positional redundant data from different sensors. Common fusion approaches, originating mostly from military applications, deal with multidimensionality as a side effect, as these approaches are mostly object based. In the examined case, the fusion problematic is divided in three sub-problems, which are solved individually. Firstly, a common geometry has to be established. The discussed case has two main geometries - slant range and map geometry. Fusion can be carried out in both. Secondly, the data need to be grouped in similar measurements, for which data fusion is reasonable. Hence, an association and assignment metric has to be established. Thirdly, estimation is carried out with the grouped data. This aims at finding an estimate of the searched entity, which best fits to the observations from the individual sensors. The functional model differs in both geometries, as the fusion objective varies in both scenarios.

The realization of the data fusion process in slant range geometry is given in chapter 4. With the given observations from an independent sensor, the most critical steps in SAR interferometry are solvable. The phase unwrapping, which prevents repeat pass interferometry from working

operationally in many cases, profits an approximation of the phase slope is available. This estimate is derived by applying an optimal filter to the interferometric observations and using locally the simulation from the optical DTM in order to retrieve the filter parameters. The extent of the atmospheric contribution to the measured phase can also estimated when fusing the interferometric with the optical measurements. Otherwise, possible atmospheric artifacts within an interferogram, also arising from the repeat pass constellation of existing spaceborne SAR interferometers, are not at all detectable without redundancy and corrupt the whole measurement process. SAR interferometry, being a range distance measurement technique, needs precise determination of the orbit position during image acquisition. As the baseline precision hardly matches the requirements, a systematic error is imminent. The baseline dependency is mitigated, when existing DTM information is available.

Besides the fusion in the slant range domain, often dubbed as DTM integration, also the combination of the DTMs in map geometry is discussed. Chapter 5 addresses this problem with two approaches, based on DTM interpolation techniques. The starting point of both approaches is the redundant surface coverage. In order to find a best fitting surface, one adjusts the different observations by a polynomial approximation of the local surface based on the ensemble of locally available measurements. The second approach splits the trend from the actual surface in order to minimize systematic and local errors separately. By a fusion realization in the spatial frequency domain, it is shown that the InSAR error is mainly concentrated at the low DTM frequencies. This low frequent error can be substituted by the corresponding stereo DTM frequencies, resulting in a drastic error decrease.

In chapter 6, the concept and its realization are tested at different test sites, representing demanding types of terrain. Rolling and mountainous terrain in Switzerland and Spain has been initially surveyed with SPOT and, more recently, with ERS. The individual results lied within the expectation, but were in part of very limited use. In order to achieve a result of improved quality, the ERS measurements were fused with their existing SPOT counterparts. The result of the data fusion is significantly improved in respect to its sources when compared to the national databases in the same scale. The rms error of the resulting DTMs varied between 4 and 6m, depending on the terrain, and proved the fusion potential of the data.

Chapter 7 summarizes the previous chapters. The results are evaluated and lead to the conclusion of the presented work. Finally, an outlook to further activities in this field is given, taking into the account some forthcoming SAR and optical satellite missions.

C h a p t e r   2

INSAR AND STEREO-OPTICAL DTM GENERATION

2.1 Introduction

This chapter gives an introduction to DTM generation with spaceborne SAR interferometry and stereoscopy with optical sensors. As it is reasonable for the addressed problem of fusing an existent stereo DTM with InSAR data, interferometry will be described to some detail in section 2.2. After describing each processing step, the error sources and their impact on the DTM accuracy are outlined. Section 2.3 gives an overview on stereo-optical DTM generation and states some of its main processing steps. In section 2.4, the generation techniques are compared to each other and their advantage and disadvantages are evaluated in respect to the desired data fusion. Finally, the state-of-the-art fusion techniques for InSAR and stereo-optical DTMs are summarized in section 2.5.

2.2 InSAR DTM Generation

2.2.1   Overview

The first civil use of SAR interferometry for topographic mapping has been demonstrated by *Graham (1974)*, who reported the results of an airborne dual antenna SAR interferometer. The further advancements in SAR and digital processing helped to develop this technique as described in *Zebker and Goldstein (1986)*. The results could successfully be transferred to the spaceborne case, being particular due to the repeat pass constellation *(Goldstein et al., 1988)*. The technique evolved enormously during the last decade with the increasing SAR data supply provided by the satellite

missions operated by ESA (ERS-1/2), NASDA (JERS-1) and CSA (RADARSAT-1) and found a preliminary peak in the shuttle radar topography mission (SRTM) in the year 2000.

A series of recent publications deal with the technique. *Madsen and Zebker (1999)* give an introduction to the general theory and applications, *Rosen et al. (2000)* give an in depth analysis of the technique, systems and limitations and show several applications. Technical reviews are also given e.g. by *Xia (1996)*, *Bamler and Hartl (1998)* and *Small (1998)*.

2.2.2   Acquisition Geometry and Data

The imaging geometry of an across track SAR interferometer is given in Fig. 2.1. The platform moves at uniform speed and altitude in along track or azimuth direction (a), while the antenna by turns transmits and receives microwave pulses (wavelength λ) at a looking angle θ. The pulses are transmitted to the side, in a plane perpendicular to the track (i.e. squint angle = 0°). The footprint on the ground is an oval with long axis in range direction. The target backscatter from increasing range is received and sampled at increasing time, forming a scanned line in range (r). Repetition of the procedure highlights a strip on the ground, which is postprocessed to a SAR image c(r, a).
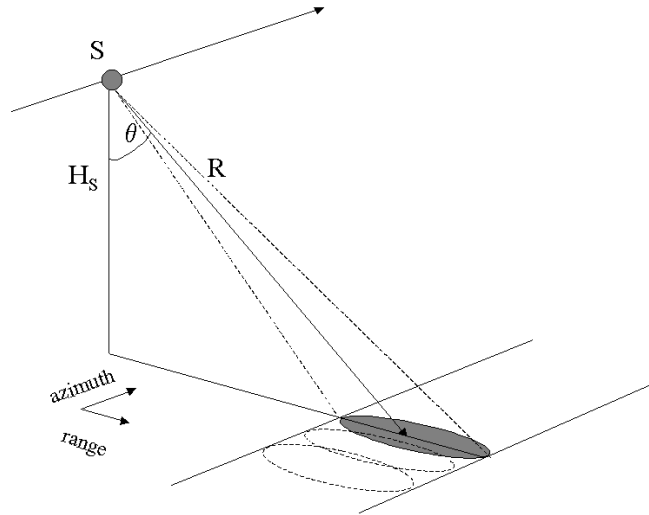
Fig. 2.1 SAR image acquisition geometry for a right looking system flying at altitude H_S. A sequence of spots are highlighted on the ground and formed to an image in range and azimuth coordinates.

The image is ordered horizontally according to the increasing range and vertically to the Doppler times. After pulse compression (pulse duration t) the range size r_r of a resolution element is

$$r_r = \frac{v_c t}{2} \qquad (2.\,1)$$

with v_c being the light velocity. The range pixel is the projection of the response of a ground resolution element into the SAR image plane. For ERS, the range pixel size is 7.9m, which equals a ground range (r_g) distance of ~20m ($r_r / \sin\theta$) (Fig. 2.8). The azimuth pixel size after azimuth compression for ERS is 4m. Therefore, an ERS image does not consist of 'square' pixels. The standard ERS full frame image consists of 5'000 pixels in range and 25'000 pixels in azimuth. Despite these pixel dimensions, the ERS SAR image resolution (i.e. least recognizable image detail) is lower than resolution of comparable optical imagery, due to the speckle effect (Fig. 4.7). However, SAR interferometry does not depend on recognizable image features, but on the evaluation of the phase of each resolution element. The ERS InSAR DTM post spacing (25 - 50m) is therefore comparable to that of a DTM, generated with SPOT stereo images (10m pixelsize panchromatic).

For SAR interferometry, two SAR images, taken from slightly different orbit positions are combined. SAR, being a coherent imaging system, provides, besides the backscatter amplitude, the phase information φ for each resolution element:

$$\varphi = \frac{2\pi}{\lambda} 2R + \varphi_o \qquad (2.\,2)$$

with R being the range distance between sensor and target and φ_o the phase contribution of the target properties (e.g. vegetation, humidity).

In order to eliminate φ_o for height measurement, a second image is acquired and the phase difference is calculated. Assuming that the target properties have not changed, the phase difference becomes (Fig. 2.5)

$$\varphi_2 - \varphi_1 = \phi_{abs} = \frac{4\pi}{\lambda}(R_2 - R_1) \qquad (2.\,3)$$

The phase difference for each point in the scene is calculated. As the phase difference is only measurable modulo 2π, a regular phase pattern, the interferogram, emerges as resulting image. The phase differences are related to the range distance difference between each antenna and the imaged point, which is a function of the topographic height. Given the range and azimuth relation of the

15

imaged point, the phase measurement yields the third equation required to determine the absolute orientation (section 2.2.9).

Spaceborne SAR imagery is distributed by the space agencies. The ESA image product suitable for interferometry is the so-called single look complex image (SLC), a two band image, which is the harmonic separation of the received backscatter signal in a real (cosine) and complex (sine) part *(Vass and Battrick, 1992)*.

Geometric Distortions Ranging and the looking geometry produces geometric distortions when imaging an elevated surface. The image geometry in respect to terrain is illustrated in Fig. 2.2. An iso-azimuth line in the image corresponds to the intersection of the surface with the plane into which the pulse is transmitted. When projecting the terrain into an image line, the echoes are received according to their travel times. Therefore, whenever the terrain slope angle facing the sensor $\alpha \neq 0$, the distance between two imaged points b and c is shorter than the distance between B and C on the ground. As long as $\alpha < \theta$, this effect is called foreshortening. When the slope is perpendicular to the beam, so $\alpha = \theta$, the distance between the points is compressed to a single range resolution element. Larger slopes lead to points, which are imaged in reverse order, their signal being overlaid with the signal of points situated on the same arc (D-E in Fig. 2.2). Consequently, this type of distortion is called layover. Finally, if terrain back slopes are steeper than $\alpha \leq \theta - 90°$ the terrain is not illuminated by the SAR - an effect which is denoted as shadowing (F-G).
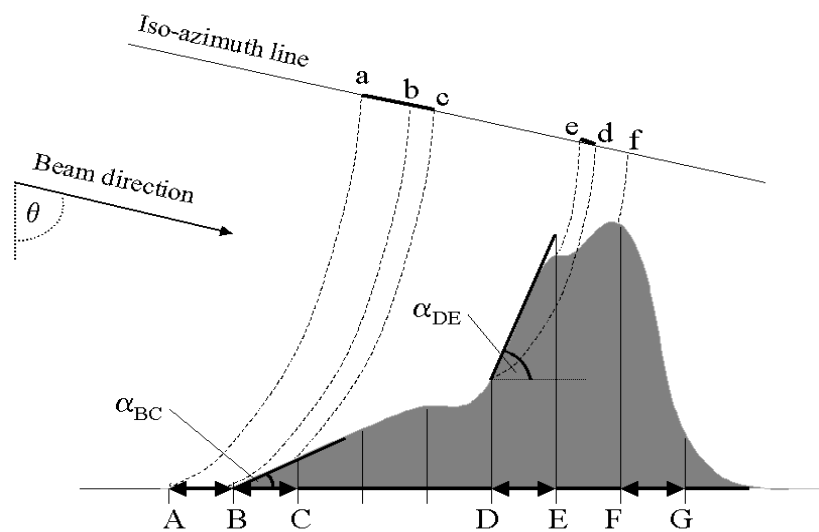
Fig. 2.2 Slant range vs. ground range geometry. The right looking SAR flight track is perpendicular to the page. Foreshortening, (BC), layover (DE) and shadowing (FG) are illustrated as mentioned in the text.

2.2.3   Orbit Determination

Orbit Samples of the orbit position of the satellite during the image acquisition are delivered to the user with the ERS SAR data in form of N=5 state vectors, representing the position and velocity of the platform commonly given in the ECR (earth centered rotating) coordinate system. Based on the short duration of the image acquisition (number of image lines times the pulse repetition frequency), the orbit is then approximated by a polynomial in each direction:

$$\underline{S} = \begin{pmatrix} X(t) \\ Y(t) \\ Z(t) \end{pmatrix} = \begin{pmatrix} \sum_{i=0}^{N-1} a_i t^i \\ \sum_{i=0}^{N-1} b_i t^i \\ \sum_{i=0}^{N-1} c_i t^i \end{pmatrix} \tag{2.4}$$

The state vectors are used to solve for the polynomial coefficients a_i, b_i and c_i with the least squares approach. As the state vectors are derived by propagating the velocity and position information from an initial point vector, the accuracy of calculated orbits is dependent on the quality of the information of that point and the vector propagator. A deviation of the approximated orbits from the real ones causes an erroneous sensor-target relation, thus producing a systematic error in the DTM. In response to the precision requirements for interferometry, ESA provided highly accurate state vectors available at D-PAF *(Massmann et al., 1993)* and the Delft Institute for Earth-Oriented Space Research (DEOS) *(Scharroo et al., 1998)*. The DEOS product accuracy is reported to be 5-6cm, while the D-PAF is slightly worse (8-10cm), but includes the satellite's velocity information.

Example A comparison between position vectors accompanying the image product and DEOS vectors are given in Tab. 2.1. Their absolute difference is plotted in Fig. 2.3. The initial point differs already by more than 6m, but still marks the closest approach between the orbits. Due to the weakness of the propagation method, the deviation increases with time. Assuming that the DEOS product is of much higher accuracy, the effect of erroneous positional information is illustrated in Fig. 2.4, where the resulting interferometric phase difference for the second Spanish test data set is shown. Two interferograms are calculated and flattened (see section 2.2.5) with help of the orbital models. After removal of the topographic fringes, by subtracting the interferograms and dividing the difference modulo 2π, a residual fringe remains. The residual fringe corresponds in this case to a height error of 60m and causes a systematic DTM error.

Propagated Position			DEOS Position		
X	Y	Z	X	Y	Z
5448132	-241204	4627878	5448132	-241198	4627881
5435558	-245460	4642378	5435556	-245454	4642383
5422942	-249709	4656843	5422938	-249704	4656851
5410285	-253951	4671275	5410279	-253947	4671285
5397587	-258187	4685671	5397579	-258183	4685684

Tab. 2.1 State vectors included with the SAR imagery (left) and the DEOS position. The time increment between the vectors is 2.6s. The absolute position difference increases with the time.

	1	2	3	4	5
absolute difference	6.71	8.07	10.25	12.33	15.78
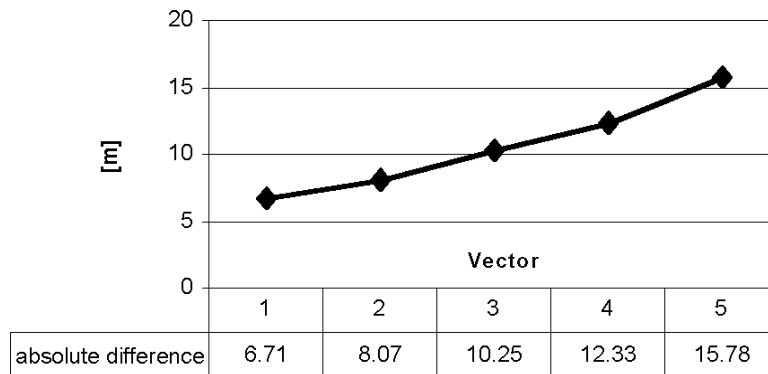
Fig. 2.3 Absolute difference between the 5 DEOS and propagated vectors. Starting from a relative small error at vector 1, the difference more than doubles with the time, due to the propagation inconsistency.

Fig. 2.4 Effect of inconsistent positional accuracy on interferogram phase (see also Fig. 2.6). The interferometric phase difference, computed by $\mathrm{mod}(\phi_{prop} - \phi_{DEOS}, 2\pi)$, results from the state vector difference. The full 2π cycle equals a height of 60m and would lead to a DTM tilt.

If precise vectors are not available, ground control points are required to optimize the orbit model, which is inevitable for the baseline calculation.

Baseline For the baseline determination, i.e. the calculation of the orbit separation, the master and slave orbits must be related to each other.

The straightforward solution for this problem is to calculate the point of closest approach between the orbits. This is performed by iterating along the orbits $\underline{S}_1$ and $\underline{S}_2$ (2. 4), calculating the baseline magnitude $B = |\underline{B}|$

$$|\underline{B}| = |\underline{S}_2 - \underline{S}_1| \tag{2. 5}$$

Iteration with decreasing time intervals in the neighborhood of the minimum of B yields the point of closest approach and correspondingly the baseline vector $\underline{B}$ at this point.

$$\underline{B} = \underline{S}_2 - \underline{S}_1 \tag{2. 6}$$

This approach delivers sufficient accuracy for the coming image registration. However, for phase to height conversion, the baseline vector must be refined and its time dependency must be considered (sections 2.2.8 and 4.2).

2.2.4   Image Registration

Coarse The image offsets in range and azimuth are calculated in a first registration step. In the ERS case, this can be performed by using the orbit models, calculated in the previous section.

The range offset is calculated in respect to a given reference point $\underline{P}_{ref}$, generally the center point of the master scene. The corresponding master and slave satellite positions $\underline{S}_{1Pref}$ and $\underline{S}_{2Pref}$ are derived from the orbit models and baseline calculation. The distances $|R_i|$ between reference point and both satellite positions are given by

$$|R_i| = |\underline{S}_{i\,Pref} - \underline{P}_{ref}| \tag{2. 7}$$

The range offset c_{range} in pixels is calculated with the known slant range pixel spacing r_r

$$c_{range} = \frac{|R_1| - |R_2|}{r_r} \tag{2. 8}$$

The azimuth offset $c_{azimuth}$ is calculated in respect to the acquisition time of the first master image line. The starting times of each scene, t_1 and t_2, are delivered with the SAR scenes. The established orbit model allows computing the time t_{21}, which corresponds to the position of the slave sensor in respect to the first master image line (e.g. by determining the closest approach between the sensors). The time for taking one line in azimuth direction is the inverse of the pulse repetition frequency (prf) (ERS: 1678Hz), hence the azimuth offset is estimated by

$$c_{azimuth} = prf\,(t_{21} - t_2) \qquad (2.\,9)$$

If the orbit information is not accurate enough, the offsets are calculated by maximizing the correlation coefficient between the master and the slave scene. A large enough patch is selected at the same position in both images. While moving the slave patch pixelwise in range and azimuth, the correlation coefficient is calculated and stored for each position. The maximum correlation coefficient belongs to the image offsets c_{range} and $c_{azimuth}$.

Fine After the offset determination, the images are registered accurately to few pixels. However, to obtain the spectral overlap of the ground responses belonging to the pixels of each scene, the images must be registered to subpixel accuracy. For that purpose, the optimal fringe visibility criterion must be matched *(Gabriel and Goldstein, 1988)*. Fringes are best visible when the images are best registered to each other. Mathematically, this is the case when the fringe signal to noise ratio (SNR) reaches its maximum.

Several chips (i.e. image patches) are selected, spread along and across the scene. Starting from the range and azimuth offsets, a solution of the maximal fringe visibility criterion is sought by iteratively moving the patches and calculating the SNR. The images are oversampled by factor two in each direction. The fine offsets are interpolated using further oversampling in the neighborhood of the maximum. The results from each chip are used for polynomial fitting of the slave image to the master image geometry, to which it is resampled in a final step.

As the fringe frequency increases with the baseline length, the image registration becomes more demanding. For example, if the baseline length is 100m, the fringe period is about 15 pixel, if the length is 600m, the period is 2 pixel. Image registration must be more precise than 1 pixel in the latter case *(Xia, 1996)*. Weak registration leads to a coherence decrease, thus to minor measurement accuracy (section 2.2.10).

2.2.5   Interferogram Calculation

The interferogram is formed by a multiplication of the master image $c_1(r,a)$ with the conjugate complex of the co-registered slave image $c_2^*(r,a)$. In order to reduce the phase noise, one undersamples the image by averaging N adjacent pixels, commonly denoted as taking N 'looks'.

$$\Phi(r,a) = \sum_{i=1}^{N} c_{1i}(r,a) \cdot c_{2i}^{*}(r,a)$$

(2. 10)

The interferometric phase ϕ, being the argument of $\Phi(r,a)$, is derived by

$$\phi(r,a) = a\tan\left(\frac{Im\{\Phi(r,a)\}}{Re\{\Phi(r,a)\}}\right)$$

(2. 11)

The multi look technique reduces the phase standard deviation by $N^{-\frac{1}{2}}$, sacrificing on the other hand spatial resolution *(Rodriguez and Martin, 1992)*. With regard to the pixel size in ground range (section 2.2.2), usually 5 looks in azimuth are taken in the ERS case in order to achieve almost 'square' pixels. If further noise reduction is required, one may apply local averaging or spectral filtering, with a band pass centered around the local peak frequency. The latter approach yields slightly better results as it adapts to coherence and phase slope conditions.

Due to the properties of the tangent function, the phase is only known in a 2π interval (Fig. 2.5, Fig. 2.6). This 2π ambiguity is solved during the so-called phase unwrapping process, which yields the continuous phase course. As the unwrapping result depends on the starting point of the procedure, a constant, being a multiple of 2π, has to be added to each unflattened, unwrapped phase value for absolute phase ϕ_{abs} derivation (Fig. 2.5). The absolute phase measures the range difference ΔR between the satellites (2. 3).

$$\Delta R = \frac{\lambda}{4\pi}\phi_{abs}$$

(2. 12)

$$\phi_{abs} = 4\pi/\lambda(R_2 - R_1)$$
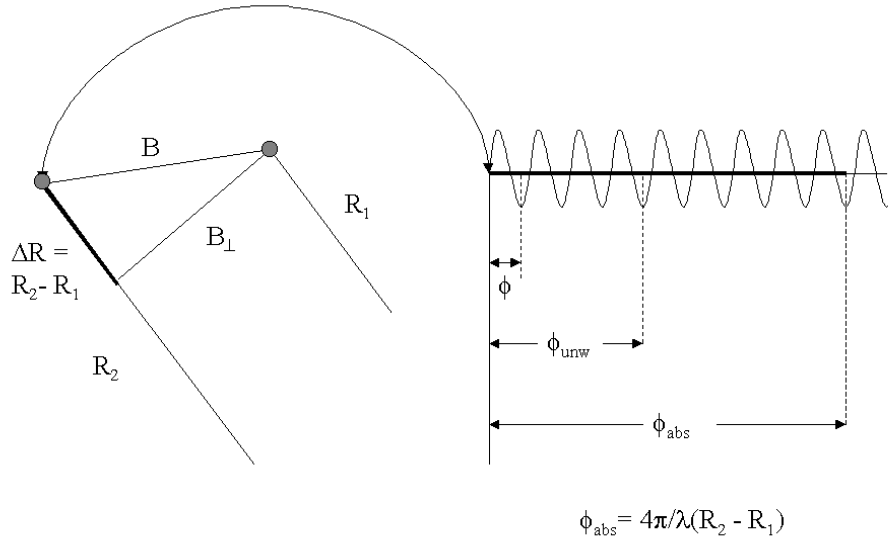
Fig. 2.5 Relation between range difference (left) and phase. The phase is originally measured modulo 2π. This ambiguity is resolved through phase unwrapping. The absolute phase value is directly proportional to the range difference.

Flattening In order to facilitate the unwrapping process to come, the amount of fringes is reduced either by subtracting from the interferogram the simulation from an existing DTM or by removing the systematic phase contribution due to the earth curvature - the so called interferogram 'flattening'. DTM flattening is discussed in chapter 4.

The commonly used flattening approach computes a synthetic interferogram originating from the ellipsoid with constant, e.g. zero, height. It models for each interferogram point the phase contribution from the earth ellipsoid. The range distances R_1, R_2 between a point on the surface of the ellipsoid P_{ell} and both satellite positions (2. 4) are computed with (2. 7). The related phase ϕ_{ell} is then computed with (2. 12) and removed from the interferogram.

Faster methods fit a polynomial through the range and azimuth coordinates of known ellipsoid phase values for the whole scene *(Geudtner and Schwäbisch, 1996)*. When subtracting the ellipsoid contribution to the local phase, the remaining fringe lines follow closely the local topography (Fig. 2.6).
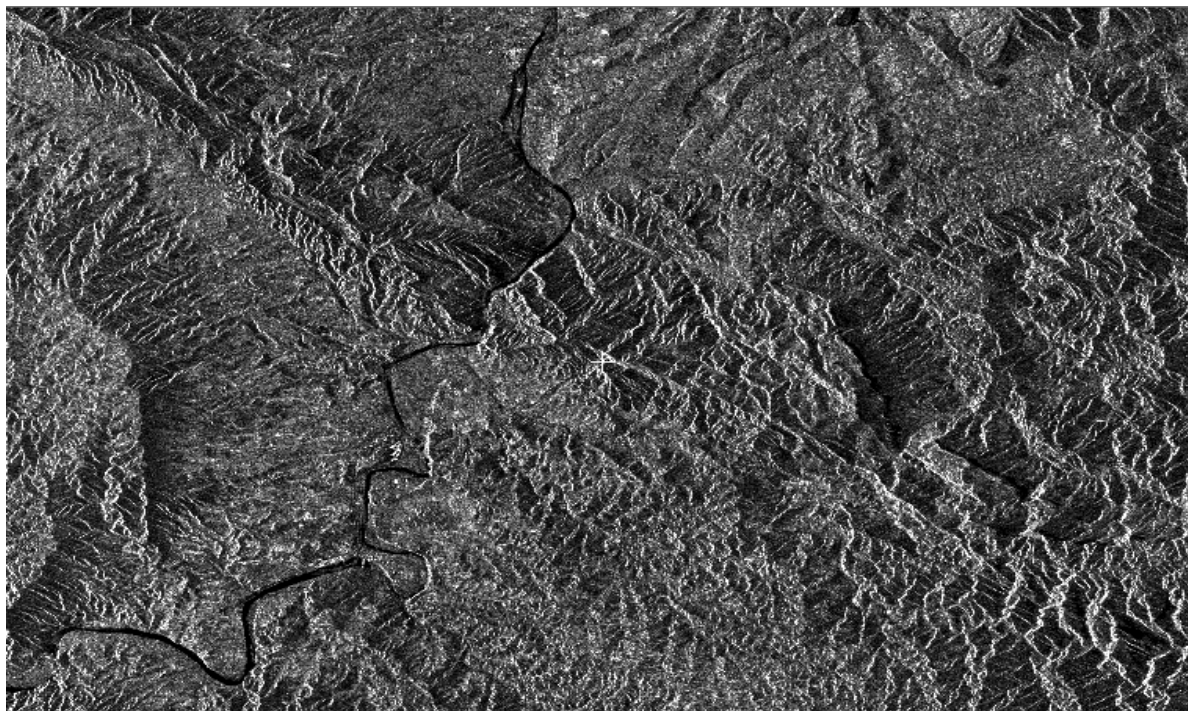
Fig 2.6a ERS SAR amplitude image of test site Spain II (see also sections B1, B2 (appendix)). Some features like the Ebro river or the mountains are recognizable by their backscatter properties. The mountains look distorted due to the SAR imaging geometry (e.g. lower right). For interferogram generation, two SAR images are necessary.
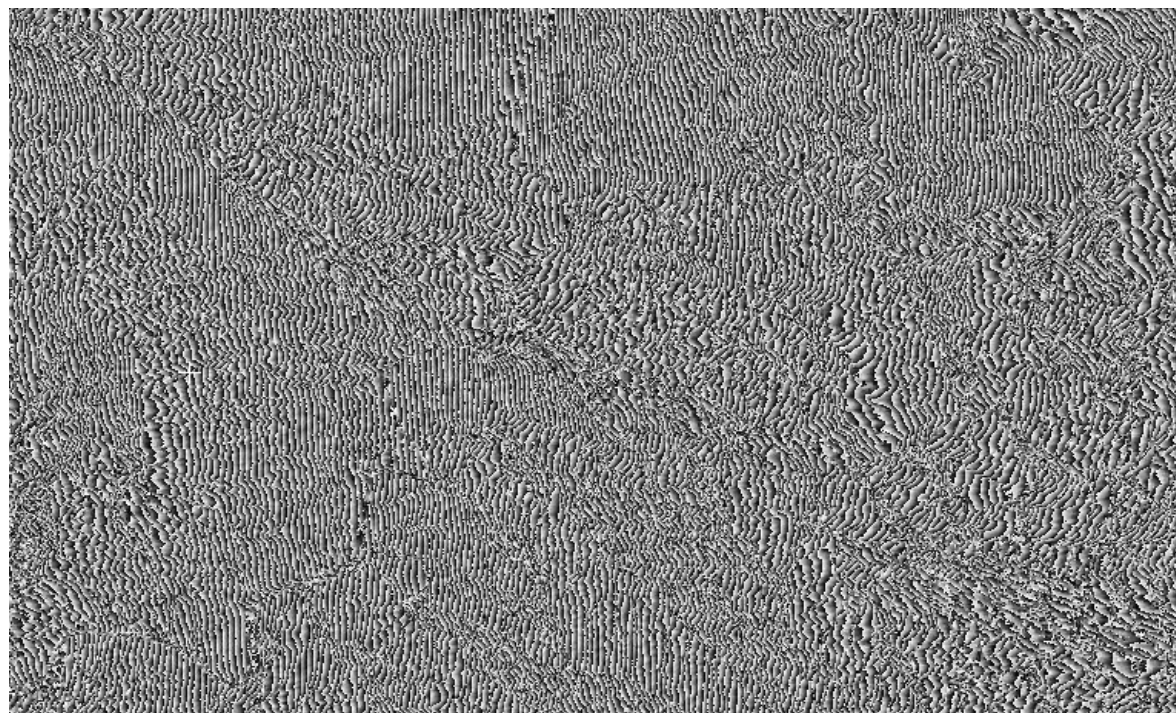
Fig 2.6b Interferogram of test site Spain II. The phases are only measurable in 2π intervals, therefore the characteristic phase pattern (fringe) arises. The dominant frequency is in range direction (left to right), but is distorted from the topographic phase contribution in the mountainous part of the site. This dominating phase trend is approximated by the local earth ellipsoid or an existing DTM and is removed in order to reduce the amount of fringes, thus facilitating especially the phase unwrapping.
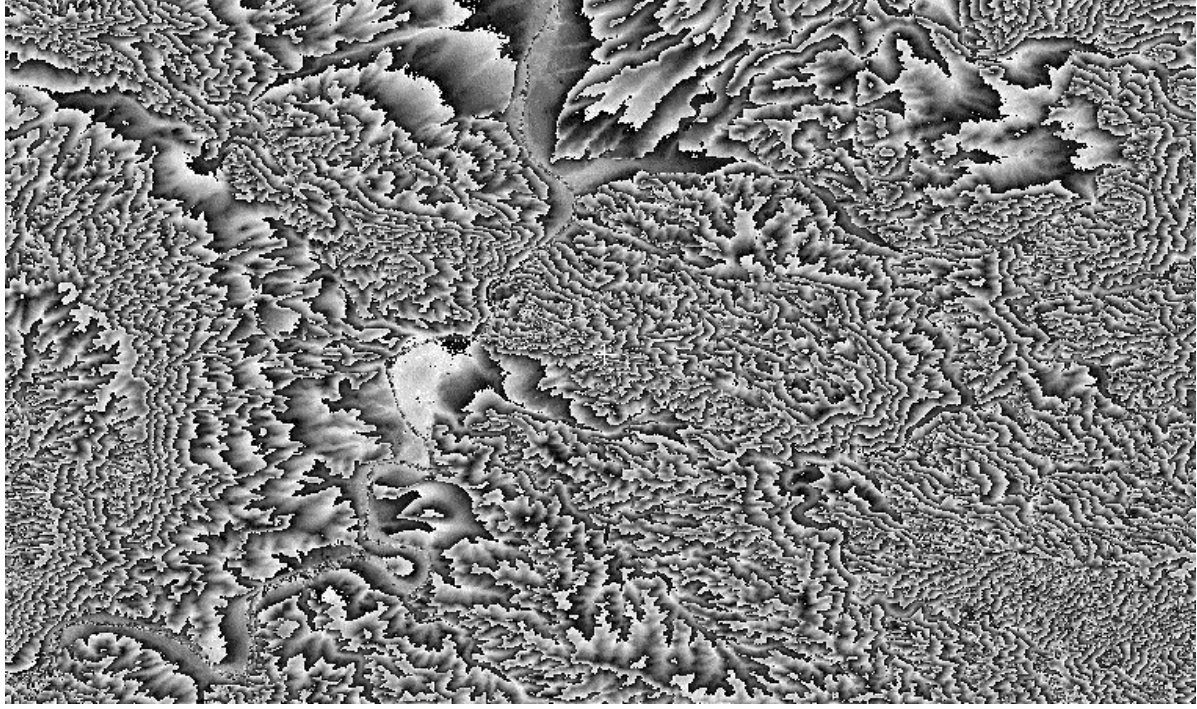
Fig 2.6c Ellipsoid flattened interferogram of the test site Spain II. After flattening, the fringe lines follow the topography and resemble contour lines. A qualitative height analysis can therefore already be performed at this stage of the processing with the known ambiguity height (2. 36). The flatter the terrain the broader the fringes and vice versa. High fringe frequencies foreshadow the unwrapping problems at the site (section 6.5).

2.2.6   Coherence Calculation

The magnitude of the correlation coefficient of the two images c_1 and c_2 is denoted as coherence γ. It is calculated with from the flattened N look interferogram within an estimator window of size M

$$\gamma = \frac{\left| \sum_{i=1}^{M} c_{1i} c_{2i}^{*} e^{-j\phi_{ell}} \right|}{\sqrt{\sum_{i=1}^{M} |c_{1i}|^2} \sqrt{\sum_{i=1}^{M} |c_{2i}|^2}}$$

(2. 13)

The sum within the estimator window describes the local mean, therefore the sums are often replaced by the expectation operator. As can be seen from (2. 13), the coherence value varies with the estimator window size. The total number of looks taken for the calculation of γ is $M \times N$.

Coherence is a measure for the similarity between the interferometric image pair and is defined between 0 (non overlapping image spectra) and 1. The coherence value indicates from which interferogram areas height information is reasonably derived and, especially in repeat pass constellations, where surface changes spoil the initial assumption of the same ground reflectivity spectrum for both passes. The InSAR sensitivity to surface changes is exploited for various SAR

24

applications as land use mapping *(Wegmüller and Werner, 1995)* and natural disaster monitoring *(Wiesmann et al., 2001)*.

Decorrelation The decorrelation consists of three major contributions

$$\gamma = \gamma_{temp} \gamma_{spatial} \gamma_{noise}$$
(2. 14)

where γ_{temp} means temporal decorrelation, $\gamma_{spatial}$ means spatial decorrelation and γ_{noise} is the decorrelation due to thermal noise.

The temporal decorrelation is a major limitation to repeat pass interferometers like the ERS single mission, having a 35-day repeat pass interval. By definition, temporal decorrelation is the ratio between the stable scattering to the total scattering intensity of a resolution element. Temporal decorrelation refers to the physical changes in position of scatterers within a resolution element. It has been shown that correlation decreases exponentially with increasing displacements, with greater sensitivity towards position changes in vertical direction *(Zebker and Villasenor, 1992)*.

Spatial decorrelation includes both the contributions from baseline and volumetric effects. Both sources can be interpreted geometrically regarding the viewing angle difference $\Delta\theta$. As shown in Fig 2.7, the viewing angles θ_1 and θ_2 are slightly different due to the baseline separation of the antennas.

The wavelength λ transmitted from the antenna in slant range is projected to a ground range resolution cell. The scale factor for that projection is $1/\sin\theta$ assuming a flat earth for the moment. Expressed with wavenumbers ($k=2\pi/\lambda$), the wavenumber in ground range k_{gr} becomes

$$k_{gr} = \frac{4\pi}{\lambda}\sin\theta = \frac{4\pi f_o}{c}\sin\theta$$
(2. 15)

with f_0 being the central frequency of the SAR. The factor 2 originates from the two ways travel path.

With differing viewing angles, the wavenumber for each acquisition changes (Fig. 2.7). Neglecting the stretch and linearizing:

$$\Delta k_{gr} = \frac{4\pi}{\lambda} \Delta\theta \cos\theta \tag{2.16}$$

The wavenumber shift given in (2.16) causes the spectral components of the range spectrum of the same resolution cell to be shifted by Δf *(Gatelli et al., 1994)*:

$$\Delta f = -\frac{f_o \Delta\theta}{\tan\theta} \cong -\frac{f_o B_\perp}{R\tan\theta} \tag{2.17}$$

with $B_\perp = B\cos(\theta-\alpha)$, the orthogonal baseline component (Fig. 2.5, Fig. 2.10). In other words, the SAR system acquires slightly shifted ground reflectivity spectra with each pass. Only the overlapping part of the spectra is usable for interferometry.
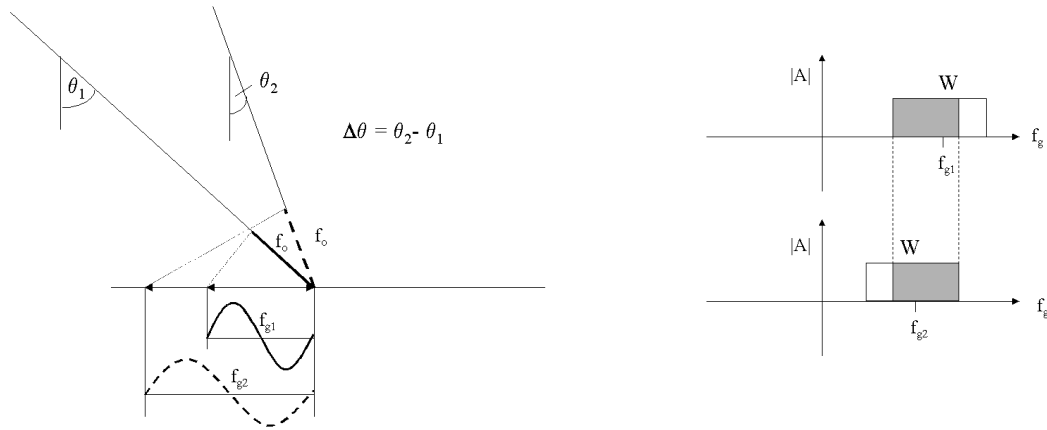
Fig. 2.7 Shifted ground reflectivity spectra $A(f_g)$ of the same ground resolution element due to slightly different viewing angles (exaggerated). From the bandwidth W, only the overlapping part of the spectra (grey) is usable for interferometry

As can be seen in (2.17), the frequency shift is directly proportional to the baseline length. Thus, at the critical baseline $B_{\perp c}$, where Δf equals the system bandwidth W, the spectra become disjoint - the responses are completely decorrelated ($\gamma=0$).

$$B_{\perp c} = \frac{WR\tan\theta}{f_o} \tag{2.18}$$

The critical baseline length is an important interferometer design parameter. For ERS, $B_{\perp c} \approx 1100m$ with nominal system values. The fact that the shift increases with the baseline length, thus the correlation declines, is often denoted as baseline decorrelation.

26

Apart from the baseline length, the terrain slope α increases the spectral shift, as (2. 17) becomes

$$\Delta f = \frac{f_o \Delta \theta}{\tan(\theta - \alpha)}$$

(2. 19)

Hence, the critical baseline length is significantly reduced in presence of slopes.

Spectral shift filtering with filters tuned to the center frequencies has been proposed in to order to decrease the spatial decorrelation *(Gatelli et al., 1994)* and is realized with bandpass filtering.

The previous considerations have been made under the assumption of a bare soil surface. If, on the other hand, the received signal originates from elevated scatterers within the resolution cell, the volumetric scattering contribution has to be taken into account. Geometrically, volume scattering increases the size of a ground range resolution element, as the scattering originates from all targets within a resolution element exposed to the SAR beam (Fig. 2.8). With the previous discussion of the wavenumber shift, one verifies that this increase of size results in a decreased coherence *(Rodriguez and Martin, 1992)*.
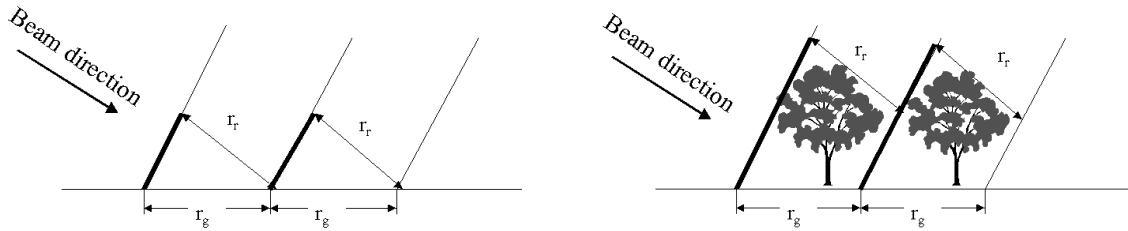
Fig. 2.8 Volume scattering. The slant range and ground range pixel dimensions are given for flat earth and elevated scatterers with in the resolution cell. The different sizes of the projection of the ground range cell perpendicular to the look direction are boldly indicated. As the volume within the resolution cell contributes to the scattering, the correlation decreases with increasing scatterer heights (from: *Rosen et al., 2000*).

Prati et al. (1994) show that the relationship between volumetric contribution, originating from the targets of height Δz within a resolution cell, and the baseline has to be

$$\Delta z << \left| \frac{\lambda H_S \tan(\theta - \alpha)}{2B_\perp} \right| \tag{2. 20}$$

in order to minimize the spectral decorrelation due to volumetric scatter. Assuming no slopes, this value becomes 40m with 200m baseline length and therefore 16m with 500m baseline length (nominal ERS values). Hence vegetation is a major spatial decorrelation source especially with longer baselines.

In addition to the aforementioned decorrelation sources, thermal noise in the interferometric channels contributes to the coherence. For uncorrelated signal and noise in these channels, the relation between coherence and the signal to noise ratio (SNR) becomes *(Zebker and Villasenor, 1992)*:

$$\gamma_{noise} = \frac{1}{1 + SNR^{-1}} \tag{2. 21}$$

Low coherence, resulting of one or the combination of the aforementioned mechanisms, decrease the measurement accuracy and leads to phase unwrapping problems.

2.2.7   Phase Unwrapping

Phase unwrapping is possibly the most delicate step in InSAR DTM generation. It deals with solving the 2π ambiguity of the interferogram phase. As it seeks a conservative solution (i.e. independent from the integration path) for the whole interferogram, it is inevitable to divide noise corrupted areas from those where the algorithm succeeds. Noise sensitivity is a major drawback in all existing algorithms, which can be divided in three groups: the branch cut algorithm *(Goldstein et al., 1988)*, the least squares approach *(Ghiglia and Romero, 1989, 1994)* and, more recently, the minimal cost flow approach *(Constantini, 1996, Chen and Zebker, 2001)*. The branch cut algorithm is the most common and possibly still the most consistent approach up to now and will be further discussed in the following.

The basic idea of phase unwrapping is straightforward. Assumed that the phase difference between adjacent unwrapped pixels is less than $|\pi|$, the first derivative (i.e. the local slope) in each image direction is calculated and the result is integrated in both directions.

The unwrapping algorithm is realized as follows. The difference between a pixel and its adjacent neighbors in range and azimuth is calculated. For the integration, the difference is then treated by adding an integer multiple n of 2π to the phase value $\phi(r,a)$.

$$\phi_{unw} = 2\pi \cdot n + \phi(r,a)$$

(2. 22)

The weighting factor n for each adjacent pixel is derived by the examination of the phase difference $\Delta\phi$ between the actual phase value and its four direct neighbors in each direction.

$$n = \begin{bmatrix} n, & \text{if } \Delta\phi < |\pi| \\ n+1 & \text{if } \Delta\phi < -\pi \\ n-1 & \text{if } \Delta\phi > -\pi \end{bmatrix}$$

(2. 23)

The algorithm is implemented as a region growing procedure, i.e. it is repeated for each unwrapped phase, starting from an unwrapping seed point with n=0, reasonably placed in a highly coherent region.

If the initial assumption is valid (that there is no phase difference greater than $|\pi|$), the integral around a closed path is zero. This assumption is spoiled in case of pronounced decorrelation, causing phase inconsistencies. If a phase inconsistency is not prevented from entering the integration path, it will cause a systematic error throughout the unwrapped interferogram. This is the starting point for the branch cut algorithm *(Goldstein et al., 1988)*. Prior to the unwrapping, all phase inconsistencies, denoted as residues, are detected by integration around a block of four pixels (two in each direction). If the net sum does not equal zero, the block is marked as containing a residue. The residue is signed ('charged') positively or negatively, depending on the sign of the sum. As integration around a charged residue is leading to an unwrapping error, oppositely signed residues are connected, thus neutralized, by so-called cuts. The unwrapping procedure must not cross such a cut. It is obvious that the proper positioning of the cuts, connecting the correct residue pairs, is decisive for the unwrapping performance. Erroneous cuts are most likely placed in the vicinity of residue dense regions or with increasing distance of corresponding residues (Fig. 4.4). Different branch cut unwrapping approaches have been proposed *(e.g. Prati et al., 1992, Zebker and Lu, 1998)*, sharing more or less the fate of failure in residue dense regions, which have to be excluded from the procedure and leave measurement holes.

By integrating around residue dense regions, the solution of the branch cut algorithm includes mainly highly coherent phase values. The re-wrapped continuous result is identical to the original interferogram, thus possible unwrapping errors do not appear. In case of spaceborne interferometry, high noise corruption has to be taken into account, due to the common repeat pass constellation. The shallow incidence angle (layover!) of the ERS satellites and long baselines (section 2.2.10) worsen the phase unwrapping problem. Large portions of the interferogram remain inaccessible for phase unwrapping and height derivation. These portions may well include high coherent phase values, which are hence lost for further processing. Other phase unwrapping algorithms (e.g. the least squares approach) may yield a continuous solution for the whole interferogram, with similar results in coherent regions, while residue rich regions may contain quite large errors, not indicated by these algorithms.

Absolute Phase After the phase unwrapping procedure, the phases are unflattened by adding again the phase contribution of the earth curvature. One now has determined the unwrapped phase ϕ_{unw}, which differs from the absolute phase ϕ_{abs} by an integer amount of phase cycles (Fig. 2.5). As this integer amount is constant for the entire interferogram, a single ground control point suffices for its determination. As can be seen in Fig. 2.5, the absolute phase is a measure for the range difference between the satellites, which will be exploited for the phase to height conversion.

2.2.8 Height Calculation

The geometry of the interferometric height determination is illustrated in Fig. 2.9. The height h above a reference plane and the across track position y of a target are calculated with the given sensor altitude H_S and the range distance R_1:

$$h = H_S - R_1 \cos \theta \tag{2.24}$$

and

$$y = R_1 \sin \theta \tag{2.25}$$

both depending on the local incidence angle θ.
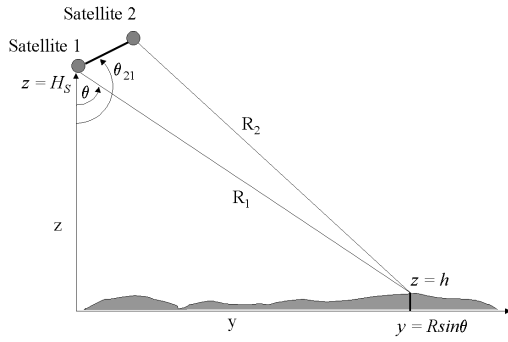
Fig. 2.9 Geometry of across track interferometry. The platform is flying in x-direction, the impact of the earth curvature is already removed.
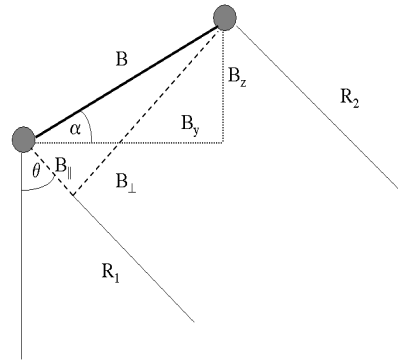
Fig. 2.10 Baseline geometry of the sensor configuration. The looking angle θ is determined with the baseline quantities B, $B_{||}$ (i.e. $\Delta R = R_2 - R_1 = \phi_{abs}\lambda/4\pi$) and α

With the baseline angle θ_{21}, or, alternatively, the angle versus the horizontal, $\alpha = \theta_{21} - \pi/2$ (Fig. 2.10), the cosine law yields

$$R_2^2 = R_1^2 - 2BR_1 \cos(\theta - \theta_{21}) + B^2 \qquad (2.\ 26)$$

yielding an expression for θ

$$\cos(\theta - \theta_{21}) = \frac{R_1^2 - R_2^2 + B^2}{2R_1 B} \qquad (2.\ 27)$$

With $R_1 \approx R_2 \gg B$ and the measured range difference ΔR (2. 12), (2. 27) becomes

$$\cos(\theta - \theta_{21}) = \frac{R_1 - R_2}{B} = -\frac{\lambda}{4\pi B}\phi_{abs} \qquad (2.\ 28)$$

which is applied to solve for the height (2. 24) and across track position (2. 25). As can be concluded from (2. 28), the precise knowledge of the baseline geometry is decisive for correct height and range positioning. Although ESA reacted to this need of the interferometric community by delivering highly precise state vector information, the orbit information of ERS still requires refinement with ground control points. Methods for baseline refinement with ground truth have been suggested by *Werner (1992)*, *Zebker et al. (1994)* and *Small et al. (1995)*.

In addition to the strict geometrical phase to height conversion, other methods for phase to height conversion using ambiguity height (section 2.2.10) and ground control points *(Small et al., 1996)* or using a height look-up table *(Geudtner and Schwäbisch, 1996)* have been proposed.

2.2.9   Geocoding

The range distance of a point on the ground $\underline{P}$, with (X, Y, Z) representing its position in the ECR coordinate space, and the position $\underline{S}_1$ of the satellite (section 2.3) is given by

$$R_1 = |\underline{S}_1 - \underline{P}|$$ (2. 29)

The along track position is determined from the Doppler relation between the sensor and $\underline{P}$.

$$f_p = -\frac{2}{\lambda}\left(\frac{\underline{S}_1 - \underline{P}}{|\underline{S}_1 - \underline{P}|} \cdot (\dot{\underline{S}}_1 - \dot{\underline{P}}) \right)$$ (2. 30)

where f_p is the Doppler frequency and $\bullet$ denotes the first derivative in respect to time.

The third equation yields the previously calculated height in combination with the ellipsoid equation of the reference ellipsoid with semi-major axis a and semi-minor axis b.

$$\frac{X^2 + Y^2}{(a+h)^2} + \frac{Z^2}{(b+h)^2} = 1$$ (2. 31)

Equations (2. 29), (2. 30) and (2. 31) allow to solve for the three unknowns of $\underline{P}$ by intersecting the range sphere with the Doppler cone and the ellipsoid.

After having repeated the geocoding procedure for all points, the ECR coordinates are converted in the desired map projection with the standard geodetic transformations. Finally, a regular grid is generated via interpolation. Depending on the amount and distribution of coherent points, typical grid sizes for the ERS case are 25m – 50m.

The generated DTM allows to geocode also thematic SAR information such as the amplitude or the coherence image.

2.2.10 Interferometric Error Budget

Gens (1998) made a first approach towards an interferometric error propagation model. In the following, the effect of phase and baseline errors on the DTM are evaluated, as they are the prevailing error sources when regarding (2. 24), (2. 25) and (2. 28).

Phase Error Depending on the coherence and number of taken looks, it has been shown *(Rodriguez and Martin, 1992)* that the phase standard deviation σ_ϕ is a function of the coherence (2. 13)

$$\sigma_\phi = \frac{1}{\sqrt{2N}} \frac{\sqrt{1-\gamma^2}}{\gamma} \qquad (2.\ 32)$$

A phase error translates into an angular error σ_θ (2. 28):

$$\sigma_\theta = \frac{\lambda}{4\pi B_\perp} \sigma_\phi \qquad (2.\ 33)$$

The differentiation of (2. 24) and (2. 25) with respect to ϕ_{abs} yields the first order height and across track errors σ_h and σ_y in dependence on the phase error σ_ϕ

$$\sigma_h = \frac{\lambda R_1}{4\pi B_\perp} \sin\theta\, \sigma_\phi \qquad (2.\ 34)$$

$$\sigma_y = \frac{\lambda R_1}{4\pi B_\perp} \cos\theta\, \sigma_\phi \qquad (2.\ 35)$$

The phase error sources (i.e. decorrelation) have been discussed in section 2.2.6.

Ambiguity height From equation (2. 34) the height $h_{2\pi}$ corresponding to a 2π phase change (single fringe) can be derived.

$$h_{2\pi} = \frac{\lambda R_1 \sin\theta}{2 B_\perp} \qquad (2.\ 36)$$

$h_{2\pi}$ is furthermore denoted as ambiguity height. The ambiguity height is a parameter, which characterizes the interferometric height sensitivity, i.e. the height change, which is resolvable with a

single fringe. The longer the baseline, the better the height is resolved, but the more fringes arise. The term 'longer baselines' denotes in the following baseline lengths longer than 250m.

For an ERS configuration with R=835km, an incidence angle θ=21° and a perpendicular baseline length of 100m, the ambiguity height is 85m. At $B_\perp$=500m, the ambiguity height is 17m. The latter being absolutely not suitable in changing terrain, where phase unwrapping will inevitably fail due to poor fringe discrimination. On the other hand, a longer baseline length means a higher phase to height sensitivity and higher InSAR DEM accuracy (2. 34).

Atmospheric Artifacts Although *Hartl (1991)* pointed out the uncertainty of signal velocity for ERS repeat pass interferometry before the start of the ERS mission, the influence especially of tropospheric changes on InSAR measurements have long been underestimated. *Goldstein (1995)* provided an analysis of SIR-C phase errors in the Mojave Desert, California, a terrain expected to favor InSAR measurements. The errors could not be related to topography and were explained from a change in tropospheric conditions during the three day repetition interval. The effects and resulting errors on different wavelengths and baseline lengths have been studied by *Zebker et al. (1997)*. They related the artifacts found in SIR-C interferograms over Hawaii to time and space variations of atmospheric water vapor. Those changes delay the travel times of InSAR measurements, hence lead to erroneous phase determination and in turn to systematic height errors. The additional two-way phase delay Δϕ caused by the atmospheric effects in terms of the travel path change Δx is given in this publication by

$$\Delta\phi = \frac{4\pi\Delta x}{\lambda\cos\theta}$$
(2. 37)

With (2. 34), the induced height error is inversely depending on the baseline length. One verifies easily with (2. 37) and (2. 34) and nominal ERS values that a 1cm travel path change causes a height error of ≈30m with a baseline length of 100m, while the same change causes an error of ≈6m with 500m. As the travel path delay is depending on the change of weather conditions between the takes, a precise quantitative prediction of the effect is practically impossible. The occurrence of seasonal variations in weather conditions should therefore be kept in mind when selecting ERS InSAR pairs. Significant variations of atmospheric water vapor during the ERS acquisition interval occur most probably in the tropical zone. *Zebker et al. (1997)* pointed out that the phase contribution due to a 20% change in relative humidity resulted in a height error of 100m with SIR

data. As conclusion from (2. 34), long baseline missions are recommended for topographic mapping in order to reduce the effects of tropospheric changes.

While atmospheric changes cause sporadic disturbances with larger baselines, their effect on shorter baselines is more prevailing. Broad fringes are superimposed, leading inevitably to severe systematic errors, due to the large ambiguity height, if they are not removed prior to phase unwrapping.

Baseline Error An error in the baseline parameters (length B and attitude α) is the result of erroneously determined orbital models (2. 4). With the connection between α and θ_{21} and (2. 28), the error in the baseline attitude σ_α equals the incidence angle error σ_θ (Fig. 2.10). Then the height error becomes:

$$\sigma_h = R_1 \sin\theta \, \sigma_\theta = R_1 \sin\theta \, \sigma_\alpha \tag{2. 38}$$

The height error in respect to the baseline length is

$$\sigma_h = \frac{R_1}{B} \sin\theta \tan(\theta - \alpha) \, \sigma_B \tag{2. 39}$$

A baseline error affects the measurements systematically. An example for such a systematic is given in section 2.2.3 and in section 4.6.3. As can be concluded from the previous equations, longer baselines are preferred for InSAR DTM generation, as with rising baseline length, the phase and baseline induced height error decreases. For ERS, the baseline length is selectable within the decorrelation limit. However, longer baselines bear two major shortcomings:

- With rising phase - height sensitivity, the measurements are increasingly prone to noise.

- The low ambiguity height causes additional unwrapping problems in changing terrain.

Both points add significantly to the well-discussed problems for SAR interferometry in changing and especially mountainous terrain. *Balan (2000)* illustrated the effects of erroneous baseline determination. Orbit information and fringe rate methods have been used to determine the baseline between two SIR-C passes over a scene in Western Ghats, India. Although a long wavelength (L-band) has been used, promising sufficient coherence, some of the resulting DTMs have been completely dominated by the systematic tilt introduced from erroneous baseline determination.

It should be kept in mind the effect of the baseline error is easily mixed up with a large atmospheric corruption. However, the baseline effect is systematic and therefore regular (e.g. tilt), while the atmospheric corruption is a random effect.

2.3 Introduction to Stereo-Optical DTM Generation

2.3.1   Overview

Continuous spaceborne digital optical image supply became available since the Landsat mission start in 1972. Since the launch of the first SPOT satellite (of meanwhile four) in 1986, stereo image pairs are available on request. The image pixelsize in the panchromatic mode is 10m, in multispectral mode 25m. DTM generation with SPOT imagery can be carried out with analogue images, derived from the digital data, using analytical stereoplotters or with the digital image product on digital stations. Due to the intensive research effort, which has been undertaken in the years after the first launch, the digital approach is considered as operational since the second half of the last decade.

DTM production with SPOT consists of three steps:

- Sensor Modeling, i.e. the determination of the imaging geometry.

- Object point measurement, by matching of conjugate image points and the intersection of their imaging rays.

- DTM interpolation.

The long-term experience with the data shows that the height accuracy, which can be expected from SPOT DTMs, is around the pixel size of 10m *(Baltsavias, 1999)*. Reasonable grid sizes are between 20m and 30m.

Since an abundance of publications on that topic are already existent, only a qualitative assessment of the main steps for SPOT DTM generation is provided in the following sections.

2.3.2   Imaging Geometry

Due to the oblique viewing geometry of SPOT 1-4 (Fig. 2.11), the stereo pair has to be acquired during different orbits, which, in the SPOT case, are at least separated by 3 days. The base to height

ratio can be estimated from the inclination of the optical axis of the sensor α_1 and α_2 during each acquisition, by

$$\frac{B}{H_s} = \tan \alpha_1 + \tan \alpha_2 \tag{2.40}$$

SPOT carries 4 linear array line sensors with altogether 6000 pixels forming a line in the image x direction (Fig. 2.11). An image consists of 6000 lines, all having their own exterior orientation parameters (3 each for the perspective center and attitude). The relation between object and image coordinates is given by the collinearity equations of a line.

$$\underline{P} - \underline{X}_{ol} = \kappa \mathbf{R} \underline{x}_l' \tag{2.41}$$

and

$$\underline{x}_l' = (0, y_l', -c) \tag{2.42}$$

where $\underline{P}$ is the object point vector, $\underline{X}_{ol}$ the coordinates of the projection center, κ the scale factor, $\mathbf{R}$ the rotation matrix, c the camera constant and y_l' the image line coordinate in respect to the center of the line.
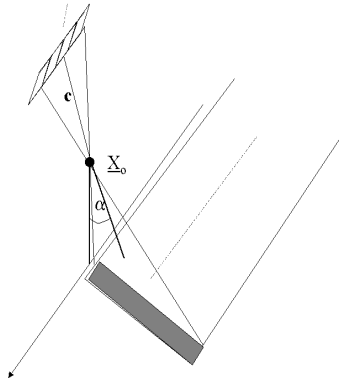
Fig. 2.11 SPOT image acquisition geometry. 4 CCD line sensors are mounted in the focal plane.
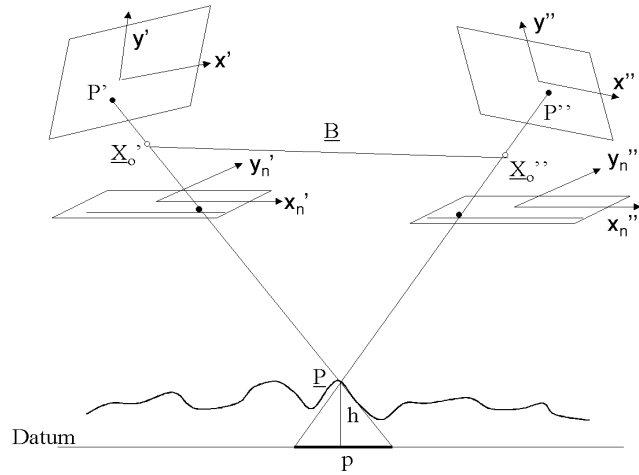
Fig. 2.12 Epipolar geometry and point matching. By taking advantage of the epipolar geometry, the search space reduces from 2D to 1D.

Due to the relatively smooth satellite orbit, the exterior orientation parameters are highly correlated from line to line, allowing to model their change during the acquisition in terms of the y direction

(time). Over the years, different models have been developed and applied both on analytical stereoplotters *(Konecny et al., 1987)* and digital stations. Two general model classes can be distinguished. One approach approximates the orientation parameters using polynomials of first to third order *(e.g. Forster et al., 1987, Li and Cheng, 1988)*. Stricter models describe the platform movement with a precise mathematical model *(e.g. Toutin, 1985, Dowman et al., 1987, Kratky, 1989)*. The high geometric accuracy, which is obtained for a single model in this way, can also be achieved with SPOT image strips *(Dowman, 1991)*.

The amount of the required ground control points depends on the applied model. Generally, 6-10 points suffice for determining the image geometry with the strict model, while the polynomial approach requires obviously more points. If several SPOT images in a strip are processed, block adjustment reduces considerably the need for ground control *(Grün, 1986a, Dowman, 1991, Veillet, 1992)*.

It is worth noting at this point that, in contrast to SAR interferometry, there is no absolute need for auxiliary data such as orbit information in order to determine position and attitude. However, they can be used as approximations or in order to reduce the number of ground control points. The required number of ground control points for setting up the imaging geometry has often been stated as disadvantage of stereo-optical DTM generation. Nevertheless, it has been shown that large SPOT blocks can be adjusted with the same amount of control points which are needed for a single model *(Veillet, 1992)*. Repeat pass SAR interferometry (spaceborne) needs approximately the same number of control points for baseline adjustment for a single model. The required control point accuracy in order to avoid a systematic height error (section 2.2.10) is higher than in the SPOT case, where the point accuracy is several meters *(Dowman, 1991, Durand, 1995)*. In addition, accurate ground control point identification is certainly more cumbersome in SAR images than in their optical counterparts.

2.3.3 Point Measurement

Since the orientation has been determined for both images before, an object point can be determined by identification of its image coordinates and subsequent intersection of the corresponding image rays. Although the measurement of conjugate points can be carried out both manually and automatically, the sheer size of a SPOT image favors the automatic approach to build a DTM. Generally, the automatic point matching is performed by finding the maximum similarity by computing the cross correlation between the images using a selected image patch. However,

computational expense due to the image size, radiometric differences between the images and ambiguous matching results force for a more sophisticated matching procedure.

Epipolar Geometry After the orientation of the images, the image rays of conjugate points intersect in the object point. The perspective centers, the image points and the object point are part of the same plane, the epipolar plane (Fig. 2.12). In contrast to the perspective images, the epipolar lines are curved in case of linear pushbroom images (e.g. of SPOT), as the perspective centers are changing from line to line (*Kim, 2000*). However, it has been shown that straight epipolar lines may well be approximated for SPOT with a very small error *(Baltsavias and Stallmann, 1992)*. This geometric constraint reduces the 2D search space to a single line, the intersection of the epipolar plane with the image plane of the second image. Thus, the normal case can be approximated, if the images are resampled along the epipolar lines. The search along a single line increases success rate and reliability apart from being much less computational expensive than the 2D search.

Matching The success of the matcher depends on its ability to discriminate features (e.g. gray level gradients) in the neighborhood of a pixel. The basic approach of computing the cross correlation just based on arbitrarily chosen gray level patches performs weak especially in the SPOT case, where strong radiometric differences between the images occur due to the repeat pass interval of several days or even weeks. It is therefore advantageous to extract possible point candidates prior to the matching with so called interest operators. The Förstner operator takes e.g. the local SNR, texture or gray level gradients into account when searching for the candidate points *(Förstner, 1986)*. Different matchers have been proposed, among them the adaptive least squares matching *(Grün, 1985)*, based on 6 affine transformation parameters, and its extension, multiphoto geometrically constrained matching *(Grün, 1985, Baltsavias, 1991)*. The accuracy of the method has been repeatedly reported to be clearly in the subpixel range *(e.g. Grün, 1986b, Angleraud et al., 1992, Baltsavias and Stallmann, 1993, Fraser et al., 2001)*. A comparison with other methods is given in *(Day and Müller, 1988)*.

The result of the matching process, accuracy and density of measured points, decide about the accuracy of the DTM. High correlation values are generally a qualitative indicator for successful matching, although point mis-matching may still occur (e.g. presence of regular patterns on the ground). The error equations of the normal case *(Kraus, 1982)* serve as a first approximation of the measurement error and indicate the direct proportionality between matching accuracy and both altimetric and planimetric accuracy.

Space Intersection After having determined the image orientation and carried out the image matching, the object point vector is found by forward intersection (Fig. 2.12). Mathematically, the object point is determined by solving the collinearity equation (2. 41) of each image. The result is in most cases an irregular grid of points, which needs to be interpolated to an evenly gridded DTM.

Backprojection from object to image coordinates allows additional consistency checking.

A faster (yet less strict) method for height calculation is to measure the parallax in the epipolar images and convert it directly to height by polynomial fitting. As a first approximation the parallax is proportional to elevation. The parallax to height conversion is then performed with help of ground control points and the corresponding parallaxes. Based on these points, the parallax-height relation for the whole image is modeled as a polynomial. The polynomial coefficients are calculated using the ground control points *(Teguh, 1994)* and applied to convert the measured parallaxes to heights. A similar approach for phase to height conversion using unwrapped phases (instead of the parallaxes) exists in SAR interferometry (section 2.2.8).

2.3.4   DTM Interpolation

The DTM is interpolated from the irregular distributed points in a final step. Typically, this is performed by fitting a polynomial through the measured points in order to approximate the local surface. Various interpolation methods exist. Reviews are given e.g. in *Schut (1976)* and *Kraus (2000).*

As stated above, the interpolation result is strongly depending on the accuracy, density and distribution of matched points. The results also vary with the interpolation method used. Before interpolation, the stereo DTM is edited in order to remove eventual mismatched points, appearing as local spikes, and to remove the influence of the terrain on the height measurement (e.g. woods).

2.4 Comparison of InSAR and Stereo-Optical Height Measurement

ERS and SPOT "see" different parts of the spectrum. Due to the wavelength, SAR microwaves penetrate through clouds, but interact on the other hand with surface features of comparable size, which makes repeat pass InSAR DTM generation that change sensitive. In contrast to SPOT, the less the texture, the higher the coherence and therefore the higher the measurement accuracy of InSAR and vice versa. Short SAR wavelengths (e.g. X-band) are plagued with that sensitivity, but offer higher resolution and accuracy (2. 34) than the long wavelength systems. Longer SAR wavelengths (e.g. L-band) are uniquely able to penetrate the vegetation, thus deliver measurements

from the earth surface instead of the canopy thus saving work for DTM editing. C-band, on which ERS operates, is somehow a compromise between long and short wavelengths. ERS InSAR range measurement is capable to deliver the height for every pixel, which compensates the lower resolution of the system in comparison to electro-optical sensors (such as SPOT), which depend on recognizable features for the matching. In addition, the change sensitivity has been treated with the one day repeat pass interval of the tandem mission. In this way, ERS InSAR is capable to deliver DTMs of the same grid as SPOT, but from images, which offer less resolution.

An advantage of the stereo-optical method is the measurement geometry. The collinearity equations relate the image to object coordinates. Such a strict interrelation does not exist in the InSAR case, which is on the contrary strongly dependent on the precision of the satellite state vectors in order to determine the baseline angle and length. In fact, the ERS orbit information is considerably more accurate than SPOT ephemeris data (*Renouard and Perlant, 1993*). Precision of the position and attitude information remains an issue of future optical sensors in order to reduce the amount of required ground control points. Theoretically, a single ground control point suffices for SAR interferometry in order to determine the absolute phase. However, in practice, several points are required in order to adjust the InSAR baseline ((2. 38) and (2. 39)). The accuracy of ground control point matching in ERS SAR imagery is yet hardly examined.

In case of the oblique viewing geometry, the sharp intersection angle of the two image rays is less prone to errors and determines the point location much clearer than the intersection of three rotation bodies, which are needed to locate the point in the InSAR case (section 2.2.9). SPOT stereo DTM generation also faces problems in steeper terrain *(Theodossiou and Dowman, 1990)*, but these are less pronounced than the InSAR layover problems, especially due to the shallow viewing angle of ERS.

The similarity between matching and the calculation of the phase difference has often been pointed out. In fact, the change of the corresponding entity (location, phase) between two images of the same point is exploited in both approaches for height determination. However, while matching in the optical case is the most critical step, the InSAR phase difference measurement process can be carried out virtually unimpeded. The phase unwrapping procedure, in principle a postprocessing step, is the true obstacle for the InSAR process.

Due to the very similar acquisition positions, the registration accuracy of InSAR images is comparable to the best matching results. When properly performed, the remaining misregistration

is of almost no importance when calculating the response in highly correlated regions (i.e. adjacent pixels have almost the same response). In this way, the achievable accuracy of InSAR in these regions (2. 32) is much higher than in the stereo-optical case, where only features and not actual pixels can be matched. Radiometric differences, originating from the considerably different viewing positions (and acquisition times) hinder the exact point identification in the optical case. Furthermore, InSAR is at a first glance superior in respect to the measurement density, since the phase difference is calculated for each point. Also InSAR reliability is superior, since the required filtering process and the residual detection prevent outliers from entering the unwrapping process.

The usage of image patches rather than the single point response is on the other hand the great strength of the stereo measurement principle, as it becomes less dependent on slight changes. As long as there is enough unchanged texture (in its vicinity), a *patch* (point) remains identifiable for the matcher. In addition, typical features (e.g. edges, crossroads) show relatively stable radiometric properties. In contrast, slight changes (in cm scale for ERS) in the backscatter geometry of a imaged *pixel* suffice to turn it unusable for interferometric height measurement *(Zebker and Villasenor, 1992)*. The repeat pass problematic - the ground and atmospheric change sensitivity - limit seriously the use of spaceborne SAR interferometry. As a first approximation, the more texture, the more problems arise for interferometry, certainly a source for synergism with the stereo-optical measurement principle. Table 2.2 summarizes the discussed points:

	SPOT	**ERS**
Orientation Parameters	Position, attitude and scale	Position and velocity of sensor
Point determination	Intersection of two imaging rays	Intersection of three rotational bodies
Measured entity	Parallax	Phase difference
Principle	Feature matching, patch-wise	Phase difference calculation, pixel-wise
Height accuracy	Subpixel-size	Clear subpixel-size
Error characteristic	Local	Systematic

Tab. 2.2 Comparison between SPOT and ERS DTM generation.

One concludes that although, or just because, the achievable height measurement accuracy of SAR interferometry is significantly higher than its stereo-optical counterpart, it is much more error sensitive. SAR interferometry tends to fail globally, due to erroneously determined imaging geometry, atmospheric effects or phase unwrapping errors, whereas stereo-optical point measurement fails by its nature most likely locally, as there are less problems with the geometry. Due to that robustness, stereo measurements are expected to produce at least a coarse grid even under less favorable conditions. The repeat pass problematic will be overcome by the new

generation of along track stereo-imaging systems (e.g. SPOT 5), while this remains an issue with spaceborne SAR interferometers.

2.5 Multisource DTM Generation

Exploitation of redundancy increases the reliability of the height measurement process in both the optical and SAR case. Photogrammetric strip processing is a routine operation in the airborne case and is also applicable to spaceborne optical imagery from SPOT *(Veillet, 1990)*, MOMS *(Kornus et al., 2000)* or Landsat *(Toutin, 2001)*. The common problem with acquiring strips of repeat pass spaceborne optical stereo pairs is their insufficient availability in many parts of the world. Furthermore, the cost of a SPOT stereo pair and its processing is considerably higher than the cost of an ERS SLC image pair. Cost must especially be taken into account if regular update is intended or if the initial results are unsatisfactory.

Block adjustment has not been examined in such detail in the SAR case, despite the fact that InSAR DTM generation would certainly profit for the reasons stated in the previous sections. ERS strip adjustment has been performed in large mapping projects such as the British Landmap project *(Morley et al., 2000)*. In order to achieve an accurate DTM result with repeat pass SAR interferometry generally 6-10 interferograms are required *(Bamler and Hartl, 1998)*.

Two main reasons for applying several interferograms for topographic mapping can be found.

Firstly, several measurements of the same entity enable the exploitation of the high degree of redundancy. If up to 10 measurements taken with different baselines are available, phase, or height, respectively, can be estimated with help of common estimation techniques, e.g. maximum likelihood *(Ferretti et al., 1997)*. This approach is intriguing, due to high availability and the, in comparison to optical data, low price of SAR data. On the other hand, the long acquisition period for so many scenes and the computational expense for combining them limit the use of this approach in many cases.

Secondly, combination of ascending with descending interferograms has been proposed in order to overcome the distortion effects originating from the image acquisition geometry *(Carrasco et al., 1997)*. Affected regions are detected with help of coherence and replaced with measurements from the opposite track. This technique works with isolated, but not too steep slopes, which otherwise cause shadow effects in the counterpart. However, mountainous terrain is not resolvable with both passes and still needs manual intervention for determining the cuts in residue dense regions.

Additional problems arise, if passes of long and short baselines are combined, because of the different accuracy of the measurements.

Both, the combined use of radargrammetric and interferometric SAR *(Crosetto and Perez, 1999)* and the combination of stereo-optical and stereo-SAR *(Toutin, 1995)* have been proposed. The use of radargrammetry together with interferometry is certainly a data fusion option for the future. At present, spaceborne radargrammetry performs weaker than photogrammetry and offers a lower accuracy potential than interferometry *(Leberl, 1999)*.

The use of mixed SAR and optical imagery has also been examined. *Renouard and Perlant (1993)* exploited the relatively high orbit accuracy of ERS in order to improve the geocoding of SPOT imagery. Topographic mapping with a Radarsat – SPOT image pair has been studied by *Goncalves and Dowman* (*2001*). The height accuracy has been better than with a SPOT stereo pair, due to strong intersection geometry, if a same side looking optical and SAR image pair is used. However, the speckle effect in SAR imagery hinders the matching of sufficient points for DTM generation with such an image pair, although certain features appear similar in both images and can be used for matching (*Dare and Dowman, 2000*).

The combination or fusion of spaceborne stereo optical and InSAR height measurements has been scarcely examined throughout the years. *Perlant (1992)* gave an early example of SPOT and ERS being complementary in respect to map production. A comparison of ERS-1 and SPOT performance over two sites in Utah is given in *(Renouard et al., 1995)*, again the complementary properties of both sources have been pointed out. *Tannous et al. (1996)* proposed the fusion of any kind of 3D information using a Bayesian framework. They tested the approach with a coarse DTM and ERS interferometric and ERS stereo data. An other approach for fusion is to use existing measurements as datum for the InSAR measurements. A very popular method is to flatten an interferogram, i.e. to remove topographic fringes with the stereo DTM in order to ease phase unwrapping. *Feretti et al. (1999)* used a SPOT DTM as datum for fusing several InSAR terrain models using wavelets.

2.6 Summary

In this chapter, the basic principles and processing steps for ERS InSAR and SPOT DTM generation have been introduced. InSAR measures the absolute phase difference between two SAR images, which is used for solving the viewing geometry of the sensor configuration and in this way

for determining the object point coordinates. InSAR is not dependent on the identification of image features, but measures the height pixel-wise. Therefore, ERS is capable to deliver an amount of point measurements at least comparable to SPOT, despite its lower resolution. Three major ERS InSAR DTM error mechanisms have been identified and quantitatively assessed. Firstly, tropospheric changes during the repeat pass interval delay the travel time of the SAR signal and add to the measured phase. Secondly, decorrelation corrupts the measured phases and obstructs the phase unwrapping. Thirdly, the limited precision of the satellite orbit during the data takes. Decorrelation and the resulting problems for phase unwrapping are much discussed InSAR issues, as common unwrapping approaches perform rather weak in presence of noise. These problems are local (although their effect on unwrapping may be systematic) and have to be treated as random errors. On the other hand, baseline errors and large atmospheric changes during the passes have a systematic effect on the DTM. Their effect on the InSAR DTM is similar. ERS SLC image resolution is approximately half of the resolution of SPOT imagery, which is in addition easier to interpret. The accuracy of the ground control points depends on the reference (e.g. map) and will hardly surpass the resolution of the ERS image. Quality and quantity of ground control points for ERS DTM generation are therefore compromised. If ground control points of limited accuracy are used for orbital adjustment, the determination of the exterior orientation is erroneous, which causes a systematic error in the InSAR measurements. Hence, regular errors will be furthermore denoted as baseline errors. However, it remains an issue to find a procedure which discriminates atmospheric and baseline effects.

SPOT DTM generation behaves in many ways complimentarily to ERS InSAR. It is less prone to systematic errors, as its imaging geometry is well modeled. On the other hand, matching problems especially with repeat pass images affect the DTM accuracy locally. The problems in steeper terrain are less pronounced with SPOT, while flat and slightly textured terrain favors InSAR. The existing approaches of combining SPOT with comparable SAR data have been mentioned. With regard to this complimentarity, the cost for SPOT imagery and the large amount of ERS scenes required for achieving satisfactory DTM quality, the combination of an existing SPOT DTM with ERS InSAR measurements appears as an interesting option for high quality spaceborne DTM generation. InSAR DTM processing will profit from redundant information in similar scale as it is usable to reduce its sensitivity to systematic errors. After reduction of these errors, the achieved high InSAR measurement accuracy helps in turn to improve the SPOT DTM.

C h a p t e r   3

CONCEPT FOR THE FUSION OF STEREO-OPTICAL AND INSAR MEASUREMENTS

3.1 Introduction

This chapter introduces a concept for the fusion of a SPOT DTM with ERS InSAR data. The following section sets up the fusion terminology. The terms of reference must be defined, as the literature is not consistent in terms of data fusion. Therefore, the key terms data fusion and quality are explained and defined for this fusion scenario. The concept for the fusion of interferometric and stereo-optical measurements is introduced in section 3.3. The fusion problem is formulated for the combination of measurements of different sensors in order to achieve an improved result. This formulation yields to the well-known engineering problem of fusing observations from different sensors, whose solution also applies in the discussed case. The problem is solved by breaking it into three core parts, data alignment, association and estimation, which are highlighted in the sections 3.4 - 3.6.

3.2 Terms of Reference

3.2.1 Data Fusion

The term 'Data Fusion' is not standardized at all. In common use, there is no distinction between 'Data Fusion' from other related terms like 'Data Combination', 'Data Integration' or 'Data Merging' *(Buchroithner, 1998)*. Even the interpretation of the single terms 'Data' and 'Fusion' is strongly dependent on the application and view of the individual.

The advent of the increasing amount of remote sensing data in the recent decade and the ever rising need for higher data quality urged for a more precise definition of the term. Following the scheme of the blurred terminology, several definitions have been proposed. A good review of definitions is given in *(Wald, 1998)*, where also the definition of the *U.S. Department of Defense (1991)* is stated that '*data fusion is a multilevel, multifaceted process dealing with automatic detection, association, correlation, estimation and combination of data and information from multiple sources* '. This strict definition of operations, which are performed for data fusion, applies well to the discussed case. It refers to the typical military problem of fusing positional data from different sensors.

What actually is missing in this definition, is the definition of the fusion goal, being adopted by the definition of the EARSeL Special Interest Group 'Data Fusion' *(EARSeL, 1998, Wald, 1999)*: '*Data fusion is a formal framework in which are expressed means and tools for the alliance of data originating from different sources. It aims at obtaining information of greater quality; the exact definition of 'greater quality' will depend upon the application* '. This rather general definition needs specification for discussed case, which deals with 3D geometrical data. Additionally, the desired quality has to be specified.

The terms 'Geometrical Data Fusion' or 'Positional Data Fusion', are best describing the addressed problem. The Geometrical data fusion problem may be defined by: *finding the positional vector closest to reality within a reference system by favorably combining the related observations.* The word 'favorably' depends on the quality, which is specified in the follows.

3.2.2 Quality

Much like the data fusion terminology, quality is a completely subjective term. It has to be defined *before* each fusion process, which consequently has to be optimized in respect to match the desired quality. In this way, quality - and its increase - is the 'raison d'être' of data fusion itself, as all participating data do obviously not deliver data of the desired quality, or, without redundancy, it is not clear if they do.

The reasons for fusing DTM data from different sensors are many.

- The accuracy of the existing data is not sufficient.
- An update and revision of existing databases with more recent data is required.
- New measurements enhance a sparse database.

- Individual sensor/technique limitations shall be overcome.

- Data fusion saves data and processing time, thus reducing cost.

These points may be summarized to two main criteria: increase of measurement accuracy and increase of the amount of accurate measurements. These criteria define in the discussed case the quality of the resulting DTM and specify the term 'greater quality' in the EARSeL definition. The fusion algorithm must be designed in order to match these criteria. Although different quality criteria are applicable for DTMs, this work concentrates on the quantitative improvement of the measurements.

The specifications for DTM quality are e.g. given in *US Department of the Interior (1992)* that distinguishes between the planimetric and altimetric DTM accuracy. The planimetric (horizontal) accuracy is assessed by features found in an ortho-image, generated with the DTM, or with the DTM itself, by identifying typical topographic features.

The altimetric (vertical) accuracy of a DTM is assessed with the root mean square (rms) error, which is defined as

$$\text{rms} = \sqrt{\frac{\sum_{i=1}^{n}(H_i - H_{ri})^2}{n}}$$

(3. 1)

where H_i are the measured (or fused) DTM heights, H_{ri} are the reference heights (e.g. check points, national DTM database) and n is the number of compared points.

For reasons of completeness, the formulae for the bias μ and standard deviation σ are listed below.

$$\mu = \frac{1}{n}\sum_{i=1}^{n}(H_i - H_{ri})$$

(3. 2)

$$\sigma = \sqrt{\frac{\sum_{i=1}^{n}(H_i - H_{ri} - \mu)^2}{n-1}}$$

(3. 3)

In contrast to mean and standard deviation, the rms error expresses both the systematic and the random error, being two out of three DTM error types:

- The systematic error, which occurs due to a system inconsistency and is of constant magnitude and sign.

- The random error, which is unpredictably occurring with different magnitude and sign throughout the DTM.

- Blunders, or outliers, which are errors of major proportions, larger than three times the standard deviation.

These errors are also summarized as first order quality criterion *(Durand, 1995)*. The second order criterion is more qualitative, comprising the terrain shape or features (e.g. slopes, curvatures). The further work focuses mainly on the first criterion, although terrain shape modeling is certainly also an fusion issue, as e.g. InSAR generally delivers denser measurements than the stereo optical method. For simplification, it is assumed that accurate and dense measurements resulting from the fusion process will help tackling the second criterion, too.

In this context, it should be mentioned that the fusion result is not necessarily a final product, but an output of both measurement processes combined. The result is mathematically the best fitting result to both underlying observations. Further "value adding" processes like DTM editing (e.g. for the removal of the influence of landcover) and interpolation may be applied.

Synergy Synergy is an important term in connection with quality. Synergism according to Merriam Webster means: ' *interaction of discrete agencies (as industrial firms), agents (as drugs), or conditions such that the total effect is greater than the sum of the individual effects* '. In other words, the better the data synergy is exploited (e.g. during the fusion process), the better is the effect (e.g. quality of the result). On the other hand, one can certainly fuse non-synergetic data, but the quality of the result then remains lower than in the synergetic case. This also means that besides the fusion procedure itself, data synergy determines the quality of the result. Hence, given an optimal fusion environment, results may differ, depending on the data synergy. According to the positional data fusion definition, given in section 3.2.1, the best result is achieved, if the data synergy is exploited.

3.3 Concept for the Fusion of Interferometric SAR and Stereo-Optical Measurements

3.3.1   Goal

As pointed out, the fusion goal is the improvement of quality of SPOT DTMs by fusing them with ERS data. The product of this fusion process has to be significantly superior to the stand-alone data in respect to the formulated quality criteria in order to justify the fusion expense. Therefore, prior to the actual data fusion, four points have to be cleared in order to achieve that improvement:

1. Which are the quality criteria, which the existing database does not match?

2. Which is the synergy between the data?

3. Is the synergy between the database and the InSAR measurements sufficient to improve the quality according to 1. ?

4. How is the synergy optimally exploited?

Answering these questions sets up the fusion goal and by what means it is achieved. It determines how the data are combined in order to generate a fused product with improved quality in comparison to the single sensor data sets. The problems with stereo-optical and InSAR DTM generation have been stated in chapter 2. Goals of DTM fusion are e.g. the increase of DTM accuracy for the derivation of contour lines for map production or the increase of valid measurements for ortho-image production.

After the definition of the goal, the data fusion concept can now be formulated, which answers the aforementioned questions.

3.3.2   Concept

The DTM fusion problem is a time independent variant of the problem of combining observations from different sensors to a single expression. The common fusion result can be of many types, e.g. a decision or a qualitative or quantitative expression. The fusion issue typically arises in target recognition or target tracking problems. The discussed case deals with measurements from different sensors, from different acquisition times and resolution. Although the underlying imaging principles and measurement techniques are completely different, both measure the 3D coordinates of points.

Positional data fusion concepts have been proposed e.g. by *Waltz and Llinas (1990)* or *Hall (1992)*. They deal with combining observations from different sensors in order to estimate an object state vector, e.g. position and velocity. Applied to the InSAR/stereo-optical case this means that after data acquisition from both sensors, the observations are submitted to three procedures in order to achieve a best estimate: data alignment, data association and estimation (Fig. 3.1).

Firstly, it has to be ensured that both measurements share the same geometry and units. A typical problem when fusing DTMs in different projections or introducing an existing DTM in map projection into the InSAR DTM generation process being in the Range-Doppler geometry. Thus, a common reference system has to be defined and the data are aligned with that reference system.

Secondly, the aligned data sets are grouped in order to prepare them for the fusion process. In the simplest case, such a group consists of a pair of InSAR and the corresponding stereo-optical point coordinates. In order to increase the redundancy, the neighboring measurements can be included. The association aims at determining, if the measurements belong to the same point. Therefore, the grouping has to be performed according to some distance metric, which represent the similarity of the observations. The similarity declaration is based on a maximum allowable distance. By comparing the similarity with this threshold, observations are associated to each other or sorted out from the fusion process, such reducing the complexity of the following estimation step.

Thirdly, estimation combines the grouped observation to the final result. It finds a solution, which fits best to the multiple observations. Basically, this is an adjustment problem, which is treated with the applying mathematical model. The adjustment procedures are a special realization of statistical estimation with a priori given mathematical model *(Mikhail, 1976)*. The least squares estimation procedures, which suit the discussed fusion scenario, are prediction and interpolation. Prediction is commonly performed in time variant processes in order to estimate the future state vector of a system. As the estimation is based on observations, prediction applies well to the discussed case of having a priori stereo-optical DTM information. Note that the InSAR Range-Doppler geometry and phase measurements are as well functions of time. In location dependent systems, interpolation is used for the estimation task. The option of not only estimating unobserved locations but also filtering existing ones makes it of special interest for the stereo-optical and InSAR DTM fusion.
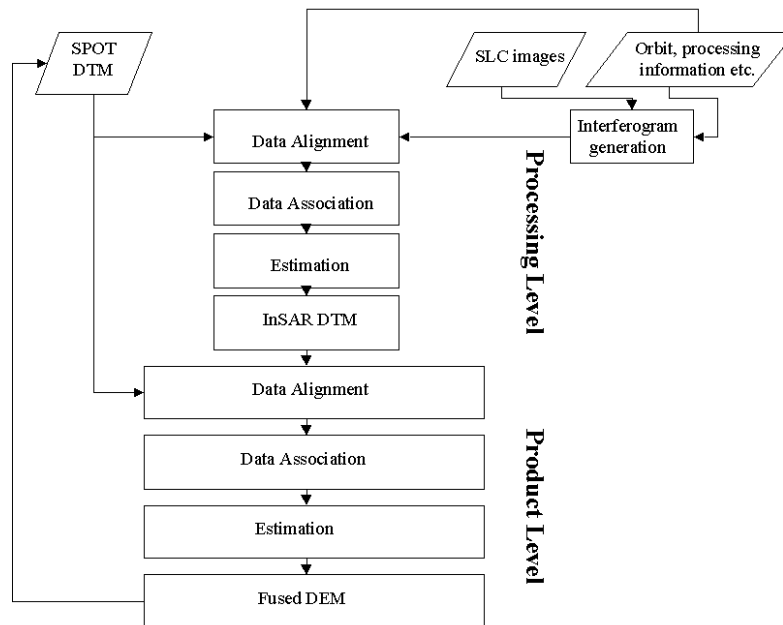
Fig. 3.1 The data fusion concept. The SPOT DTM and the ERS measurements contribute to the fusion process, which comprises of an alignment procedure, the data association and the estimation. Data fusion can be carried out during the InSAR processing and on the DTM product level.

3.3.3   Strategy

In principle, the data fusion can be carried out on three levels: on the sensor level, on processing level and on product level. Reasonable for InSAR and stereo-optical data fusion is the fusion during the InSAR generation process and on the common product level, the DTM (Fig. 3.1).

Fusion during the InSAR DTM Generation Process If stand-alone InSAR DTM generation is not feasible with appropriate results, preexisting height information is applied to overcome the limitations. Problems arise typically with spaceborne SAR interferometers from the repeat pass configuration and/or the need for precise determination of the baseline. Spaceborne SAR interferometry has meanwhile proved its measurement capabilities. DTMs with less than 3m rms error have been generated *(Small, 98)* under very well maintained conditions (e.g. flat terrain, corner reflectors). Hence, the generation process does not need enhancement as a whole, but it is sufficient to concentrate the fusion on certain critical steps like noise reduction, phase unwrapping and phase to height conversion. For that purpose, the stereo-optical measurements have to be

projected to the SAR Range-Doppler geometry and may serve as approximation at the following stages of InSAR DTM generation:

- Reduction of phase noise

- Detection of atmospheric artifacts

- Phase unwrapping process

- Phase to height conversion

- Correction of orbital state vectors

- Geocoding of the InSAR DTM

If a fusion at DTM product level is still intended, one should minimally interfere with the InSAR measurement process. An option, depending on the original stereo quality, is to use in a first step only approximations for fusion for the enhancement of the generation process and fuse the resulting DTM with the database in a second step. In this way, the redundancy of independently measured heights is preserved as far as possible, while the InSAR DTM generation is yet enabled. The use of approximations takes the existing database errors into account and prevents them to leak into the measurement process. It will be shown in chapter 4 that approximations are enough to overcome the systematic effects, originating from baseline and atmospheric errors, which will otherwise turn the InSAR measurements unusable for data fusion. In addition, it will be shown that approximations suffice to constrain the phase unwrapping process, preventing it from failure.

DTM Fusion The InSAR height measurements are fused with their optical counterparts on the DTM product level. This is the straightforward fusion application, as the DTM is the output of both techniques. Moreover, it is less complex than the interference of the SPOT heights with the InSAR measurement process. In contrast to the fusion during the InSAR processing, which is solved in a prediction manner, both estimation options, interpolation and prediction, apply for the fusion on the DTM level. For the interpolation, the measurements are treated equally as independent observations of the same point, while for prediction, a certain knowledge about the quality of the existing SPOT measurements is assumed. Prediction is an interesting option when fusing DTMs of different grid sizes.

3.4 Data Alignment

Data alignment ensures that the data sets are in the same frame of reference, i.e. they share the same geometry and refer to the same units. The required geometry depends on the application. The conversion from DTM map coordinates to SAR image coordinates and vice versa follows the scheme outlined in Fig. 3.2.
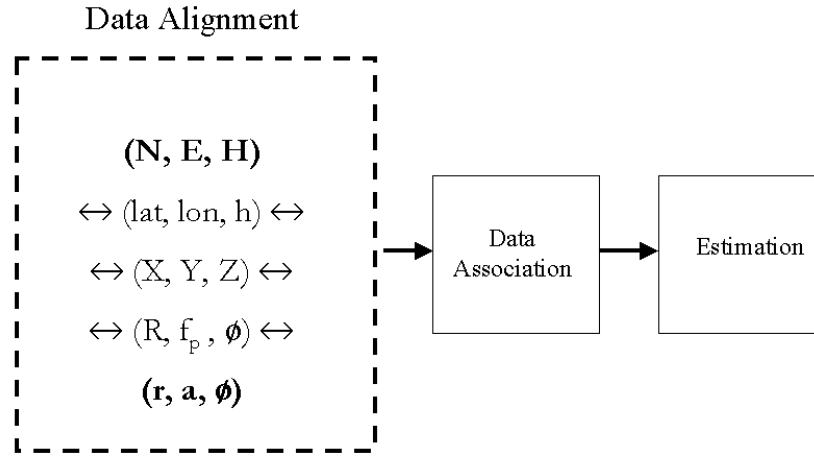
Fig. 3.2 Conversion scheme from map coordinates (northing, easting, height) to SAR image coordinates (range, azimuth, phase)

The northing, easting and height coordinates are transformed to spherical coordinates in latitude, longitude and height above the reference ellipsoid. A broadly used ellipsoid is the WGS84 to which not only the measurements of the Global Positioning System (GPS) refer, but also the orbital state vector information from most ERS processing and archiving facilities. After conversion to the same geocentered X, Y, Z system as the orbit ephemeris data, the DTM is in the same reference frame, allowing baseline correction or determination of the unwrapping phase constant. The connection between the X, Y, Z coordinates and the Range-Doppler geometry and in turn with the SAR image coordinates has already been shown in section 2.2.9.

Qualitative interferometric analysis can be performed already at this stage by interferogram simulation using the DTM *(Hagberg and Ulander, 1993)*. If applicable, the optimal system parameters (e.g. wavelength, baseline) for InSAR DTM generation can be computed and determine the choice of the SAR system. Up to now, one may choose between different SAR sensors (e.g. ERS, RADRSAT, JERS) having different viewing angles, wavelengths and baselines.

3.5 Data Association

After coordinate and unit conversion, the measurements are in a common frame of reference. Having the same geometry does not tell that measurements originate from the same height. For example, stereo methods directly measure the vegetation canopy height, while SAR penetrates the vegetation, depending on the wavelength, resulting in lower height measurements for the same point *(Small, 1998, Ulander et al., 1995)*. This problem is less pronounced with X- and C-band SAR systems, but becomes increasingly problematic with longer wavelengths (e.g. L-Band), as a different target is measured.

The association process consists of three major procedures. Possible fusion candidates are selected and screened during the gating process, which determines their similarity with help of a distance metric (Fig. 3.3). Finally, an assignment instance decides, if the measurement belong to the same target, i.e. if they are similar or not.

The output of the association are the measurements, grouped together according to their similarity, but reduced by sorted out erroneous measurements. It has to be pointed out that at this stage systematic errors are detected and removed in order to prevent their leakage into the estimation process. This applies especially to the baseline and atmospheric errors, corrupting InSAR DTM generation.
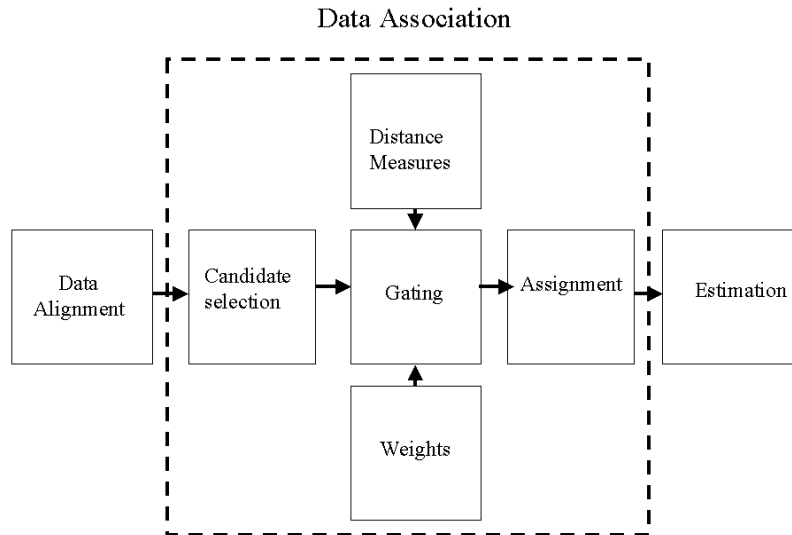

Fig. 3.3 Association serves to group the aligned data to similar measurement pairs. It reduces the amount of measurements by selecting only similar ones from all possible candidates. Similarity is determined with help of the distance of each measurement from an observation model.

3.5.1   Candidate Selection

While the alignment process converted only geometry and units, actual fusion candidates are selected during the first step of association. Globally, it is secured that the database encompasses the image or frame boundaries, outlying measurements are sorted out. In case of incomplete databases, regions, missing measurements, are excluded from the association procedure. Locally, the neighborhood condition is determined, according to which the data are associated (e.g. pointwise, nearest neighbor).

3.5.2   Gating

Error recognition and exclusion from the estimation is a goal of the association process. Gating prevents outliers from penetration of the estimation process, being very sensible to outliers, by calculating their similarity. For that purpose, a confidence bound is defined, beyond which the measurements are rejected and labeled as erroneous. Inside this bound, the similarity of measurements according to some metric is defined.

Other types of existing information can be included in the gating process. A typical example are weights, derived from the different measurement processes.

Similarity measures Finding the same feature or object in images from different sensors, thus finding their similarity quantitatively, is a challenging task in many applications (e.g. feature matching). When dealing with quantitative entities, like height measurements or phases within the same reference system, the similarity declaration is much facilitated.

Distance The straightforward quantitative measure of association of two vectors $\underline{f}$ and $\underline{g}$ is their Euclidean distance d

$$| d | = | \underline{f} - \underline{g} | \tag{3.4}$$

which reduces in the DTM case to the difference in height in case that the measurements are in the same grid.

Covariance The covariance plays an important role in similarity declaration and the following estimation.

The variances and covariances of a vector of random variables $\underline{f}$ are summarized in the auto-covariance matrix $\mathbf{K_{ff}}$ being

$$\mathbf{K_{ff}} = E\{(\underline{f} - E\{\underline{f}\})(\underline{f} - E\{\underline{f}\})^T\} \tag{3.5}$$

Similarly, the covariances of two vectors $\underline{f}$ and $\underline{g}$ are summarized in the cross-covariance matrix $\mathbf{K_{fg}}$, being

$$\mathbf{K_{fg}} = E\{(\underline{f} - E\{\underline{f}\})(\underline{g} - E\{\underline{g}\})^T\} \tag{3.6}$$

Correlation Coefficient The local correlation coefficient ρ_{fg} ($|\rho_{fg}| \leq 1$) between $\underline{f}$ and $\underline{g}$ is computed as local quotient of the cross-covariance k_{fg} and the product of the standard deviations σ_f and σ_g.

$$\rho_{fg} = \frac{k_{fg}}{\sigma_f \sigma_g} \tag{3.7}$$

The correlation coefficient expresses the similarity between variables by measuring their joint variability.

In contrast to the distance, which is a metric measure, the correlation coefficient is an angular measure. The higher the absolute correlation value, the smaller the related angle and vice versa. Uncorrelated observation vectors are orthogonal.

The correlation coefficient between two DTMs is useful for determining their feature similarity, but is futile for determining a measurement bias.

3.5.3   Assignment

Assignment concludes the association procedure. It determines, if the remaining measurements after the candidate selection and gating processes belong to the same entity. InSAR and stereo-optical measurements are finally related in this way. For this decision, the distance measures of the previous section are referred to. If these measures do not exceed a similarity boundary, they are transmitted to the final estimation. The boundary is established empirically, depending on the expected standard deviation of the measurements.

3.6 Estimation

At this point, a set of pairs of similar InSAR and stereo-optical measurements are available. The estimation process aims at combining the measurements to a best fitting observation according to the functional model, which depends on the application (Fig. 3.4). The following two estimation methods apply to this problem.
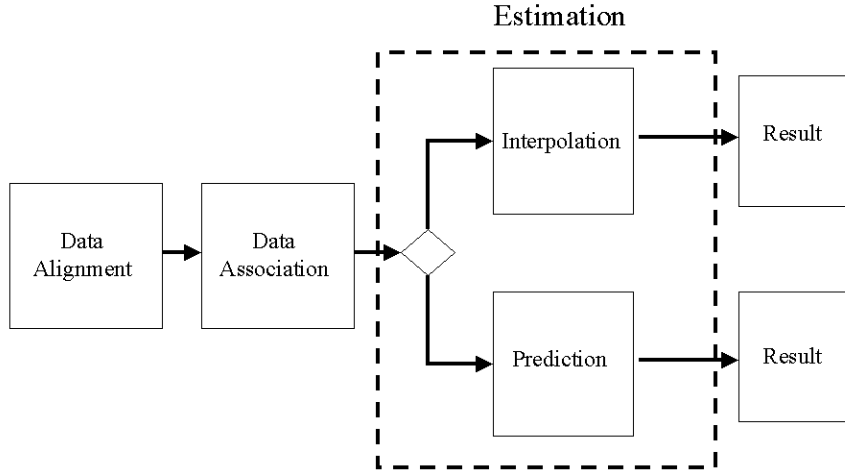
Fig. 3.4 Estimation. Depending on the mathematical model, two estimation options, interpolation and prediction, are applicable for the given fusion problem. The selection of the estimation option depends on the application. As indicated, the results of the options differ.

3.6.1 Interpolation

It is assumed that the real surface can be approximated, at least locally, by a linear function. The aim is to find the function parameters from a set of irregularly distributed observations. Once determined, the functional relationship is used to interpolate a regular grid.

In order to set up the mathematical model, InSAR and stereo-optically derived points are interpreted as discrete realizations of the linear function and are ordered in the local observation vector $\underline{g}$. Provided, the observations can be described as a linear combination of the vector of unknown function parameters, $\underline{f}$, and the given functional coefficients, expressed by the matrix $\mathbf{A}$, the following linear model can be formulated:

$$\underline{g} = \mathbf{A}\underline{f} \qquad\qquad (3.8)$$

The benefit of combining the relatively dense ERS InSAR measurements with existing points from SPOT is the increase in number of observations (i.e. elements of the vector $\underline{g}$). This increase in

redundancy is exploited in order to obtain a better estimate of the sought function parameters and in this way of the local topography.

Expressing the observation error vector with the vector $\underline{e}$, (3. 8) becomes

$$\underline{g} + \underline{e} = \mathbf{A}\underline{f} \tag{3. 9}$$

This leads to the well known least-squares formulation for the residual error $\underline{v}$

$$\underline{\hat{e}}^{\mathrm{T}}\,\underline{\hat{e}} = \underline{v}^{\mathrm{T}}\,\underline{v} = \mathrm{E}\{(\underline{f} - \underline{\hat{f}})^{\mathrm{T}}(\underline{f} - \underline{\hat{f}})\} \rightarrow \min \tag{3. 10}$$

which yields the best estimate of $\underline{f}$ *(Koch, 1980)* being

$$\underline{\hat{f}} = (\mathbf{A}^{\mathrm{T}}\mathbf{A})^{-1}\mathbf{A}^{\mathrm{T}}\underline{g} \tag{3. 11}$$

In the weighted form, with weight matrix $\mathbf{P}$, (3. 11) becomes

$$\underline{\hat{f}} = (\mathbf{A}^{\mathrm{T}}\mathbf{P}\mathbf{A})^{-1}\mathbf{A}^{\mathrm{T}}\mathbf{P}\underline{g} \tag{3. 12}$$

For the interpolation purpose, (3. 11) or (3. 12) are commonly used for deriving the parameters for a polynomial surface approximation, which is described in greater detail in section 5.3.1.

3.6.2   Prediction

A typical fusion problem is the prediction of an observation, based on set of measurements. The Kalman filter is a prediction problem solution widely used in time dependent systems *(Kalman, 1960)*. It will be shown in section 4.5 that prediction in the context of height measurement fusion is applicable for interferogram restoration.

The prediction model arises from (3. 9) through generalization of the error term

$$\underline{g} = \mathbf{B}\underline{f} + \mathbf{N}\underline{v} \tag{3. 13}$$

where $\mathbf{B}$ and $\mathbf{N}$ are known coefficient matrices and $\underline{v}$ is a vector of random parameters. The term $\mathbf{B}\underline{f}$ is interpreted as systematic part of the observation, while $\mathbf{N}\underline{v}$ is the random part. The model is

routinely applied for trend splitting in collocation (section 5.3.2), but is also the base for the Wiener image restoration, which is widely used in digital image processing *(Pratt, 1991).*

Wiener Estimation For a first simplification, one summarizes the second term into the random noise vector $\underline{n}$.

$$\underline{g} = \mathbf{B}\underline{f} + \underline{n} \tag{3.14}$$

The observation error is then

$$\underline{e} = \mathbf{B}\underline{f} + \underline{n} - \underline{g} \tag{3.15}$$

For the restoration of $\underline{g}$, an estimate of $\underline{f}$ is sought, which is formed by

$$\hat{\underline{f}} = \mathbf{W}\underline{g} + \underline{b} \tag{3.16}$$

where $\mathbf{W}$ is the restoration matrix and b is a bias vector. $\mathbf{W}$ and $\underline{b}$ are chosen for Wiener estimation in a way that they minimize the restoration error $\underline{e}$, which has been defined in (3.10).

Minimization of the least squares restoration error is achieved by applying the orthogonality principle, which yields two necessary and sufficient conditions for the determination of $\mathbf{W}$ and $\underline{b}$.

Firstly, the expectation values of the estimate and the image must be equal

$$E\{\underline{f}\} = E\{\hat{\underline{f}}\} \tag{3.17}$$

By substitution with (3.16), the bias $\underline{b}$ becomes

$$\underline{b} = E\{\underline{f}\} - \mathbf{W}E\{\underline{g}\} = E\{\underline{f}\} - \mathbf{W}\mathbf{B}E\{\underline{f}\} + \mathbf{W}E\{\underline{n}\} \tag{3.18}$$

Secondly, the restoration error must be orthogonal to the observation about its mean:

$$E\{(\underline{f} - E\{\hat{\underline{f}}\})\,(\underline{g} - E\{\underline{g}\})^{\mathrm{T}}\} = \mathbf{0} \tag{3.19}$$

By substitution:

$$E\{(\mathbf{W}\underline{g} + \underline{b} - \underline{f})(\underline{g} - E\{\underline{g}\})^{T}\} = \mathbf{0} \tag{3.20}$$

With (3. 18)

$$E\{(\mathbf{W}\underline{g} + E\{\underline{f}\} - \mathbf{W}E\{\underline{g}\} - \underline{f})(\underline{g} - E\{\underline{g}\})^{T}\} = \mathbf{0} \tag{3.21}$$

$$E\{(\mathbf{W}(\underline{g} - E\{\underline{g}\}) - (\underline{f} - E\{\underline{f}\}))(\underline{g} - E\{\underline{g}\})^{T}\} = \mathbf{0} \tag{3.22}$$

By further simplification:

$$\mathbf{W}E\{(\underline{g} - E\{\underline{g}\})(\underline{g} - E\{\underline{g}\})^{T}\} = E\{(\underline{f} - E\{\underline{f}\})(\underline{g} - E\{\underline{g}\})^{T}\} \tag{3.23}$$

Referring to (3. 5) and (3. 6), the term on the left side of (3. 23) denotes the auto-covariance $\mathbf{K_{gg}}$ of the observation g, weighted with $\mathbf{W}$, and the right side is the cross-covariance matrix $\mathbf{K_{fg}}$ between reference sample and observation. Thus $\mathbf{W}$ becomes

$$\mathbf{W} = \mathbf{K_{fg}}(\mathbf{K_{gg}})^{-1} \tag{3.24}$$

The previous equation is the solution of the Wiener-Hopf equation. What makes it important for interpolation applications, is the fact that one obtains the best estimate for $\underline{f}$ out of the auto-covariance of a set of observations and the cross-covariance, which is approximated with help of the established covariance function (section 5.3.2).

The covariance calculations can be avoided, if the systematic part $\mathbf{B}\underline{f}$ of (3. 13) can directly be approximated. By substitution of (3. 24) becomes

$$\mathbf{W} = \mathbf{K_{ff}}\mathbf{B^{T}}(\mathbf{B}\mathbf{K_{ff}}\mathbf{B^{T}} + \mathbf{K_{nn}})^{-1} \tag{3.25}$$

where $\mathbf{K_{nn}}$ denotes the noise covariance matrix. One obtains from (3. 25) a simplified expression by assuming the ideal measurements being uncorrelated and $\underline{n}$ being a white noise process, thus

$$\mathbf{W} = \mathbf{B^{T}}(\mathbf{B}\mathbf{B^{T}} + \frac{\sigma_{n}^{2}}{\sigma_{f}^{2}}\mathbf{I})^{-1} \tag{3.26}$$

The previous equation is further simplified to the expression of (3. 11) in case of absence of the additional noise.

62

The common problem with Wiener filtering is the determination of the matrix **B**. In image restoration applications, **B** is used to describe a systematic image degradation (e.g. blurring). It is approximated by comparing corrupted pixels with a set of independently derived uncorrupted points. This approach is as well applicable for fusing data from different sensors.

Estimation applications for both prediction and interpolation within the proposed concept for DTM fusion are given in the following two chapters.

3.7 Summary

The concept for fusing ERS InSAR with SPOT DTMs has been introduced in this chapter. The reason for fusing these data is the expected increase of quality (i.e. accuracy) of the point measurements. The concept takes advantage of the synergy of both measurement methods, which has been pointed out in chapter 2. Data synergy and its optimal exploitation are the decisive factors to achieve a high quality fused result. Following the common multi-sensor data fusion approach, the data sets are first aligned, then associated and finally fused by estimating the sought positional vector. During the alignment procedure, the coordinate and entity conversions are performed, depending on whether the data sets are fused during InSAR DTM generation or on the DTM product level. During association, the similarity of the observations is calculated and used for screening. As only similar measurements are passed to the estimation process, the reliability of the fusion result will be increased. In a final step, the sought entity (phase, height) is estimated from the grouped observations. Two estimation procedures, based on the least squares criterion, apply to the given problem: interpolation and prediction. Their functional models differ. The interpolation task is to estimate new points based on a mathematical description of the surface. The function parameters are calculated with a set of irregularly distributed observations and is therefore preferably used to fuse the stereo-optical and InSAR DTMs (chapter 5). Prediction performs estimation of newly acquired measurements on the basis of past observations. The functional model is capable to treat both systematic and random errors. Newer observations are treated with the derived model in order to minimize the measurement error. Prediction applies to the fusion problem during the InSAR DTM generation process, which will be addressed in the following chapter.

C h a p t e r   4

DTM INTEGRATION DURING INSAR PROCESSING

4.1 Introduction

The data fusion concept is applied for integrating an existing DTM in the InSAR generation process. In the stereo instance, DTM integration is routinely performed with the hierarchical approach in order to facilitate the matching. The low resolution DTM is introduced at the corresponding resolution level of the image pyramid. The InSAR case can be treated similarly. The DTM yields a prediction for optimizing corrupted interferometric phases and supports the crucial phase unwrapping process. The procedure takes into account that the SPOT measurements are of limited accuracy and is therefore applicable in realistic DTM fusion scenarios.

The structure of this chapter follows the proposed data fusion concept. The following section deals with data alignment and association, starting with the DTM slant range conversion and the different association options, which depend on the fusion issue. Removal of atmospheric artifacts, phase slope estimation for phase unwrapping and ground range conversion of the interferometric measurements are addressed with the estimation. In order to avoid an error leakage from the stereo measurements into InSAR measurement process, the intervention is kept as low as possible.

4.2 Alignment

The standard slant range conversion scheme is given in section 3.4. The DTM coordinate conversion into the SAR orbital (X, Y, Z) coordinate system is a standard geodetic procedure and is not discussed here any further.

The Doppler times t_{1p} and t_{2p}, belonging to each orbital pass, are determined by iteration along the orbit model as long as a point satisfies the Doppler condition (2. 30). In this way, the positions S_i and the corresponding orbit times t_{ip} are determined. The Doppler times provide simultaneously the synthetic image azimuth coordinate a_i. With the SAR orbit model, the ranges R_{1p} and R_{2p} for each DTM point $\underline{P}$ with coordinates (X_p, Y_p, Z_p) are calculated with (2. 29). The corresponding simulated phase $\phi_{sim, abs}$ is finally calculated with (2. 12).

The relationship between the DTM and the interferometric image coordinates is used for baseline correction using ground control points. With the procedure mentioned above, each point delivers three equations for adjustment of the orbital position vector. If they are not compensated, orbital errors lead to a misalignment between simulation and actual phases and must be prevented from entering the fusion process.

4.3 Association

After slant range conversion, there are two options for the design of the data association procedure, mostly depending on the accuracy of the simulation. Firstly, for similarity calculation, the distance between simulation and interferogram is directly computed. This is also denoted as DTM flattening. Secondly, the simulation serves in regions of low coherence for the interferometric phase slope estimation.

4.3.1   Distance calculation

Flattening If DTM information is available, it is typically used after alignment in order to flatten the interferogram. The simulated unwrapped phases are subtracted from the interferogram. The difference is subsequently wrapped in the $[-\pi, \pi]$ interval, resulting in the flattened interferogram $\phi_d(r,a)$.

$$\phi_d(r,a) = \mathrm{mod}(\phi(r,a) - \phi_{sim,abs}(r,a), 2\pi)\big|_{-\pi}^{\pi} \tag{4. 1}$$

If the DTM is of sufficient resolution and accuracy, the resulting flattened interferogram consists of a single fringe with phase values presenting the similarity between actual interferometric measurements and the simulation. It is practical for the subsequent association to use the ambiguity height, i.e. to use the 2π distance for similarity declaration. If residual fringes emerge during this operation, they are interpreted as errors larger than the ambiguity height and are easily excluded. In

66

this way, the no phase unwrapping needs to be performed, as all phase values belong to the same fringe.

Despite its widely use, DTM flattening has four major shortcomings:

1. Flattening needs a DTM of the same resolution as the interferogram to remove all fringe lines.

2. The simulation from the DTM has to be significantly more accurate than the actual interferogram in order to justify the error declaration of the residual fringes.

3. DTM errors beneath the ambiguity height are not detected and leak in this way easily into the InSAR DTM generation process.

4. Flattening interferes maximally with the InSAR measurement process.

Simulations of lower resolution are still applicable, if a multi-resolution approach is used. *Massonnet et al. (1996)* proposed the use of DTMs generated from digitized 1:1'000'000 or 1:500'000 maps, in order to reduce the topographic fringe contribution in repeat pass interferometry. Resolution and accuracy of those DTMs do not suffice for the intended high quality DTM generation.

The limitations of use in respect to insufficient accuracy of the existing DTM are mitigated, if only the trend instead of actual phase difference is evaluated. The option is therefore not to aim at the principal component, but at full cycles, displaying systematic error effects like incorrect baseline determination or atmospheric artifacts. As shown in section 2.2.10, their effect on short baseline measurements may easily exceed a full phase cycle. This procedure also avoids too much interference with the InSAR generation process.

In many cases, simulations from SPOT DTMs of normal quality are not applicable for phase flattening, especially for long baseline measurements, having a small ambiguity height. Still, there are two options for associating them with the InSAR phases, exploiting their resolution. Either, by examining the 2π constant, which is added during the unwrapping process, or by using the simulated principal phase values to help overcoming unwrapping problems in low coherent regions. The shorter the baseline, the less critical is the first option, which aims at systematic effects. The second option is justified, as long as it is applied only locally. It aims at the local phase restoration low coherent regions, which trouble the phase unwrapping.

4.4 Atmospheric Artifacts

Model Atmospheric artifacts must be compensated before the phase unwrapping procedure. As mentioned in section 2.2.10, atmospheric changes may cause an additional phase contribution. Depending on the spatial extent of the changes, the phases are either corrupted locally or systematically, in case that residual fringes emerge. These corrupt the phase unwrapping procedure by adding an erroneous multiple of 2π, which causes a significant systematic error, especially with shorter baselines. Up to now, atmospheric effects can only be detected and localized by employing independent measurements. Basically, the difference to the reference data is computed with (4. 1) and measurements exceeding the expected difference are excluded from the measurement process.

The option of a baseline error is excluded for the further considerations (section 2.2.10 and 2.6). If the atmospheric contribution to the phase measurement is systematic, the resulting erroneous surface can be approximated and removed with help of the existing measurements. For that purpose, a simple noise model for the interferogram phase $\phi(r,a)$ is introduced

$$\phi(r,a) = \phi_{if}(r,a) + \Delta\phi_n(r,a) + \Delta\phi_{atm}(r,a) \tag{4. 2}$$

with $\phi_{if}(r,a)$ being the uncorrupted measurement, $\Delta\phi_n(r,a)$ the noise and $\Delta\phi_{atm}(r,a)$ the atmospheric phase contribution. For a SNR $\gg 1$, the atmospheric contribution governs the phase error, as it does not affect the coherence.

Detection If a simulation $\phi_{sim}(r,a)$ with an error $\Delta\phi_{n,sim}(r,a)$ is applied, the flattened interferogram $\phi_d(r,a)$ becomes with (4. 1) and (4. 2)

$$\phi_d(r,a) = \Delta\phi_n(r,a) + \Delta\phi_{n,sim}(r,a) + \Delta\phi_{atm}(r,a) \tag{4. 3}$$

By computing the error statistics in different highly coherent regions ($\Delta\phi_n \approx 0$), the noise characteristics of $\phi_d(r,a)$ can be determined in respect to $\Delta\phi_{atm}$ and $\Delta\phi_{n,sim}$. Generally, certain knowledge of the DTM error is available to approximate this contribution.

Assuming the atmospheric contribution to be locally dependent, affected regions are revealed by their statistical deviation (Fig. 4.1), when the topographic fringes have been removed. With standard SPOT accuracy, one single fringe should remain after DTM flattening. Larger deviations may occur due to low coherence or, according to (4. 3), atmospheric artifacts. Otherwise, a locally independent atmospheric contribution, i.e. the whole scene is uniformly affected, causes an increase

of the mean difference. In order to increase the 'contrast' between noise and atmospheric artifacts, short baselines are preferred again, as the effect is more pronounced here ((2.34), (2.37)).
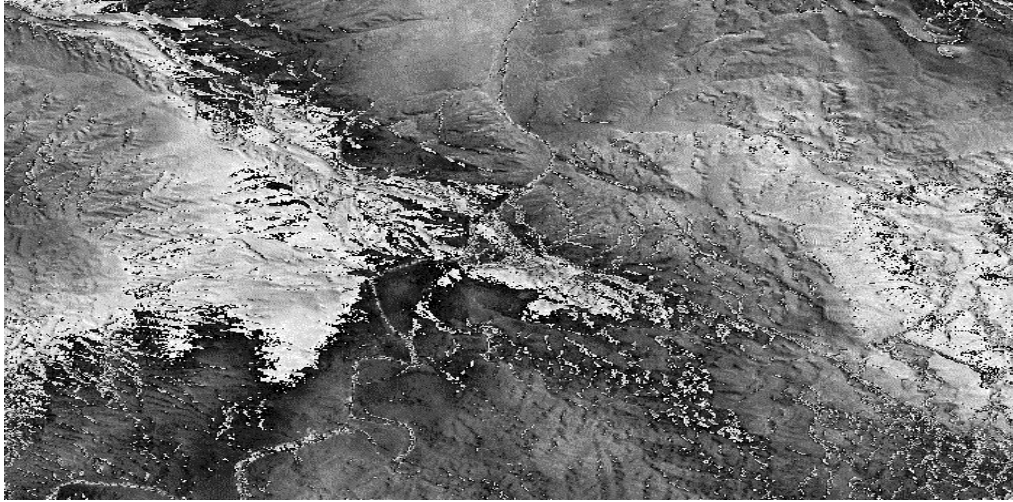

Fig. 4.1 Detection of atmospheric artifacts at test site Spain II (Fig. 2.6c, Fig. B3) by flattening the interferogram with the SPOT DTM. The artifact extends over half the scene, adding an erroneous surface. Due to the relatively short InSAR baseline, the phase contribution due to the artifact exceeds a full phase cycle, (~60m) and can easily be detected.

Removal The flattening result represents the wrapped difference surface relative to the SPOT data set. A continuous form of this surface is derived by unwrapping this flattened interferogram (which is easily done as very few fringes are left!). The error surface induced from atmospheric changes can now be estimated by fitting a surface polynomial through the phase differences:

$$\hat{\phi}_d(r,a) = \hat{\phi}_d(r,a;c_i)$$

(4. 4)

where r, a are the range and azimuth image coordinates and c_i are polynomial coefficients. Under the condition that the error budget of phase values of high coherence is dominated by the atmospheric error, only highly coherent phases will be used for surface fitting. It has been shown that the atmospheric effects have a low frequency nature *(Ferretti et al., 1999)*. Therefore, the slowly changing erroneous surface is modeled with a second to third order polynomial approximation. The resulting surface finally compensates the artifacts by subtraction from the interferogram (Fig. 4.2).

The advantage of such a procedure is certainly that it removes the residual fringes originating from the atmospheric changes. These deformations do not corrupt the DTM generation process any further. The required SPOT DTM accuracy for that procedure behaves inversely to the baseline length and is achieved with common data sets.
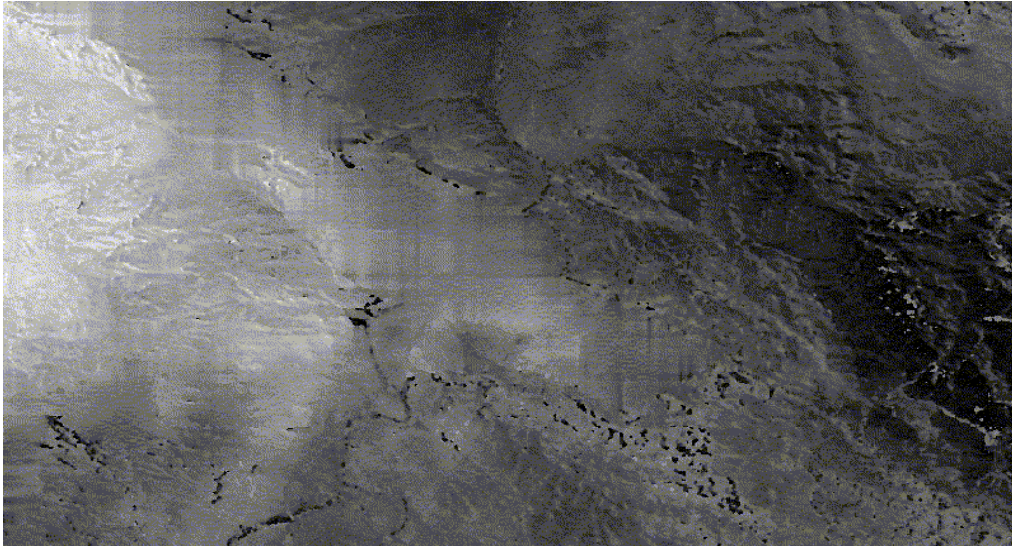
Fig. 4.2a The erroneous surface after phase unwrapping of Fig. 4.1. Phase unwrapping for derivation of a continuous surface is necessary for the polynomial approximation.

Fig. 4.2b The polynomial interferogram approximation for compensating the atmospheric surface. A third order polynomial has been fitted through a set of highly coherent unwrapped phases of (a).

Fig. 4.2c The DTM flattened interferogram after compensation of the residual atmospheric fringe. The phase difference does not exceed 2π in most parts of the site. Remaining disturbances in the mountains originated from layover and/or decorrelation.

4.5 Wiener-Based Phase Unwrapping

Common approaches of noise reduction include multi-look image processing, averaging or interferogram filtering. All these techniques have in common that they are hardly noise adaptive, thus affecting also valid measurements while dealing with the noise. The phase reconstruction in regions of low coherence is generally not possible with these methods. In *(Honikel, 2000),* a method is proposed, which aims at a restoration process, which not only removes or reduces the noise, but also restores those regions, where the phase measurement previously failed.

4.5.1   Interferometric Image Model

The following considerations relate to the general degeneration and restoration model, given in section 3.6.2, in which the image vector $\underline{f}$ is subject to some unspecified type of degradation, which affects the image both spatially (multiplicatively) and pointwise (additively), resulting in an observation g (Fig. 4.3).
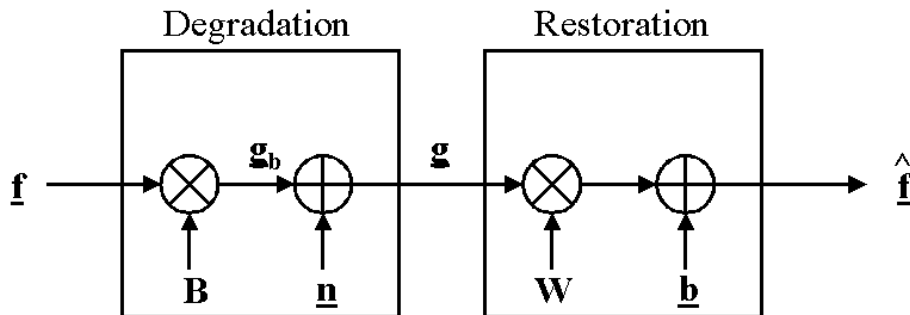
Fig. 4.3 The interferogram degradation scheme and its restoration with the Wiener estimation. The ideal phase measurements $\underline{f}$ are blurred, resulting in $\underline{g}_b$, and subsequently superimposed by noise. The restoration deconvolves the blurring and removes the bias.

Interferograms are in a narrow sense not images, but a measure for the microwave travel path difference modulo 2π. However, the interferogram is furthermore treated as single channel imagery, being degraded from different decorrelation sources (section 2.2.6).

With respect to the interferometric phase course, the degeneration causes either a local blurring of the fringe lines or adds randomly to the local noise.

Blur Interferogram blurring originates from the spectral shift of the ground reflectivity spectra belonging to the different acquisitions. This shift is induced by the slightly viewing angle difference

$\Delta\theta$, which causes the spectral components of the range spectrum of the same resolution cell to be shifted by Δf (section 2.2.6). The spectral shift causes an 'unfocussed' measurement. The similarity to the blur in optical images is obvious. Although spectral shift filtering is a common approach in interferometric processing in order to reduce the decorrelation, local phase blur inevitably remains after the filtering.

Referring to Fig. 4.3, the blur is modeled by

$$\underline{g}_b = \mathbf{B}\underline{f} \tag{4.5}$$

where $\mathbf{g}_b$ is the blurred interferometric phase observation vector and $\mathbf{B}$ is a matrix, whose elements are points on the measurement system impulse response function, often denoted as point spread function.

Especially the blurring of the fringe borders endangers the correct phase unwrapping, as the border between the phase cycles is not determinable, resulting possibly in coarse unwrapping errors (Fig. 4.4).

Noise Another aspect of decorrelation is the increase of the statistical phase variation. The characteristic of this degradation is regarded as being additive.

The reduction of the phase noise is crucial for the correct determination of the multiple 2π, which has to be added to each phase value during the unwrapping process. In presence of noise, phase jumps (residuals) can occur, which spoil the implicit unwrapping assumption of a smooth terrain, with phase changes not higher than π between two adjacent values (Fig. 4.4). The unwrapping is bound to fail, if these measurements are not excluded from the procedure.

Common automated phase unwrapping techniques (e.g. the branch cut algorithm) are able to deal with this problem only to certain extend. Large regions of low signal to noise ratio still lead either to failure of the DTM generation process, or, worse, add a global error also to uncorrupted phase measurements, if unwrapped erroneously.

Mathematically, this corruption is described in the vector-space model with (3.14). The noise $\underline{n}$ is in a first approximation assumed to be zero mean with auto-covariance matrix $\mathbf{K}_{nn}$. The Wiener estimator yields the best estimate for this type of corruption.

As follows from (2. 14), all types of decorrelation are indicated by low coherence, regardless to the their individual source. The relation between decorrelation and SNR is given by (2. 21). It is therefore very practical that the Wiener restoration process is steered by the SNR.
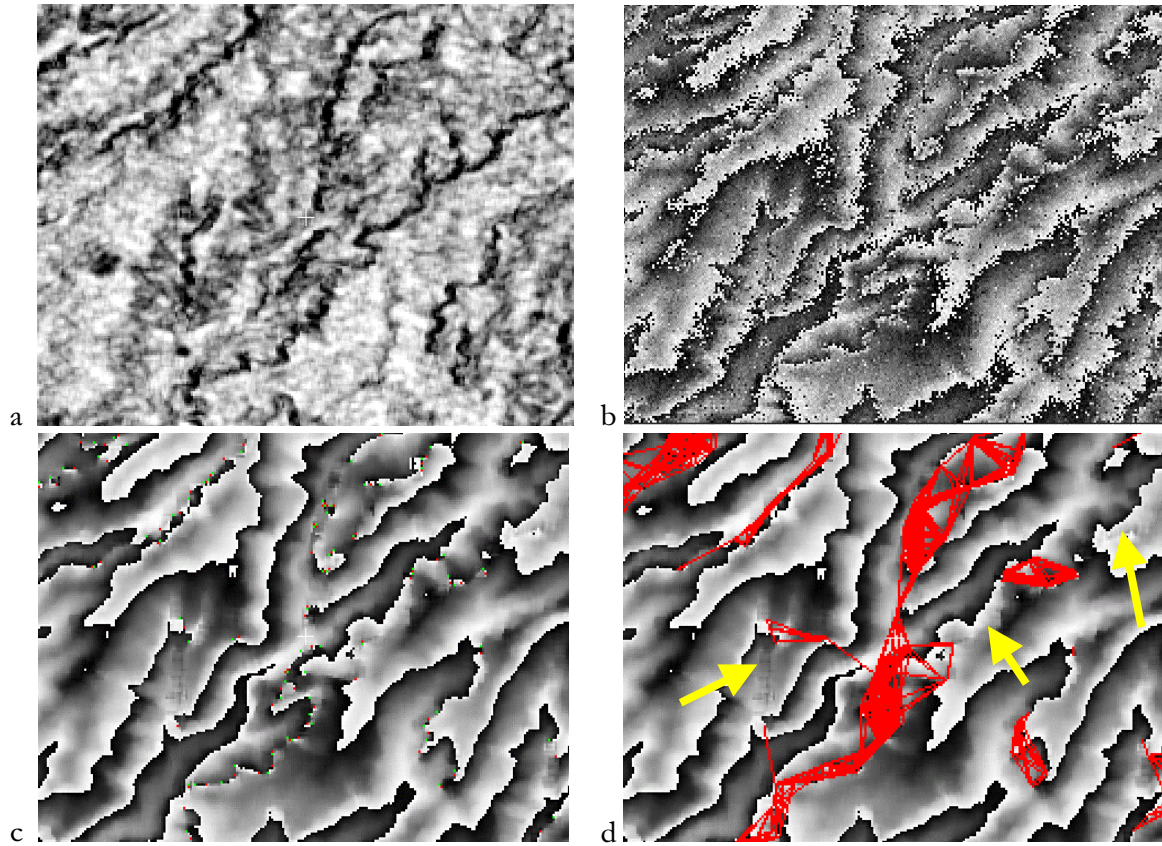
Fig. 4.4 Low coherence (a) indicates the corrupted interferogram locations (b). Interferogram filtering reduces the additive noise component, but intensifies the fringe line corruption (c). Remaining residuals have to be connected to clusters before the phase unwrapping. As clusters (d) must not be accessed, unwrapping holes remain, while increasing distance between the residuals leads to erroneous placed cuts (marked), causing unwrapping errors.

4.5.2   Blurring and Noise Estimation

Although Wiener filtering is theoretically the optimal method for the phase deconvolution in presence of noise, several problems limit its effectiveness.

Firstly, the precise knowledge of the ideal measurement vector $\underline{f}$ and the noise term $\underline{n}$ cannot be assumed for most applications including this one. Models, developed in digital image processing for the direct approximation of **B**, are too weak for the highly complex phase restoration task. Secondly, the assumption of spatially invariant degradations for the whole image is not valid for the spatial variant interferometric signature. Thirdly, the image and noise signals are assumed to be stationary, which will hardly hold valid in varying terrain.

Spatial Invariance and Stationarity In order to overcome limitations two and three, the proposed Wiener filtering will be applied locally, depending on the local signal to noise ratio. The degradations behave almost spatially invariant within the borders of a limited window. In addition, the local covariance will hardly change within the window in contrast to the whole interferogram, thus matching the stationarity requirement for the Wiener filtering.

Blurring For overcoming limitation one, the uncorrupted vector $\underline{f}$ will be approximated locally in this approach with simulations from the stereo-optical DTM. It serves for the calculation of the cross-covariance matrix (3. 24) in those areas, where the interferometric phases are degraded. The simulated data will deliver here information, which approximates the correct local phase slope and serve for the determination of $\mathbf{W}$ and $\underline{b}$.

Following the formulation of (3. 26), $\mathbf{B}$ becomes:

$$\mathbf{B} = \underline{f}\,\underline{g}_b^{-1} \tag{4. 6}$$

The noise reduced image $\underline{g}_b$ (Fig. 4.3) is derived by the common interferogram filtering operations. The Wiener filtering is designed to improve these results further.

Signal to Noise Ratio As the signal to noise ratio steers the filter, the correct determination of the SNR is inevitable for the successful phase restoration. In the InSAR case, determination of the SNR becomes a straightforward task, as this information is directly retrievable from the interferometric processing by computing the local coherence γ from the SAR images (2. 21). The SNR is a useful hint for interferogram segmentation and association. In order to keep intervention during processing low, only regions where the local coherence is low are treated with the filter.

4.5.3   Discussion of the Wiener Estimator

Certain aspects of the filter adaptation to the presence of noise can directly be derived from (3. 18), (3. 24) and (3. 26).

In case that the image signal to noise ratio reaches infinity, i.e. no noise corrupt the fringes, the Wiener filter behaves equivalent to an inverse deconvolution filter with

$$\mathbf{W} = \mathbf{B^{-1}} \tag{4. 7}$$

On the other hand, if the ratio approaches zero, $\mathbf{W}$ is $\mathbf{0}$. The bias becomes (3. 18)

$$\underline{b} = E\{\underline{f}\} \tag{4. 8}$$

forcing a smooth solution in presence of extreme noise.

Finally, if the image signals are not blurred, thus $\mathbf{B} = \mathbf{I}$, $\mathbf{W}$ becomes

$$\mathbf{W} = \mathbf{I}(\mathbf{I} + \frac{\sigma_n^2}{\sigma_f^2}\mathbf{I})^{-1} \tag{4. 9}$$

indicating the low pass properties of the filtering in the special case of pure additive phase noise.

It is important to note that the purpose of the Wiener estimator is to recover the unknown phase slope from the noise and *not* to locate the slope, derived from the simulation, which would be the case for a matched detector. Although the simulated interferogram is used for restoration, the Wiener result is mostly dependent on the interferometric signal (3. 24). This guarantees maximum independence from the given heights and minimizes their impact on the InSAR generation process.

4.5.4   Phase Unwrapping

The branch cut algorithm circumvents the error sensitivity of the integration by detection and connection of phase residues with ghostlines, which must not be crossed during the phase unwrapping. The algorithm tackles cases with limited amount of residues and short lengths of the cuts. Automatic branch cut connection fails in regions of high residue density. This regions require in part cumbersome manual intervention for ghostline connection. With rising corruption, certain regions may not be recovered even manually and have to be left out for further processing. The unwrapped result falls apart in several isolated regions.

The simulation enables automated unwrapping, while preserving the strength of direct integration. In critical areas, the phase slope is estimated with the Wiener estimator. As shown above, critical areas are characterized by their low signal to noise ratio, which is indicated by a low coherence value. The database yields the continuous phase course, hence an approximation of the unwrapping solution. The simulation is therefore used for phase estimation and unwrapping constraint - in analogy to the constraint used for matching in the stereo-optical case.

In order to minimize the mean square error between the correct unwrapped phase value $\phi_{unw}(r,a)$ and its estimate, (3. 10) is written as

$$e(r,a) = E\{(\phi_{un}(r,a) - \hat{\phi}_{un}(r,a))^2\} \rightarrow \min \tag{4. 10}$$

or as sum of the principal phase components with the integer 2π multiples n,

$$e(r,a) = E\{((n2\pi + \phi(r,a)) - (\hat{n}2\pi + \hat{\phi}(r,a)))^2\} \tag{4. 11}$$

$$e(r,a) = E\{(2\pi(n - \hat{n}) - (\phi(r,a) - \hat{\phi}(r,a)))^2\} \tag{4. 12}$$

In order to minimize the error, both terms on the right hand side have to be minimized. When the second term is minimized by the Wiener restoration, as shown in section 3.6.2, the phase unwrapping behaves uncritical due to optimized signal to noise ratio. Therefore, the best estimate of n is derived as indicated in section 2.2.7 by the branch cut algorithm after the Wiener estimation, resulting in a minimized error of the whole term.

The great advantage of the Wiener based method is its adaptation to the local noise. The filter may be designed in a way that it does not interfere with the unwrapping algorithm in high coherent areas, guaranteeing minimal interference of the existing DTM with the interferometric measurement process.

Areas, lacking reliable phase information are detected and marked during the data association step. In contrast to the common branch-cut approach, the Wiener supported unwrapping algorithm may now enter the forbidden zones (Fig. 4.5, 4.6). By estimating of the phase slope from the simulation and the measured interferometric phases, unwrapping is carried out automatically in low coherent regions in the interferogram.

Algorithm The algorithm is designed to incorporate the consistency checking of the 2π constant, which has been stated in section 4.3. The phases are unwrapped by direct integration. The unwrapping result is steadily compared with the unwrapped simulation in low coherent areas (Fig. 4.5). The unwrapped result must not exceed the association distance ε (Fig. 4.5), which is selectable according to the accuracy of the DTM and the baseline length. If the actual unwrapped phase exceeds the constraint, the correct value of n is calculated with help of the expected value derived from the simulation and substitutes the corrupted one. The derived continuous result unbiased in respect to the simulation, but still blurred. It is therefore filtered according to (4. 7) in order to remove that blur.

The integer constraint favors certainly shorter baselines with large ambiguity heights, requiring only moderate accuracy from the existing database. An association distance of $\pm\pi$ equals a height difference of ±30m with a baseline length of 150m with ERS. This comparison is rather uncritical, as common SPOT DTMs match this accuracy requirement. The constraint allows direct phase unwrapping without any preprocessing and saves the work for the branch cut placing.
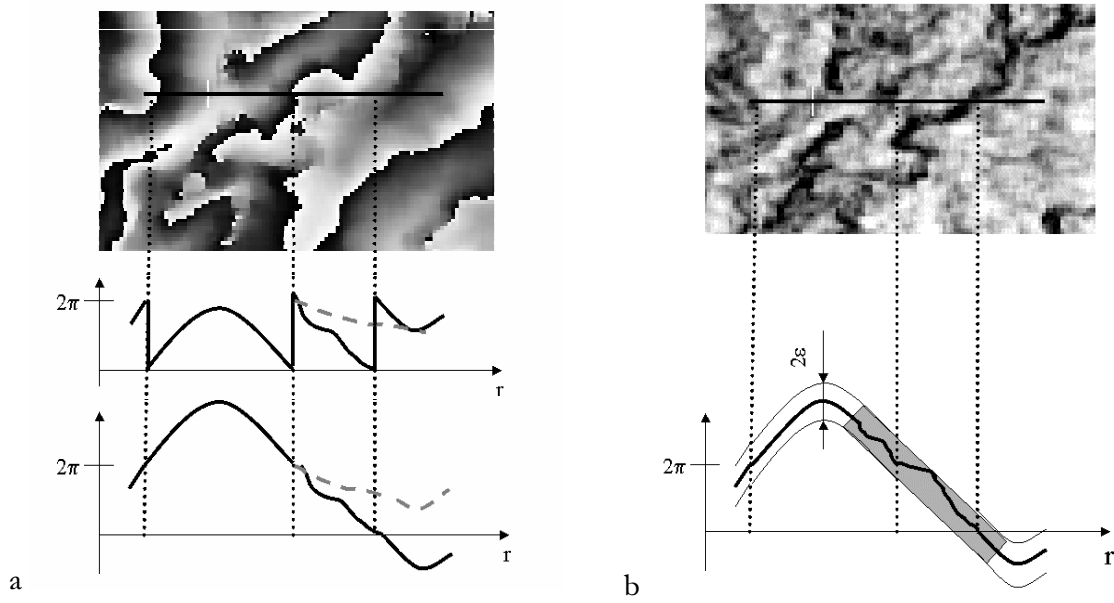
Fig. 4.5 Illustration of the Wiener phase unwrapping. The 'ideal' phase course and the actual interferometric measurement (grey) are given along a range line (a). The disappearance of the fringe border causes an unwrapping error of 2π. With the Wiener filtering (b), the phase slope is estimated in the low coherent areas with help of the simulation, which also sets up an unwrapping constraint of $\pm\varepsilon$. The unwrapping results must not exceed this constraint. In this way, the procedure bridges decorrelated areas and achieves a complete unwrapping result.

Multiscale and Iterative Algorithms The presented method is easily extended to an iterative procedure, which is able to handle phase simulations having lower resolution. The simulations are introduced on top of the image pyramid, where the solution is derived in the described way. In a iterative way, the solution is then used to constrain the unwrapping of the next level. The grid requirement from the DTM depends on the terrain. Grids up to 100m are reasonable for this purpose.

The Wiener estimation itself can be implemented iteratively. In order to further reduce the influence of the SPOT measurements on the InSAR phases, the filtered continuous result after the first iteration is used instead of the simulations for a second iteration of the described procedure. For further iterations, ε is continuously reduced. The estimation is terminated when the

convergence criterion, defined during the association, is met. In this way, the real phase slope is reconstructed with minimal interference of the SPOT measurements. In Fig. 4.6, the SPOT simulation and Wiener result of Fig. 4.4 are given. The original fringe shape (Fig. 4.4) is preserved.

a   b
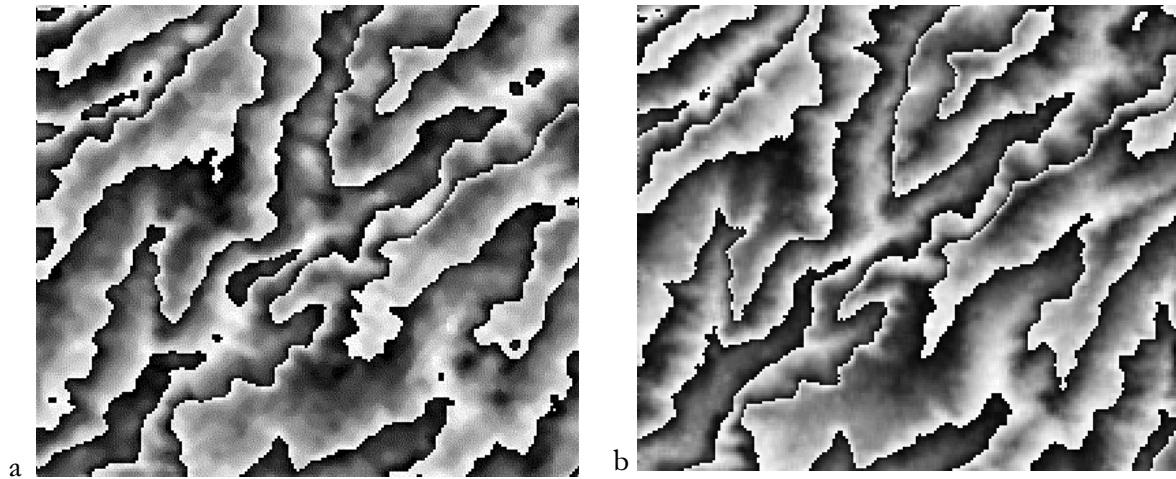
Fig. 4.6 Simulation and unwrapping result (see Fig. 4.4). In order to preserve the original interferometric phase, the slope is locally estimated with help of the simulation (a), which is obviously of different shape. Due to the estimation, the result (wrapped) (b) resembles much the original interferogram (Fig. 4.4b), but with reduced noise and reconstructed fringe borders.

4.6 Geometric Conversion

After the phase unwrapping procedure, the measured phases are converted to heights and geocoded into a map projection system, as outlined in section 2.2.9. As control point matching is very cumbersome with SAR (Fig. 4.7), the benefit of introducing an existent DTM into these processing steps is the adjustment of the possibly erroneous orbit model on which both steps rely. This can either be performed with some selected control points for adjustment of (2. 4) with (2. 29), (2. 30) and (2. 31), or by employing the DTM for removing any systematic effect.
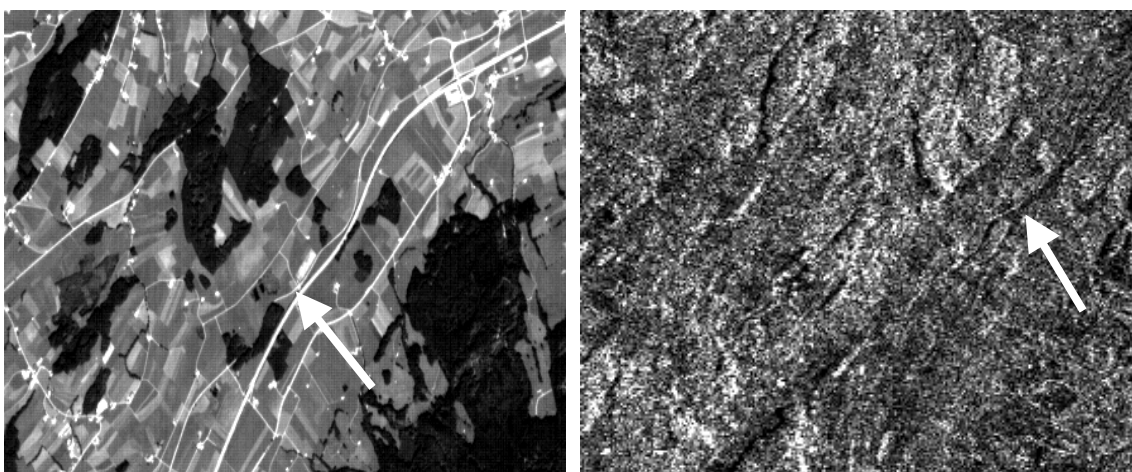
Fig. 4.7 Ground control point matching in SPOT (left) and ERS (right) images. The arrows mark the same point in both images. The feature is hardly found in the ERS image.

4.6.1 Phase to Height Conversion

As a variation of the polynomial method proposed in *(Geudtner and Schwäbisch, 1996)*, one calculates a look-up table for the phase-height correspondence from the slant range converted SPOT DTM and the unwrapped interferometric phases. Assumed that the phase-height relation is approximated within an estimator window by

$$h(r,a) = \sum_{i=0}^{n-1} c_i \phi_{un}^i(r,a) \tag{4.13}$$

with c_i being the coefficients of a polynomial of degree n-1, it is possible to derive the relation throughout the whole interferogram, given enough associated measurements. The relationship is sufficiently modeled with a 2nd to 3rd order polynomial, depending on the spacing of the existing measurements.

As the orbits slowly converge in repeat pass interferometry, the relation has to be determined along and across the whole interferogram. A solution for c_i can be derived from a coarse grid and expanded through interpolation to each interferogram pixel, as the change rate of the phase-height relation is low. This allows also existing coarser DTMs to interact with the phase height conversion.

4.6.2 Geocoding

The method for converting the slant range into map coordinates has been described in section 2.2.9. By its nature, geocoding is the alignment process for the DTM fusion, during which the image coordinates are transformed into map geometry. The generated DTM can as well be used for the geocoding of thematic SAR information like coherence or backscatter amplitude images. The SAR geocoding procedure with a given DTM is described in *(Curlander, 1982)*. Geocoded SAR images offer the opportunity to validate the planimetric accuracy by comparing the results of the stand-alone method with those of the geocoding using the SPOT DTM, or directly by comparing them with a backscatter simulation from the SPOT DTM *(Guindon and Adair, 1992)*. In this way, the planimetric error induced from an erroneous orbit model (section 2.2.10), resulting in a planimetric error, is detected and compensated.

4.6.3 Correction of Baseline Errors in the InSAR DTM

While the planimetric error derived by erroneous baseline determination may be compensated with registration to existing data, the altimetric error requires extra treatment. It has been shown in

section 2.2.10 that a baseline attitude error translates a tilt in the InSAR DTM. The effect can be modeled as a plane, superimposed to the actual surface H(N,E), causing the surface to tilt in respect to the datum. Mathematically, the additional plane is modeled with a first order polynomial P(N,E)

$$P(N,E) = c_0 + c_1 N + c_2 E \qquad (4.14)$$

where N, E are the DTM coordinates and c_i are polynomial coefficients. The InSAR DTM heights H_{SAR}(N,E) can then be described as

$$H_{SAR}(N,E) = H(N,E) + P(N,E) \qquad (4.15)$$

The SPOT database H_{opt}(N,E) can be used for approximation of H(N,E) in and solving for P(N,E) by computing the difference ΔH(N,E) between the InSAR DTM and the database.

$$\Delta H(N,E) = \hat{P}(N,E) = H_{SAR}(N,E) - H_{opt}(N,E) \qquad (4.16)$$

In a final step the first order polynomial for approximation of P(N,E) is fitted through ΔH(N, E) and removed from the InSAR measurements (Fig. 4.8).

-3m   10m

Fig. 4.8 Tilted plane. The systematic height trend has been assessed with a first order approximation through the differences of the ERS and SPOT DTM at the Swiss test site. The systematic error was induced by an erroneously determined baseline.

In practice, the approach is neither demanding for the SPOT DTM in respect to accuracy or to resolution. It serves only for detection of the trend, which is finally approximated by a polynomial through the ensemble of differences (Fig. 4.8). The accuracy of the individual point is of minor importance. A grid size of 100m easily suffices for ERS DTMs.

Baseline tilt compensation is an option in cases, where the accuracy limitations of state vectors can not be overcome with ground control points of sufficient quality. It should be favorably carried out after ground range conversion in order to have equally distributed posts for fitting.

4.7 Summary

In this chapter, different options for the integration of a SPOT DTM in the InSAR DTM processing have been discussed. Depending on the DTM resolution and accuracy, different approaches can be followed. Coarser DTMs are applicable for detecting and removing systematic effects on the InSAR measurements, such as residual fringes, originating from atmospheric changes, and the effects of an erroneous orbital model. Once observed, these effects can be approximated and compensated by using low order approximations, fitted through the difference between InSAR and the DTM measurements. A coarser DTM can also be used in order to constrain the phase unwrapping process, thus preventing it from failure in problematic regions. The constrained unwrapping is completely automatic and does not require any preprocessing (e.g. cut placing for residue connection) and can be realized as a multigrid approach.

Common interferogram filtering operations are hardly noise adaptive and do not deal correctly with spatial decorrelation, as only additive noise is assumed. An interferometric phase model has been proposed, which covers both additive and multiplicative phase corruption. If the SPOT DTM is of higher resolution, it may serve as a first approximation for calculating the parameters of the Wiener filter, which deals best with the presented image model. Wiener filtering is noise adaptive, deals with both, additive and multiplicative effects, and is in the implemented form (i.e. using the DTM as constraint) also able to restore degraded fringe borders. With an iterative filtering approach, the SPOT DTM is only used for first iteration, preventing it from interfering too much with the InSAR DTM generation process.

Although the effect of phase errors behaves inversely to the baseline length, short baseline InSAR measurements are preferred for all mentioned fusion operations, because of their moderate requirements in respect to the DTM quality. In addition, the coherence with short baselines is

higher and steeper terrain is better resolved, both leading to an increase in measurements. Due to the large ambiguity height, possible errors are easier to detect and to be removed with the SPOT DTM. If still needed, a long baseline interferogram, possibly from an opposite pass, can additionally be processed after the fusion of the short baseline measurements with the DTM.

C h a p t e r   5

FUSION OF INSAR AND STEREO-OPTICAL DTMS

5.1 Introduction

The options of fusing InSAR with already existing stereo-optical height measurements are discussed in this chapter. Depending on the quality of the existing data, different strategies are pursued by identifying and taking advantage of the synergy between the DTM sources. Inevitable for all approaches is the association and alignment process as described in section 5.2. After the similarity grouping, the fusion options are addressed in sections 5.3 and 5.4:

1. Accuracy improvement by interpolation. If the gridsize of the SPOT and ERS DTMs is similar, this approach seeks to generate a fused DTM of improved accuracy by interpolating support points, which are derived through the association process.

2. Densification of an existing coarser grid. A solution, if it is intended to fuse the InSAR measurements with coarse DTM. A terrain trend is derived from the coarse grid and refined with the denser InSAR measurements.

3. Frequency domain fusion. The options mentioned before are realized in the frequency domain by complementary exchange of uncorrupted frequency components in order to reduce the individual erroneous measurements.

5.2 Data Alignment and Association

5.2.1   Alignment

The basic alignment steps have been described in section 3.4. Coordinate and entity transform relate in this scenario to the coordinate transform of the InSAR height measurements into the projection of the existing DTM. As we have seen in chapter 2, InSAR measures elevation relative to the local reference ellipsoid. Hence, the result after phase to height conversion is in geographic coordinates, which have to be transformed to orthogonal Cartesian coordinates by standard geodetic transforms. If the existing DTM has not been used for the georeferencing of the InSAR measurements, the DTMs have to be registered to each other as described in section 4.6 in order to prevent any systematic error from entering the fusion process.

5.2.2   Association

The basic association procedure has been described in section 3.5. After alignment the closeness between the points in the grids is determined in order to discriminate between similar and non-similar measurements. The basic distance measures, spatial distance and correlation coefficient decide, which point pairs are allowed to enter the fusion process. If the measurements are in the same grid, the spatial distance reduces to the height difference ΔH between both measurements.

Weights In order to describe the quality of measurements participating in the fusion process, additional weights are definable. For InSAR, the coherence value approximates the local random error (section 2.2.10). Provided that the atmospheric contribution to the local noise has been eliminated with the existing DTM (section 4.4), the geocoded coherence information is a very suitable InSAR measurement quality indicator. It is tempting to introduce the cross correlation coefficient of the matching procedure as corresponding quality indicator of the optical measurements. However, in contrast to coherence, cross correlation is not a quantitative error measure. It indicates the similarity of the image patches used for the matching. Mis-matches still occur despite high correlation and vice versa. On the other hand, with the similarity measured before, mis-matches are detectable allowing to apply the correlation coefficient as qualitative measure.

5.2.3   Gating

The straightforward gating criterion is a rectangular gate, which distinguishes if two measurements are similar or not by testing their spatial distance. In case that only height difference ΔH is examined, gating becomes a thresholding operation. The threshold value should reflect the

expected DTM error of each scene. It is therefore chosen in the range of the expected root mean square error of the measurements. A threshold value of 10 - 15m is selected in normal cases, with higher values in more problematic terrain. The problem of losing measurements by rejecting both InSAR and stereo-optical measurements is mitigated by employing individual weights (e.g. coherence), allowing highly confident stand alone measurements to enter the fusion process.

5.3 Fusion in the Spatial Domain

5.3.1 Polynomial Surface Approximation

The task of the fusion process is to generate a single DTM out of the associated measurements originating from both sources. The common engineering problem of having redundant observations of limited accuracy is commonly solved by using the least squares adjustment.

The basic polynomial surface interpolation approach can be modified to suit the addressed case. Only in case of two regular grids, each sensor contributes one observation for each point. In order to increase this low redundancy (r=1), one seeks a local surface description, which relates the point to its neighbors. Assuming that in normal terrain each point is highly correlated with its neighbors, one approximates the local surface H(N,E) within a m x n window with help of a polynomial in terms of the point coordinates N and E.

E.g. H(N, E) becomes for a second degree polynomial approximation:

$$H(N,E) = c_o + c_1N + c_2E + c_3NE + c_4N^2 + c_5E^2 \tag{5.1}$$

The bicubic approximation in matrix form is:

$$H(N,E) = [1 \quad N \quad N^2 \quad N^3] \, \mathbf{C} \, [1 \quad E \quad E^2 \quad E^3] \tag{5.2}$$

with $\mathbf{C}$ being a 4x4 parameter matrix.

As multiple measurements are available, the number of points will outnumber the number of parameters c_i even if the surface is approximated a with polynomial of third or higher degree. E.g., in case of a cubic surface approximation, 16 parameters have to be computed. If all points are allowed to enter the fusion process within an estimator window of size m = n = 3 (nearest neighbors around a center point), the redundancy r is still 2.

The resulting equation system can be written in compact form with

$$\underline{H} = \mathbf{A}\underline{c} \tag{5.3}$$

The overdetermined system is solved by least squares adjustment, which leads with (3. 12) to the equation for the vector of unknowns $\underline{c}$

$$\underline{c} = (\mathbf{A}^{\mathbf{T}}\mathbf{A})^{-1}\mathbf{A}^{\mathbf{T}}\underline{H} \tag{5.4}$$

With the weight matrix P, (5. 4) becomes

$$\underline{c} = (\mathbf{A}^{\mathbf{T}}\mathbf{P}\mathbf{A})^{-1}\mathbf{A}^{\mathbf{T}}\mathbf{P}\underline{H} \tag{5.5}$$

The estimated height for a point $\underline{P}$ is finally computed by employing the N and E coordinates and the calculated coefficients in the corresponding polynomial (5. 1) or (5. 2).

In other words, the local surface is approximated by a polynomial within a window, centered around a point $\underline{P}$. All measurements from both sources, which fall in this window, contribute one equation to the surface approximation. By solving for $\underline{c}$, an estimate of the local surface is obtained. As the approximated surface does not run through the reference points, the polynomial approximation filters the contributing measurements.

Polynomial surface approximation is a fast and uncomplicated method for fusing the two DTMs if they have similar grid size. The assumption that the surface is rather smooth and can therefore be approximated with a second or third order polynomial is valid with the DTM grid size achieved with ERS and SPOT, where high surface change rates (e.g. caused by man made objects) are in most cases not resolved. The high degree of redundancy increases the reliability of the fusion result, as it allows to eliminate gross errors before they affect the interpolation process. The computed polynomial is also used to interpolate those points, which have been rejected during the association procedure.

The method is extremely dependent on the proper data alignment. Any systematic differences, indicated e.g. by low redundancy or uneven distribution of similar points over the scene, strongly corrupt the fusion result. As the polynomial interpolation requires high redundancy, problems arise in areas, where fewer points have been measured – typically in changing terrain. Lower order polynomials and larger estimator windows in problematic terrain circumvent the problem on the

expense of a possibly unwanted terrain smoothing. Careful permission of unchecked but highly confident points (weights!) from a single source, which performs well in the area, will increase the measurement density in those areas.

Weighted Average The weights allow to compute a fast fusion solution. For that purpose, the arithmetic mean within the estimator window is computed from the n heights (h) weighted with p. Invalid points get zero weight. One easily verifies that the computation of the arithmetic mean m is a special case of (5. 5) as

$$\hat{H} = m = \left(\sum_{i=1}^{n} p_i \right)^{-1} \sum_{i=1}^{n} p_i H_i \tag{5.6}$$

where $\hat{}$ denotes the resulting height estimate.

The approach impresses by its simplicity of implementation. On the other hand, the shortcomings are the weight dependence of the result and the missing sensitivity of terrain shape. The result is a considerably smoothed terrain.

Most approaches for deriving the weight use distance measures. The matching correlation coefficient of the stereo-optical DTM generation and InSAR coherence (section 5.2.2) are at least qualitative accuracy indicators and may also serve for the calculation of p *(Honikel, 1999)*. Furthermore, height measurements over forests show generally lower correlation or coherence, so that they indicate a required further treatment in the DTM editing process. The bias over forests will be similar, as the response comes from approximately the same height with SPOT and ERS. With increasing wavelength (e.g. L-Band), SAR penetrates the vegetation, resulting in measurements originating closer from the surface. On the other hand, buildings (if resolved) will show relatively high correlation respectively coherence and the same bias. The presented estimation procedures do not take this bias into account, as long as it is similar with both sensors. In brief, DTM editing hints can be retrieved from the correlation/coherence comparison, but are not treated here any further.

5.3.2   Collocation

The general formulation of the prediction problem has been given in section 3.6.2. Assuming that in (3. 14) $\underline{f}$ is already known, the problem becomes

$$\underline{g}' - \mathbf{B}\underline{f} = \mathbf{N}'\underline{v} \tag{5. 7}$$

The previous equations are now interpreted in respect to the original problem of height data fusion. The initial assumption of the prediction is that the observed terrain is the sum of a systematic part $\mathbf{B}\underline{f}$, which represents the macrostructure of the terrain, with the terrain microstructure $\mathbf{N}'\underline{v}$, which varies around this systematic part and is interpreted as superposed random terrain. In the narrow sense, $\mathbf{N}'\underline{v}$ is still the error, distributed around the coarse surface. The terrain microstructure is defined by the height of the reference points relative to the trend. The heights are affected by a measurement error.

Following the notation of signal theory, $\mathbf{N}'\underline{v}$ is therefore often denoted as signal, while $\mathbf{B}\underline{f}$ is referred to as trend. In order to obtain a best estimate for the random part, the systematic has to be split from the observations (5. 7). After removal of the systematic, the observations can be interpreted as random variables from which a best estimate for $\underline{v}$ is determined in the following.

The observations relative to the trend are now split themselves in two parts, the actual terrain $\underline{s}$, which is the systematic part between trend and actual surface, and the random measurement error $\underline{r}$ (Fig. 5.1).

$$\underline{v} = \underline{s} + \underline{r} \tag{5. 8}$$
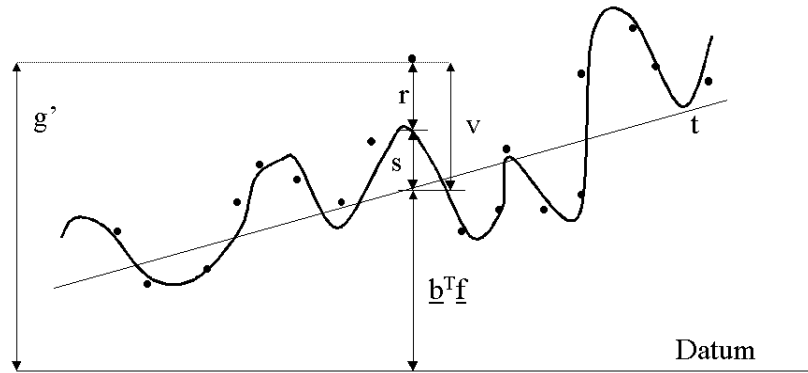

Fig. 5.1 Collocation illustration. The observation g' is split in a trend part t representing the terrain macrostructure and the terrain microstructure, consisting of a systematic (s) and random (r) part.

By rearranging (5. 7) with $\mathbf{N} = (\mathbf{N}', -\mathbf{I})$ and $\underline{g} = \underline{g}' - \mathbf{B}\underline{f}$, it becomes with (5. 8)

$$\underline{g} = \mathbf{N}\underline{s} - \underline{r} \qquad\qquad (5.\ 9)$$

The equation is the Wiener model equation, which has been introduced in section 3.6.2. The solution, which determines the systematic in presence of the random noise $\underline{r}$, has also been given there. With (3. 24), the best estimate for $\underline{s}$ is computed by

$$\overset{\wedge}{\underline{s}} = \mathbf{K_{sg}}\mathbf{K_{gg}^{-1}}\underline{g} \qquad\qquad (5.\ 10)$$

with the $\mathbf{K_{sg}}$ the cross-covariance matrix of the unknowns $\underline{s}$ and observations $\underline{g}$ and $\mathbf{K_{gg}}$ the auto-covariance matrix of the observations.

The solution is identical to equation (3. 24), which has already been used for interferogram restoration. Actually, the task of separating a slow changing, i.e. systematic, part from the signal is the same in both applications. In contrast to the height fusion discussed here, there is no need to remove the trend in interferogram restoration, as the phases are changing in a 2π interval around 0. The solution offered by (5. 10) is interpreted differently in both approaches. For image restoration, it represents the deconvolved image, compensated from the blurring with additional noise. The elements of the deconvolution matrix are points on the point spread function. In case of surface reconstruction, (5. 10) is understood geometrically as summation of rotational body surfaces centered around the observations. The surface is the covariance function between two points P_i and P_k in terms of their distance d.

By inspection of (5. 10), two major facts can be concluded. Firstly, the trend needs to be split from the observations in order to retrieve the best estimate for the surface. Only trend free observations can be interpreted as random variables from which a best estimate can be derived. Secondly, the solution can be derived from the cross covariance and covariance matrices, without knowing the matrix $\mathbf{N}$. This property makes the approach so popular for stereo-optical DTM interpolation and filtering *(Kraus, 1973)*. Moreover, it is also an option for data fusion. *Felus and Csatho (2000)* used collocation for the fusion of small scale map height information with ERS-1 radar altimeter data.

Application Collocation offers the option of fusing InSAR and stereo-optical measurements by taking advantage of their individual properties. As shown in the previous chapters, the different techniques generate comparable results. As an example, the grid size of the SPOT and ERS DTMs is routinely between 20 - 50 m. However, ERS has a higher potential in accuracy and amount of

measured points. On the other hand, InSAR height measurement is more prone to systematic errors than the stereo-optical counterpart. Depending on the baseline length, baseline errors or atmospheric effects are reflected in a bias or erroneous trend (section 2.2.10).

An interesting fusion option is therefore the fusion of an existing low resolution DTM with newly acquired data, e.g. from InSAR. The next section focuses on the improvement of sparse SPOT measurements or the enhancement of a low resolution global DTM databases, e.g. from SRTM. Of course, also DTMs of the same grid size can be fused in this way.

Realization The trend, either derived directly from the database or by a low order polynomial approximation, is removed from the observations. From the remainder, the covariance function is approximated for all valid points within a certain distance. As indicated above, high coherence indicates relative height accuracy and is applied for the validity checking, if the grid of the existing data is too coarse.

As the covariance between the height values drops with increasing distance, the covariance function k(d), in terms of the distance between the values d, is modeled by a bell shaped function with

$$k(d) = Ae^{-ad^2} \tag{5.11}$$

with $A = k(0)$ and a design constant a (Fig. 5.2). The values are determined with the least-squares approach using the n reference values and the Taylor approximation for the function

$$Ae^{-ad^2} \cong A\sum_{i=0}^{n-1}(-1)^i \frac{(ad)^{2i}}{i!} \tag{5.12}$$

Other approaches for the calculation of the covariance function have been proposed. *Kraus (2000)* uses an empirical approach to determine the curve. He calculates A from the empirical variance of the reference points and the DTM error variance and approximates a, determined in several distance intervals, by calculation of the weighted mean. *Förstner (2000)* uses the empirical variance of the reference points for A and the relationship between the Hessian **H** of the auto covariance function and gradient of the correlated part s̱ for computing a.
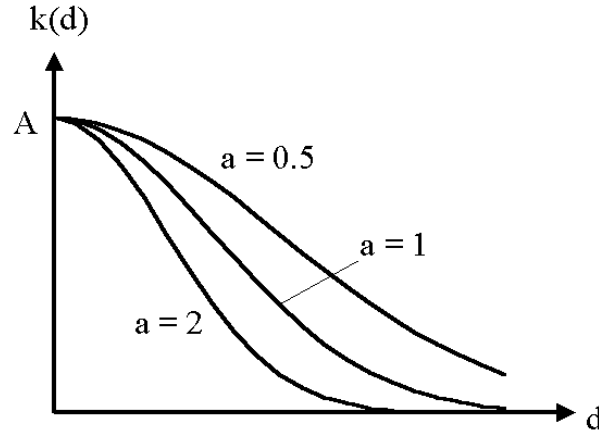
Fig. 5.2 Covariance function shape in terms of distance
d and design parameter a.

The covariance matrix $\mathbf{K_{gg}}$ is determined by inserting the distance between the reference points in
k(d) and calculating the elements $k_{ik} = k_{ki}$. The height relative to the trend s is estimated for each
point in the estimator window with (5. 10). For the concerned point, the distance d to each
reference point is calculated and inserted in the approximation of the covariance function (5. 12).
The calculated covariance vector is finally multiplied with $\mathbf{K^{-1}_{gg}}$ and $\underline{H}$, the reference heights. The
dynamic calculation and inversion of the covariance matrix within a moving estimator window
makes the least squares approach computationally expensive.

5.4 DTM Fusion in the Spatial Frequency Domain

Like any other image, an equally gridded DTM can be transformed to the spatial frequency domain
using the discrete Fourier transform. Similarly to the previous sections, the DTM g(x, y) is treated
for that purpose as superposed sum of sine and cosine waves. The Fourier transform is the well
known

$$G(u,v) = \frac{1}{N} \sum_{x=0}^{N-1} \sum_{y=0}^{N-1} g(x,y) e^{(-j2\pi(ux+vy)/N)} \qquad (5.\ 13)$$

The inverse transform is

$$g(x,y) = \frac{1}{N} \sum_{u=0}^{N-1} \sum_{v=0}^{N-1} G(u,v) e^{(j2\pi(ux+vy)/N)} \qquad (5.\ 14)$$

The Fourier transform allows to analyze the DTM with the methods of system theory. For that purpose, assume that g(x,y) is obtained from the ideal measurements f(x,y) by convolution with a position invariant function h(x,y)

$$g(x,y) = f(x,y) * h(x,y) \qquad (5.\ 15)$$

From the convolution theorem, the following frequency-domain relation holds

$$G(u,v) = F(u,v)H(u,v) \qquad (5.\ 16)$$

H(u,v) exists, if the system is stable, i.e.

$$\sum_{-\infty}^{\infty} \sum_{-\infty}^{\infty} \left| h(x,y) \right| < \infty \qquad (5.\ 17)$$

In this context, the obtained DTM is the product of the ideal measurements F(u,v) passing through a process H(u,v), denoted as system transfer function. As H(u,v) represents the measurement process, any transfer function H(u,v) $\neq$ 1 causes a *systematic* error in the result. The fine terrain structure is affected by the measurement process as, according to (5. 17), the transfer function attenuates higher terrain frequencies. The degree of attenuation depends therefore on the density and distribution of measured points and on the interpolation method. *Tempfli (1982)* gave the connection between the transfer function and the interpolation error variance with

$$\sigma_{int}^2 = \frac{1}{2} |1 - H(u,v)|^2 \cdot |G(u,v)|^2 \qquad (5.\ 18)$$

The transfer function behaves differently for the process of stereo-optical and InSAR DTM generation. For the InSAR DTM, it is described qualitatively with weak attenuation as the method measures a large number of points at least locally in high coherent regions (Fig. 5.3). The stereo principle of measuring single well identifiable points requires interpolation between the points in order to obtain a regular grid. The result is a stronger attenuation of the high frequency band, depending on the interpolation method.
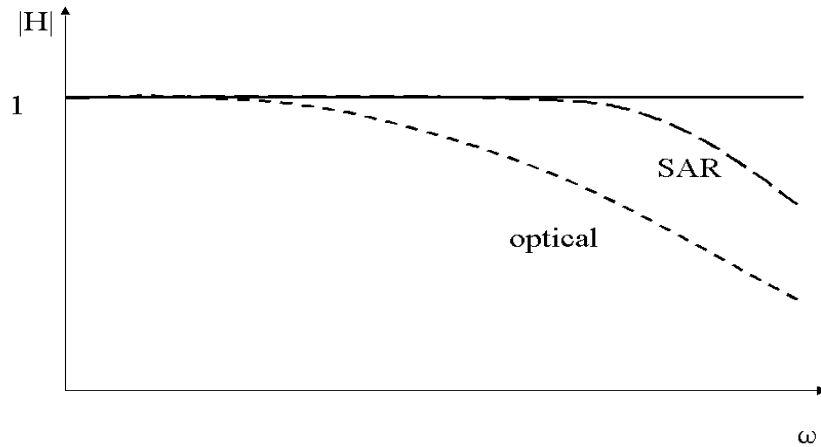
Fig. 5.3 Qualitative behavior of the transfer function of stereo-optical and InSAR DTMs. Due to the required interpolation, the high stereo-optical DTM frequencies are much more attenuated than the InSAR ones.

As shown in chapter 2, the InSAR measurement process is prone to systematic errors, corrupting the low DTM frequencies. Erroneous baseline determination results in a tilted surface, while atmospheric artifacts result in slowly changing error surfaces *(Goldstein, 1995)*, thus both affect mainly the low frequency band. On the other hand, the stereo-optical DTM generation is based on a more sophisticated satellite model that allows to keep the systematic error low, while eventual mismatched points (spikes) affect the high DTM frequencies.

Based on these assumptions, a spectral model of InSAR and stereo-optical DTM can be derived, which will serve for the intended data fusion. As can be seen in Fig. 5.4, the spectral behavior of both DTMs complement each other. Below the border frequency ω_o, the spectrum of the stereo-optical DTM is close to the ideal spectral behavior, as the noise corrupts mainly the high frequencies. For the reasons stated above, the InSAR spectrum is closer to the ideal shape above ω_o.

The fusion of the less affected high frequency band of an ERS InSAR DTM with the low frequency band of a SPOT DTM has been proposed by *Honikel (1998)*. The procedure is based on the fact that error behaviour of each DTM affects different bands in the spatial frequency domain.

By substituting the error-corrupted part of the DTM with the corresponding part of the other, the result has an improved error characteristic compared to the single source (Fig. 5.5). In order to obtain a reliable approximation of the coarse terrain course, the stereo DTM is filtered with an ideal low pass filter in the frequency domain. The slow changing terrain features are maintained, the corruptive spikes are removed. The result is a smoothed terrain, giving a first approximation of the

93

course, which will completed by the InSAR DTM features. Note that the mean of the stereo DTM, $G_{opt}(0,0)$, is in this way transferred to the resulting DTM.
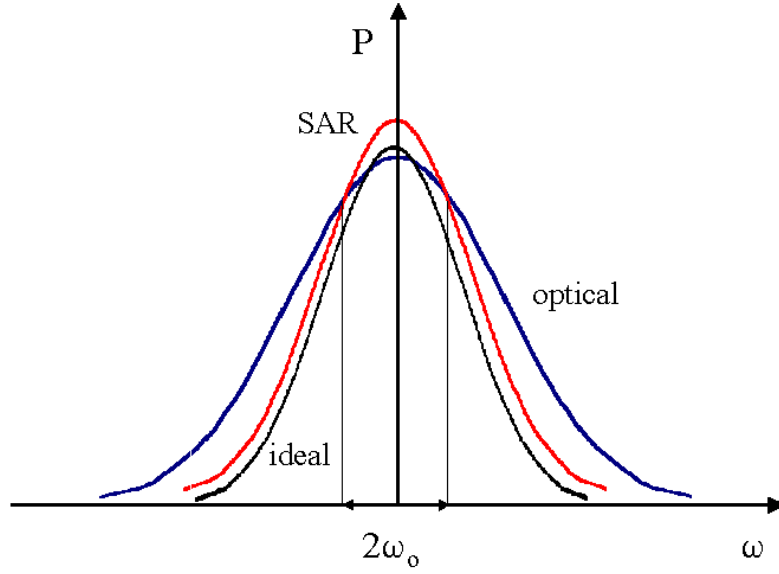

Fig. 5.4 Spectral power of InSAR and stereo-optical DTMs. While the low optical DTM frequencies are close to the uncorrupted spectrum (ideal), InSAR is more similar in the higher frequency band. The transition frequency ω_o is marked.

After high pass filtering of the InSAR DTM, the terrain details are left over. The corrupted low frequencies are filtered out and will be replaced in a final step with the low frequency part of the stereo DTM. By adding both parts, the coarse terrain course is recombined with the terrain features. The parameter ω_0 varies with the grid size of the contributing DTMs. The coarser the grid of the DTM, which contributes to the low band, the stronger the attenuation (Fig. 5.3) and the smaller the value of ω_0. The parameter can be determined directly from the intersection frequency of the amplitude spectra (Fig. 5.4). As it is less prone to systematic errors (section 2.3), the SPOT DTM is expected to approximate the auto-correlation (power) spectrum at the lower frequency band well, while InSAR DTM behaves inversely. With regard to Fig. 5.4, the SPOT power spectrum P_{SPOT} is related to the ERS InSAR spectrum P_{ERS} at the low frequency band by the gain factor G

$$\frac{G}{dB} = 10 \log_{10} \frac{P_{ERS}}{P_{SPOT}} \tag{5. 19}$$

The logarithm is used to handle the high power levels. Note that G may be less than 0 (i.e. loss). In order to automate the determination of ω_0, the frequency at the technically important 3dB gain can

be used for deriving the parameter ω_0. Tests on both procedures, spectral intersection and 3dB frequency, yielded practically the same results.

The resulting fused DTM profits from the stereo and InSAR DTM in terms of accuracy and visualisation. In contrast to the original stereo DTM, the terrain is easier to interpret, as all disturbing spikes are removed and the course of the InSAR DTM is used. In addition, the accuracy of heights of the fused DTM is higher than that of a single source. The problem of stereo-optical outliers is also solved by the procedure, as they effect the high frequencies and are removed by reliable data from the InSAR source. The whole procedure can be automated and depends only on one single parameter, the bandwidth ω_0, which decides, to which extend the individual DTMs contribute to the fusion process.
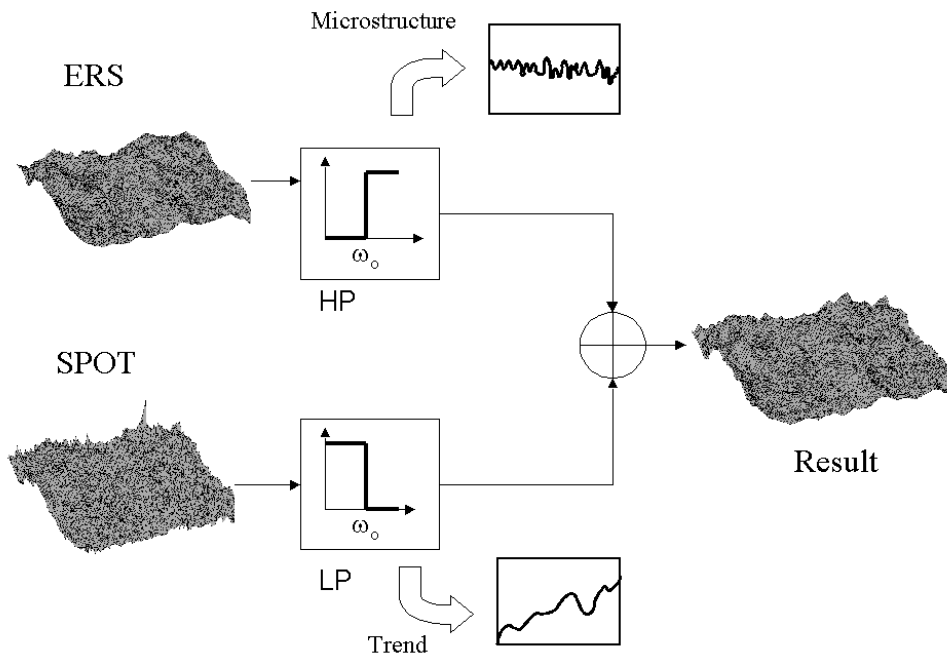
Fig. 5.5 Data fusion principle in the frequency domain. The trend is derived from the SPOT measurements, while the terrain features are provided by InSAR. The result is obtained by combining the corresponding frequency bands.

The fusion can also be performed using wavelets instead of the Fourier transform. A multi-grid approach using wavelets has been proposed by *(Ferretti et al., 1999)*. Several ERS slant range height models of different baseline taken over the Etna test site have been fused. It has been proposed to take existing SPOT measurements as datum by introducing them as subband during wavelet decomposition.

The problem of the high pass and low pass combination is the rather global assumption of the error distribution. One has to take into account that also the high terrain frequencies can be rather corrupted (slopes!) in the InSAR case and the SPOT measurements are not necessarily unbiased. Still, the procedure takes advantage from the general error behavior of the sources, can be steered with ω_0 and offers an efficient way to fuse the data.

The procedure is the approximation of the collocation approach of section 5.3.2. The trend is derived from the low pass operation while the terrain features are retrieved from the InSAR DTM with the high pass filtering. It is assumed that the InSAR measurements are only little noise affected. The noise is minimized during interferogram filtering, phase unwrapping and finally by the slant range to ground range conversion. The more general case, discussed in the previous section, can also be formulated in the frequency domain. If the measurements are subject to additional noise n(x,y), (5. 16) becomes

$$G(u, v) = F(u, v)H(u, v) + N(u, v) \tag{5. 20}$$

Taking into account that the system will attenuate the high frequencies, the noise will increasingly dominate this band. The direct approach of inverse filtering would therefore amplify the noise.

Weidner (1994) has proposed to use the Wiener filter for information preserving filtering of the terrain. The Wiener filter in the frequency domain for restoring the DTM measurements in presence of noise is given with (3. 26) by

$$W(u, v) = \frac{H^*(u, v)}{\left|H(u, v)\right|^2 + (SNR(u, v))^{-1}} \tag{5. 21}$$

where $H^*(u, v)$ denotes the conjugate complex of the transfer function, $|H(u,v)|^2 = H^*(u,v) \cdot H(u, v)$ is its power and SNR(u, v) is the signal to noise ratio. The use of the Wiener filter for data fusion has been outlined in section 3.6 and will not be discussed here in further detail. H(u,v) is either determined from a less corrupted data set or with help of the connection between coherence and height error (section 2.2.10) and (5. 18).

5.5 Summary

The concept for fusing existing SPOT with InSAR data sets on DTM product level has been realized in this chapter. The InSAR measurements serve as additional observations in order to increase the accuracy of the polynomial surface approximation used for the interpolation of a regular DTM grid. As the observations can also be filtered in this way, this approach is reasonably performed with two DTMs of similar post spacing, or in order to interpolate a DTM from a combined set of irregularly distributed points. For the second case, weights like correlation or coherence are used to measure the reliability of the points, as the direct distance calculation for similarity declaration is not necessarily possible. Collocation offers besides interpolation and filtering the option of fusing a low resolution DTM with dense InSAR measurements. It has been shown in chapter 2 that InSAR is sensitive to systematic corruptions, e.g. baseline errors. Those errors are compensated with the coarser DTM. A low resolution DTM can approximate the otherwise erroneous terrain trend, which is removed from the measurements in order to achieve an optimal interpolation result. A faster approach to compensate the low frequency errors has been realized in the spatial frequency domain. Taking into account the properties of SPOT and InSAR DTMs, the behavior of their power spectra has been modeled. According to the model, the error power will dominate the SPOT high frequency band more than in case of InSAR, which is on the other hand more error corrupted at the low frequencies. The data sets are fused by filtering the DTMs and combining the filtered uncorrupted bands of both sources. The filter frequency is determined automatically. The advantage of this approach is that it can be performed with ERS and SPOT DTMs of similar resolution or with ERS and a coarser DTM.

C h a p t e r   6

RESULTS

6.1 Introduction

The data fusion method and its procedures have been tested at three different test sites, two located in Spain and one in Switzerland. All sites comprised of changing and mountainous terrain. In all cases, an ERS DTM, from a *single* interferometric pair, has been fused with a SPOT DTM in order to obtain a product having the same grid size as the national databases, to which it was afterwards compared. The national DTM database offered the opportunity to assess the error characteristics in terms of mean, root mean square error and amount and location of outliers. The results are in any way superior to the accuracy assessment with some check points, routinely used for that purpose. *Small (1998)* already noted the insufficient testing of ERS InSAR DTM accuracy, which has been carried out by many authors. As a new method is proposed in this work, it will be submitted to an in depth testing in order to clarify its potential. The testing is described in section 6.2, while the test data and results are given in the remaining sections. Section 6.3 shows the results of ERS, SPOT and the fused product in hilly terrain. As the terrain favored none of the sensors and as the acquisition interval has been identical, the individual DTMs have been compared to each other in order to give an idea of the potential of each method. Section 6.4 gives the results of the fusion of a coarse SPOT DTM with ERS tandem measurements in Switzerland. The case of fusing low-resolution with high-resolution data is there discussed with an example of pre-alpine terrain. Finally, the benefit of fusing ERS with SPOT data in mountainous terrain is evaluated in section 6.5. Not only terrain induced problems, but also atmospheric artifacts in the interferometric measurements made this site extremely demanding.

6.2 Accuracy Testing

6.2.1 Overview

The fusion testing has been carried out with ERS and SPOT data at three test sites in Spain and Switzerland. A summary of the data characteristics is given in appendix B. A DTM in the national map projection has been derived from all data sets and compared to national DTM databases, which served as reference for the quality assessment. The rms accuracy of the reference data sets has been 1m for the Spanish sites and 2-3m for the Swiss site. Although it is tempting (and has been performed) to evaluate the InSAR potential in slant range, a sound and fair quality assessment has to be performed after ground range conversion.

The evaluation has been performed in a before/after manner by first calculating the statistics of the stand-alone data sets and afterwards the statistics of the fused product. In order to facilitate the comparison, the generated DTMs were sampled into the same grid as the reference DTMs (post spacing Spain: 30m, Switzerland: 25m). Small measurement gaps were filled by interpolation. A large gap in the Swiss SPOT DTM was left open, as it could not reasonably be filled. The statistic measures mean (μ), standard deviation (σ) and root mean square (rms) error were computed from the ensemble of differences between reference and measurements. Outliers were labeled as errors larger than 3 times the standard deviation of the error, which is approximately 40m for ERS and SPOT. In addition, the minimal and maximal height error (ΔH_{min} and ΔH_{max}) have been computed for both DTMs and the fusion result. The results of the fused DTMs have been compared to the original ERS and SPOT measurements in all categories. In order to keep the comparison transparently, the outlier criterion of $\Delta H > 40m$ is applied to the fusion result as well. The reference itself has only been used for the validation. At site Spain I, a undersampled (factor 4) reference DTM was used for simulating SRTM data for frequency domain fusion.

Although the first aim was to assess the error quantitatively, still some tests have been performed in order to characterize the second order quality criterion, terrain shape. For that purpose some DTM subsets have been examined and evaluated visually.

6.2.2 Surface Influence

Unless stated otherwise, all results relate directly to the output of the measurement or fusion process. Except the interpolation, the DTMs are not edited at all at this stage. Editing can significantly increase the DTM quality, but depends on the invested time and manual intervention

of an operator. When comparing the measurements with the 'bare soil' reference, a bias is encountered especially in wooded terrain. Although both SPOT and ERS are expected to deliver biased measurements over woods, tree top height assessment is not reasonable, due to the strong noise corruption of the measurements. In order to study the vegetation influence on the measurements, land cover maps have been applied. For the Spanish sites, the land cover map is based on the Corine map and comprised 5 main classes (artificial surfaces, agricultural areas, forests, wetlands and water bodies), which are subdivided in a total of 63 subclasses. The pixel size is with 30m the same as that of the DTM. The bare soil accuracy assessment has been carried out by masking out all regions with elevated vegetation or water bodies. For the Swiss site, the national pixel map has been resampled from original 3m to fit the 25m post spacing of the national DTM database, the DHM25. The pixel map comprises 6 classes, from which the forest layer has been used for the masking. The national Landsat TM orthoimage mosaic (25m pixelsize) has been found useful for additional validation. As expected, the accuracy rose in all cases after masking out the vegetated areas.

6.3 Results of the Test Site Spain I

6.3.1 Test Site

The test site is situated in southern Catalonia, south of Lleida. The test area comprises an area of more than 950km^2, the minimum elevation is 41m, the maximum elevation is 1085m. In general, the terrain is hilly, marking the transition from the Catalonian coastal mountain chain, situated in the south, to the plane in the north (Plana d'Urgell). Some mountains are included, especially in the south and some in the east (Fig. 6.1, Fig. B1 (appendix)), while the north is relatively flat. The land use is dominated by agricultural areas, mostly permanent crops, and forest stands, mostly olive groves. In the end of summer, when all images have been taken, the region is very dry. Due to the type of land cover and – use, only few changes occurred from image to image, making the site an almost ideal test area for repeat pass systems.

The test data have been provided by the Cartographic Institute of Catalonia (ICC) during the EU concerted action ORFEAS *(Patias, 1998)*(section C (appendix)). The research has been carried out by 5 institutes from Greece, Spain, Italy, Austria and Switzerland.
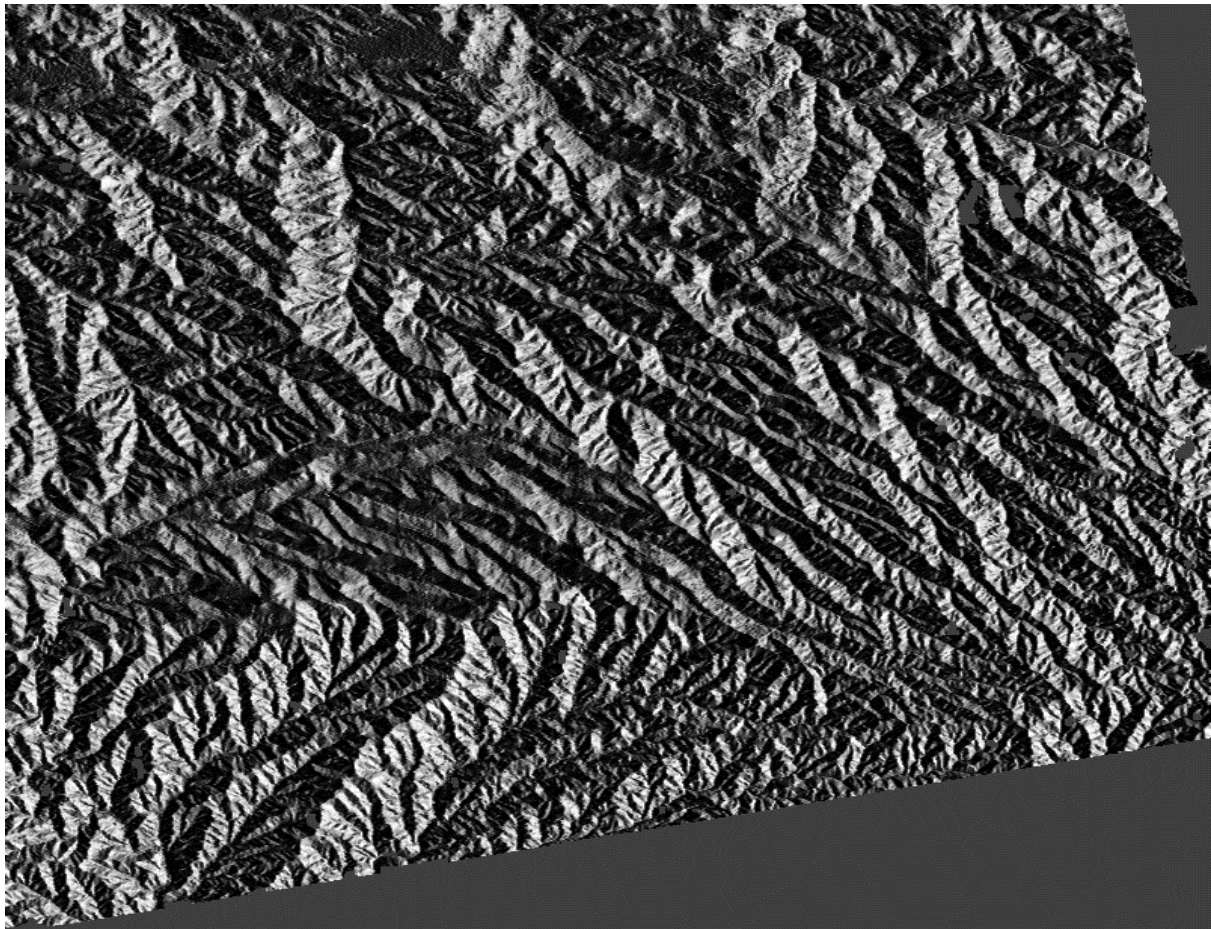
Fig. 6.1 Test site Spain I (shaded relief). Although far from being flat, the topography changes moderately and offered the opportunity for a fair comparison of the SPOT and ERS DTM.

6.3.2   SPOT

Few clouds, base to height ratio, a three day interval between the images and good texture favored stereo-optical DTM generation. Still, the raw image quality was rather low, demanding image preprocessing including chess pattern noise removal, low pass and Wallis filtering. For the determination of exterior orientation, 11 control points have been used for the *Kratky (1989)* sensor model. The exterior orientation has been used on the digital photogrammetric workstation 770 from LH systems for DTM generation. An in depth description of the SPOT processing is given in *(Patias, 1998)*.

The SPOT results are given in Tab. 6.1. The DTM is in the same 30m grid as the reference data. All results are within the expectation. The low mean error, indicates that the sensor model applied well. The rms error of the DTM is beyond pixel size, although some large outliers are found.

6.3.3   ERS

The terrain suited InSAR DTM generation, as the topographic changes were generally not too abrupt. The baseline length of 160m, resulting in an ambiguity height of 55m, is therefore well adapted to the terrain, although problems in the mountainous part occurred. The Spanish project partners encountered a very high mean error in this test site. As D-PAF state vectors have been used for baseline modelling, it was concluded that the provided control points must be erroneous and a new set of 6 points had to be matched manually from the given data.

The average coherence was with 0.56 rather high, due to the landcover properties mentioned above. Still, wooded and/or mountainous regions posed a problem for the branch cut phase unwrapping and some measurement holes remained. In order to avoid any information and error leakage from SPOT, no flattening has been carried out, which made sense also in respect to the SPOT accuracy. The Wiener unwrapping method has been tested using the simulation from SPOT, supporting the phase unwrapping in some residue rich areas. No large holes remained after the Wiener phase unwrapping and the high measurement density could be utilized for the fusion with the stereo DTM.

After phase - height conversion, the InSAR DTM has been generated through ground range conversion and UTM projection of the InSAR height measurements. The SPOT DTM has not been used for supporting the geocoding. The result of the stand alone ERS DTM is given in Tab. 6.1.

The relatively low mean proves the assumption of the originally erroneous control points. It is a fraction of which was encountered by ICC, whose result also suffered from the partially applied least squares unwrapping. The rms/standard deviation is within the expectation range and is comparable to that achieved by the ICC.

6.3.4   Comparison

Both methods perform within their expectation, when compared to the reference (Tab. 6.1).

InSAR produces only few outliers, as corrupted phases fall prey to the interferogram filtering. Practically no interpolation had to be carried out. The errors are related to the topography and occur in the mountainous part of the data set, located along the slopes (Fig. 6.2a). Vegetation, especially forest stands, increase the problems there. Still, one notes that InSAR accuracy in these

regions is higher than expected, due to the Wiener phase unwrapping. Due to the relatively high coherence of the site, the errors are expected to originate from the baseline and atmospheric artifacts. The slight DTM tilt, stretching from south-west to the north-east is visible in Fig. 6.2a. The heights are systematically too high at the south-west corner, while the terrain is underestimated in the north-east corner. The effect is not indicated in the mean error.

The SPOT results are quantitatively similar, but the nature of the errors is different. Generally, the error less systematic than with InSAR, but much more randomly occurring. The mean is very low due to the strict sensor model. This can qualitatively be concluded by visual inspection as only few features can be recognized. The most and largest errors occur in the mountainous part, but also randomly throughout the whole scene. A number of mismatched points is located in the north-west corner, due to a repetitive pattern of olive tree stands. Fig. 6.2b shows the resulting error surface.
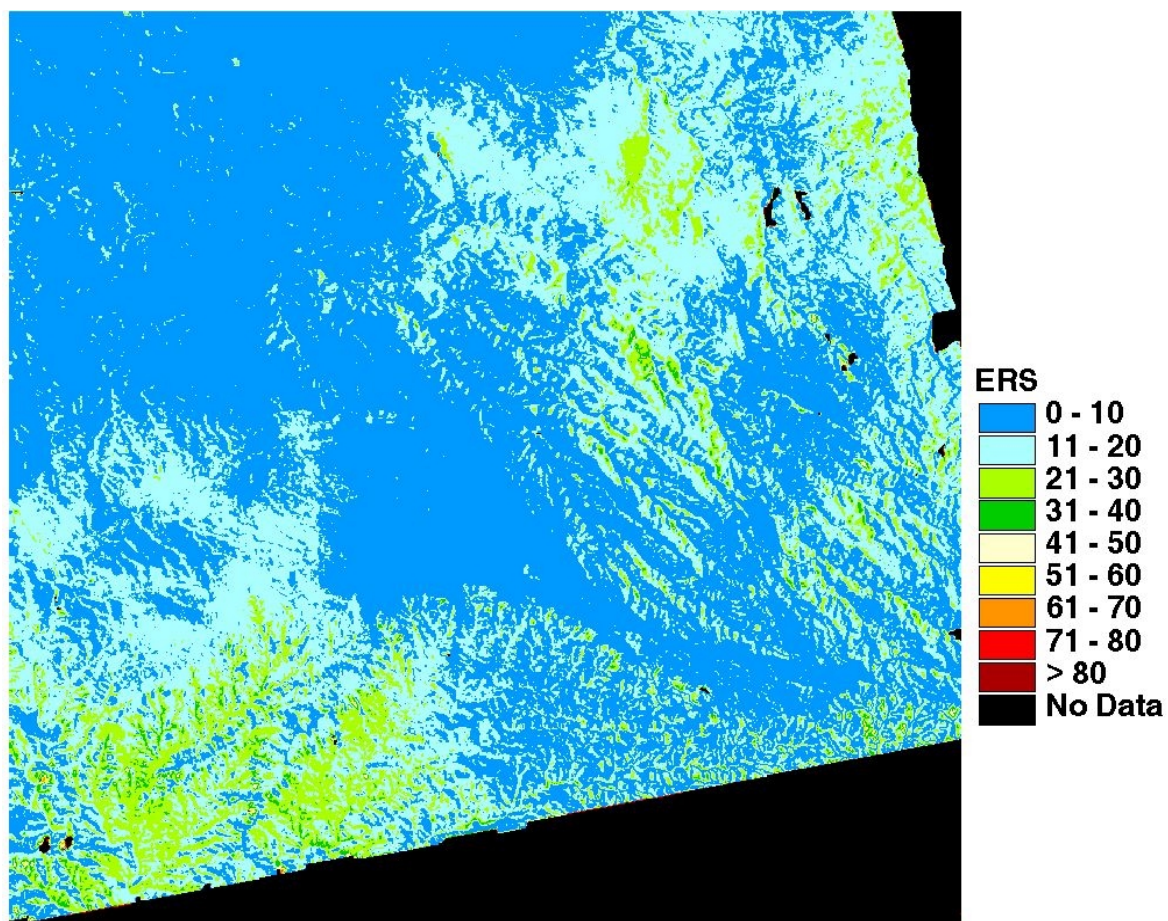

Fig. 6.2a Absolute height difference between the ERS DTM and the reference. The error in the flatter regions is below 10m. As can be seen, the InSAR error is mainly of systematic nature and related to topography. Beside the errors along the slopes, the surface is tilted from the SW to the NE corner.
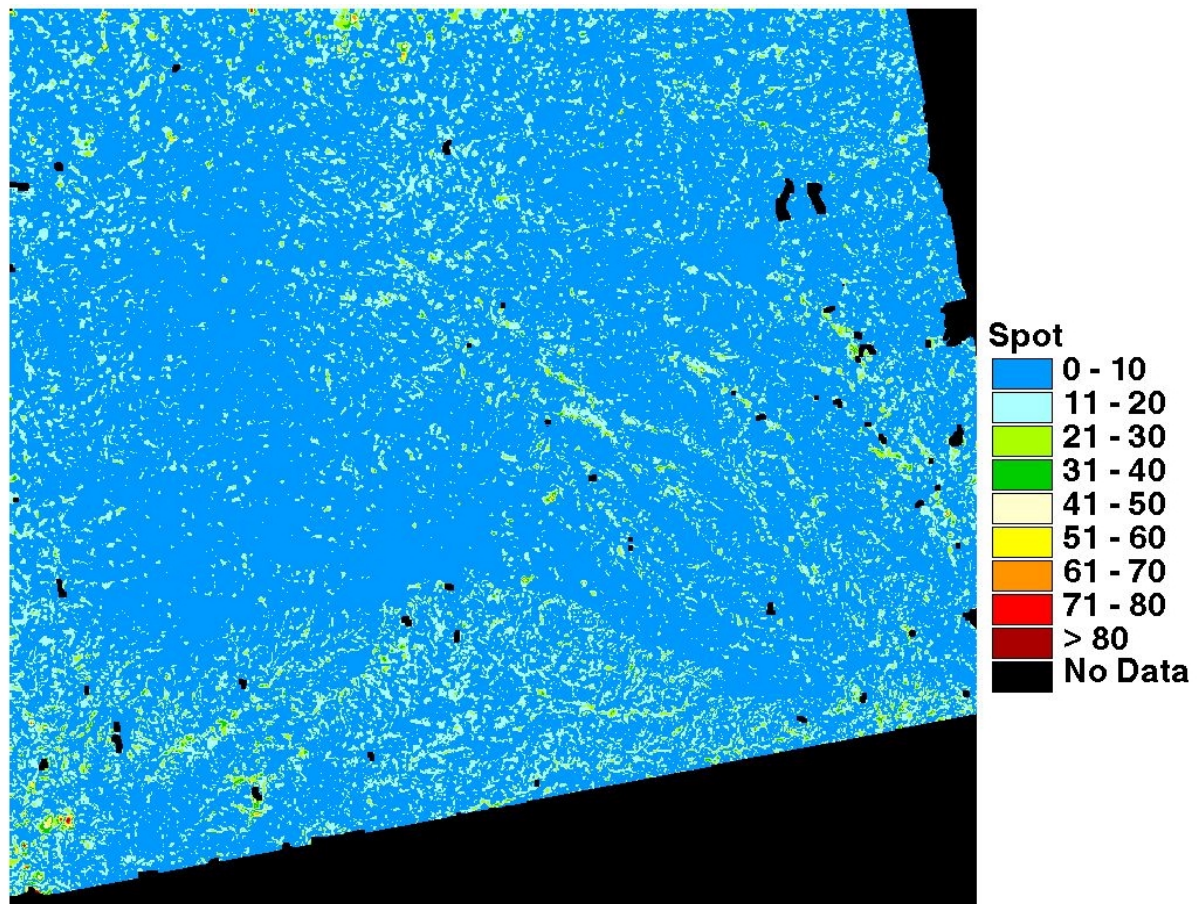
Fig. 6.2b Absolute height difference between SPOT and the reference DTM. The SPOT errors are less systematic than InSAR, but randomly distributed throughout the scene. Problems in the mountains are less pronounced.

6.3.5   Fusion

Spatial Domain

Alignment Both data sets have been projected in the UTM projection, zone 31 with ellipsoidal datum ED50. The post spacing is 30m. Visual inspection of the data indicated no need to for planimetric adjustment. An altimetric adjustment has been performed by approximating the tilt, which was introduced by the limited control point accuracy. The tilt was indicated by a systematic decrease of similar points and has been removed with the SPOT DTM.

Association The major association measure was the altimetric difference between the data. Points, differing by more than |15m|, the expected rms error of both sources, were not allowed to pass through the gating. In order to increase the amount of points and to overcome no show effects from the individual sensor, matching cross correlation and coherence were introduced as confidence measures to fill those holes with single source measurements. In cases where the association failure was clearly to be associated with one of the sources, highly confident single

measurements were allowed to enter the fusion process. The measurement holes remained very small and localized in this way.

Fusion For data fusion, polynomial interpolation has been selected, as both DTMs had the same grid size and comparable accuracy. A second order polynomial adjustment has been found useful for this type of terrain and has been performed in a 3x3 window. The results are given in Tab. 6.1.

	SPOT	**ERS**	**Fused**	
			Similar points	Filled
Σ posts	514'635	514'635	451'837	514'635
μ [m]	0.7	0.23	-0.15	0.1
σ, rms [m]	9.6, 9.5	11.9, 11.9	5.5, 5.5	6.3, 6.3
ΔH_{min} , ΔH_{max} [m]	-118, 158	-79.3, 72	-36.3, 39.6	-36.3, 52.6
$\|\Delta H\| > 40m$ [%]	5.2	0.01	0	0

Tab. 6.1 Error statistics before and after the data fusion procedure at Spain I. The category 'Fused' is divided in the result of the actual fusion process (similar points), where both sensors contribute and the filled final result, which has been enhanced by using high quality points for filling the holes.

The results are related to the fused measurements. Some 60'000 grid points have been excluded from the fusion process, as the height, measured by each sensor, differed too much (Fig. 6.3a). The holes, occurring mostly at the slopes, have been filled with measurements, selected according to their quality (sections 5.2.2 and 5.3.1). After grid interpolation, the rms error increased only little (0.8m), as comparatively few points needed to be interpolated (Fig. 6.3b). One notices the significant DTM improvement in all terms. Most errors are below 10m, the rms error reaches clearly sub-pixel accuracy. It decreases by approximately 50% in comparison to both sources. It is half the image pixelsize of SPOT and a fourth of ERS and demonstrates the accuracy potential of spaceborne DTMs. It has to be stated again that except the gating, the measurements are not manually edited at all. Therefore, the results relate measured surface heights to topographic heights. The effect of landcover on the rms error is approximately 1m, which has been assessed when comparing only regions with little landcover with the reference (section 6.2.2). The rms is given for the whole DTM, but is considerably lower in the flat regions of the DTM (~3-4m) and larger in the mountainous part (~7m). The redundancy removes virtually all outliers and thus increases the reliability of the DTM. Few errors larger than 40m have been encountered, which means that all outliers of both sources could be removed by the method, proving the sources to behave complimentarily.
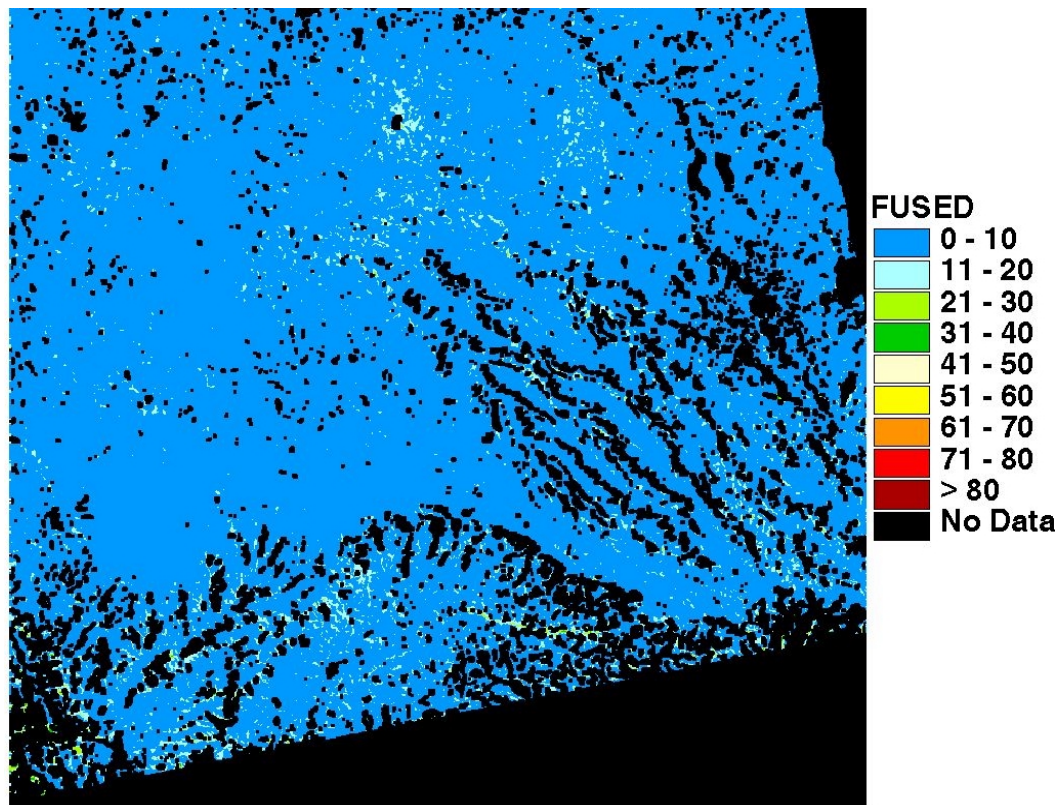
Fig. 6.3a Error surface after fusion. Only few differences larger than 10m are found after the fusion. The black points have been rejected from the fusion procedure, which prevented outliers from entering the estimation procedure. The tilt in the ERS DTM has been compensated before the fusion with the SPOT DTM.
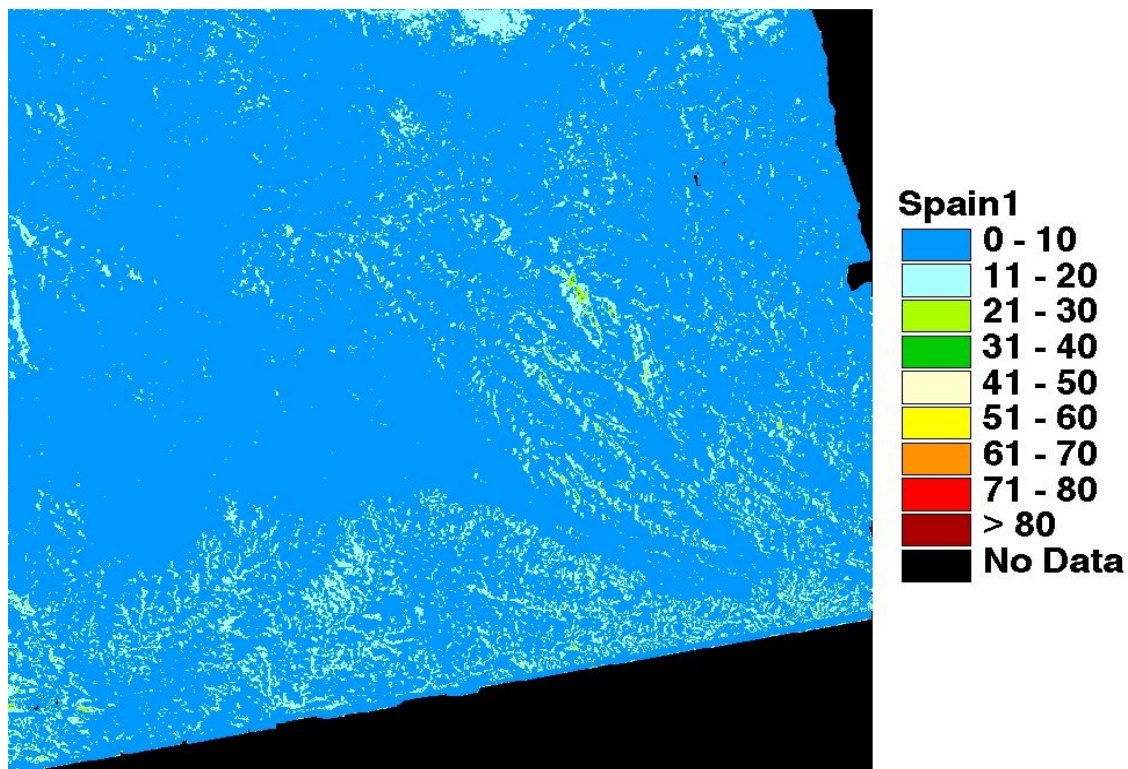
Fig. 6.3b Errors of the final result. The holes have been filled with reasonable points from each sensor, the remaining gaps have been interpolated. The quality of the single sensor measurement has been determined with help of correlation coefficient and coherence. Due to this choice of quality points (instead of interpolation), error larger than 30m hardly occur after filling. Generally, the error in the filled areas is between 11 and 20m.

107

Spatial Frequency Domain

A 15x15km^2 terrain subset (Fig. 6.5) has been used for the verification of the frequency domain fusion. The site is located at the foot of the mountains and contained hilly and mountainous terrain. The minimum height was 160m and the maximum height was 566m. The stand alone results are given in Tab. 6.2. The results are slightly better than the global ones, due to the less extreme terrain.

	SPOT	ERS
Σ posts	262'144	262'144
μ [m]	-0.3	1.7
σ, rms [m]	8.9, 8.9	8.9, 9
ΔH_{min} , ΔH_{max} [m]	-77, 105	-91, 44
$|\Delta H| > 40m$ [%]	6	0.1

Tab. 6.2 Errors of the stand alone sources at the test site.

In order to study the error effect in the frequency domain, the autocorrelation spectra of the DTMs have been calculated (Fig. 6.4). The SPOT DTM spectrum is similar to the reference in a very limited band around the origin. The higher the frequency, the more the spectrum is dominated by the noise, due to mismatched points and interpolation. In contrast, the ERS DTM spectrum is qualitatively very similar to the reference, but differs strongly around the mean, which is mainly due to the baseline effect mentioned above. A shaded relief presentation is given in Fig. 6.5.
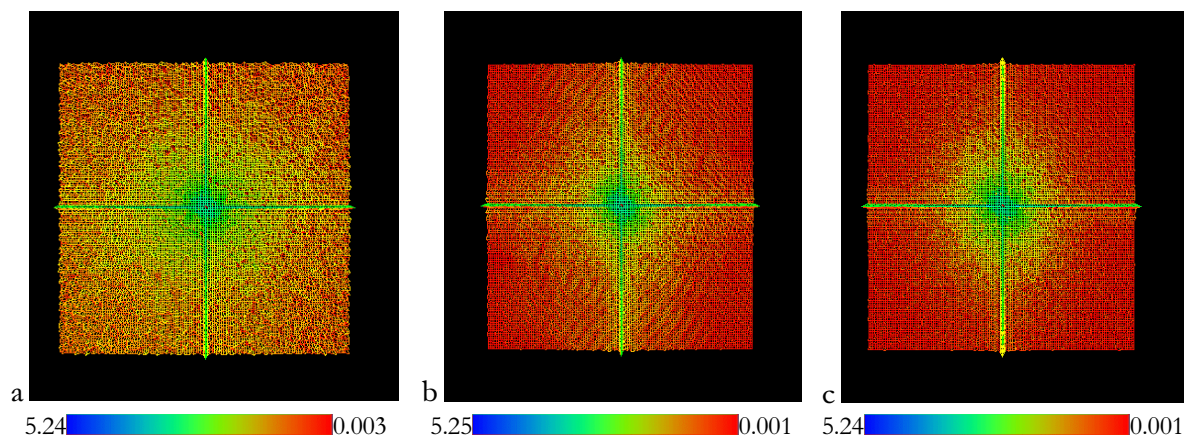

Fig. 6.4 DTM autocorrelation spectra (values: log(magnitude + 1)). The noise floor is clearly increased in the SPOT spectrum (a). The InSAR (b) mean is increased, but its spectrum resembles very much the reference (c).
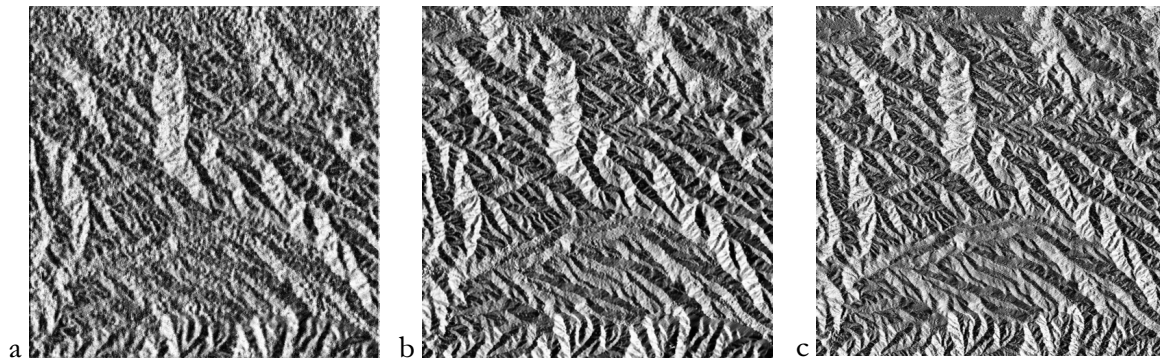
Fig. 6.5 Shaded relief illustration of the sub-area. While the SPOT relief (a) looks noisy, the difference between InSAR (b) and reference (c) is much less pronounced.

Based on this spectral behavior, three experiments for combining the higher InSAR frequencies with the low frequency band of other data have been done. Firstly, the effect of a coarse DTM, simulated by extreme low pass filtering of the reference is studied (Fig. 6.6). This is done in order to assess the InSAR error behavior. Secondly, the use of small scale data, such as SRTM, is examined. The commercially available 3" SRTM data will show a height error of 10-20m (*Rogers et al. 2001*). For simulating such a data set, the reference DTM has been resampled to a 120m grid. The height error after undersampling was 7m. Thirdly, the use of the low passed SPOT DTM has been assessed. The results of all three categories are given in Tab. 6.3.

The rms is 0.7m lower in all cases for the 'bare soil' accuracy assessment. The result proves the assumptions made in respect to the error behavior. As almost no interpolation has been needed for the InSAR DTM generation, the transfer function is rather stable, meaning little attenuation for the most part of the frequency band. Moreover, the error concentrates around the mean, indicating the baseline and atmospheric influence. If this mean is replaced with more valid measurements, InSAR is able to reach its theoretical accuracy limit, which is around 3m, as the average coherence was 0.6 (section 2.2.10). A coarse DTM suffices to contribute this mean with moderate expense, as can be seen at the 'Reference' and the 'SRTM' result.

Another advantage of this method is the maintenance of all points. The result of the same test site with the polynomial approach produced a slightly worse result (5.2m rms) for the 'fused measurements only' error assessment. After interpolation to a complete DTM, the rms error dropped to 6m, which is 25% worse than the frequency domain error.

	Reference	**'SRTM'**	**SPOT**
Σ posts	262'144	262'144	262'144
μ [m]	0.02	-0.7	-0.3
σ, rms [m]	3.7, 3.7	4.2, 4.3	4.8, 4.8
ΔH_{min}, ΔH_{max} [m]	-31, 38	-38, 41	-39, 25
$|\Delta H| > 40$m [%]	0	0	0

Tab. 6.3 Errors after frequency domain fusion of the InSAR DTM with the three fusion options: 'Reference', the low pass filtered reference, the simulated SRTM using the resampled reference and the low passed SPOT DTM.
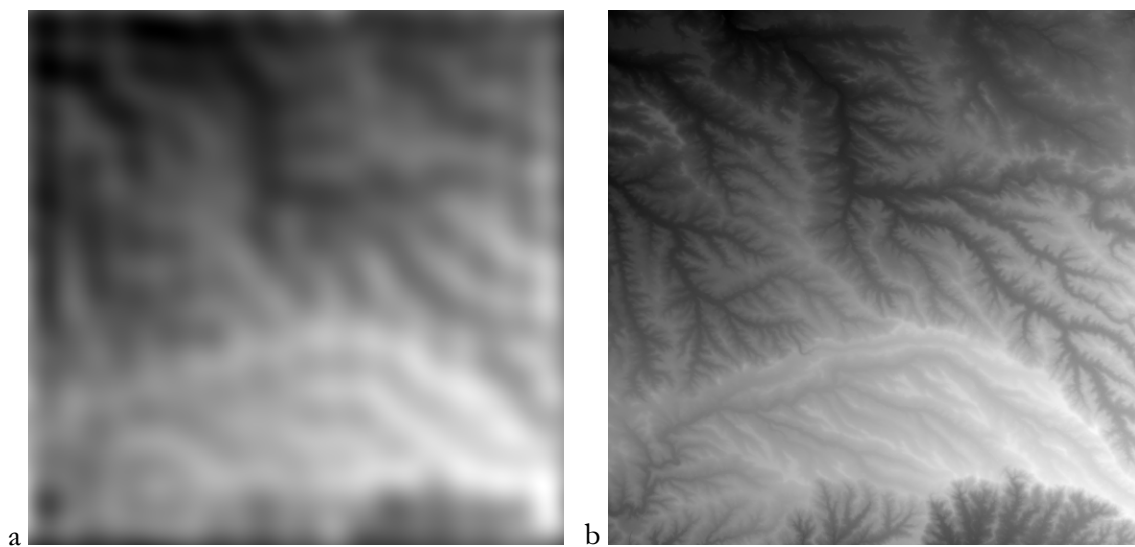

Fig. 6.6 Spatial domain fusion. An extremely low passed DTM (a) suffices for removing the low frequencies, which dominate the InSAR DTM error statistic. Due to the InSAR measurement density the terrain structure is well displayed and is preserved after the high pass filtering (b).

6.4 Results of the Swiss Test Site

6.4.1   Test Site

The site covers the 1:25'000 national map sheet 1224 (Moudon) and comprises an area of 150km^2 in a pre-alpine landscape with intensive landuse (agriculture, forestry) (section B1 (appendix)). The height difference between minimum (513m) and maximum (1413m) height is 900m. In the west of the test site, a gorge along the La Broye river could not be resolved by neither technique, while SPOT measured at least some points at the 'Les Alpettes' mountains in the south east. The main part of the site consists of rolling terrain. The purpose in Switzerland was to show the updating capabilities of the ERS data and to evaluate the combined use in pre-alpine terrain.

110

The national DTM with 25m grid-size served as reference. The points are given in an oblique mercator projection, with the Bessel ellipsoid as datum. The error is quoted with 2-3m in such a terrain *(Bundesamt für Landestopographie, 2001).*

6.4.2 SPOT

The SPOT DTM has been generated within an earlier study on automated point matching *(Baltsavias and Stallmann, 1992).* A more detailed description about the data set and its processing is given there. Due to the long SPOT repeat pass interval during the vegetation period, only relatively few points could originally be matched (10'757), which were not evenly distributed throughout the scene. Large measurement gaps had to be left open in order to avoid large interpolation errors, when interpolating to the 25m raster (Fig. 6.7). Therefore, 50m or 100m were much more reasonable grid sizes for the data. In addition to the holes, quite some large errors occurred, which further diminished the use of the DTM. The error statistic after interpolation to the raster is given in Tab. 6.4.
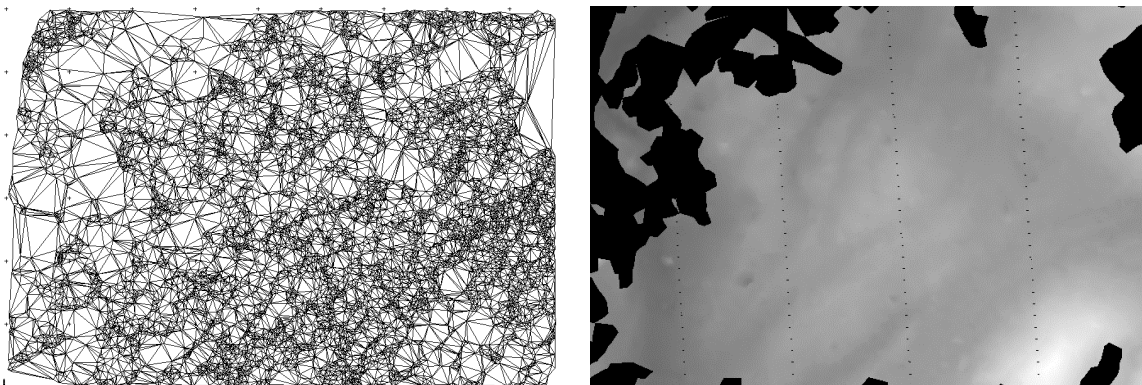

Fig. 6.7 SPOT TIN and interpolated DTM. A complete DTM could not reasonably be interpolated, due to the distribution of matched points. Large gaps remained.

6.4.3 ERS

The DTM has been generated with Tandem data. The ERS baseline length, computed from the D-PAF orbital data, was with 106m adapted for the terrain, which was well resolved, except some steep areas (Fig. 6.8). The baseline has been refined (section 4.6) with 6 control points, which have been matched manually from the corresponding national 1:25'000 map sheet. The impact of the control point accuracy on the DTM has been reported by *Renaudin (2000),* who observed a strong systematic, when processing the data set with in part weakly matched points (Fig. 4.8).

Despite the season, the coherence remained stable (average: 0.5) between the passes (Fig. 6.8), keeping interpolation within limited regions. The main processing problem posed the woods, which

are spread throughout the scene and were indicated with low coherence. Together with the steep slopes along the gorge and the mountains, they caused some residue rich zones, which could not be automatically unwrapped and were treated with help of the SPOT simulations.
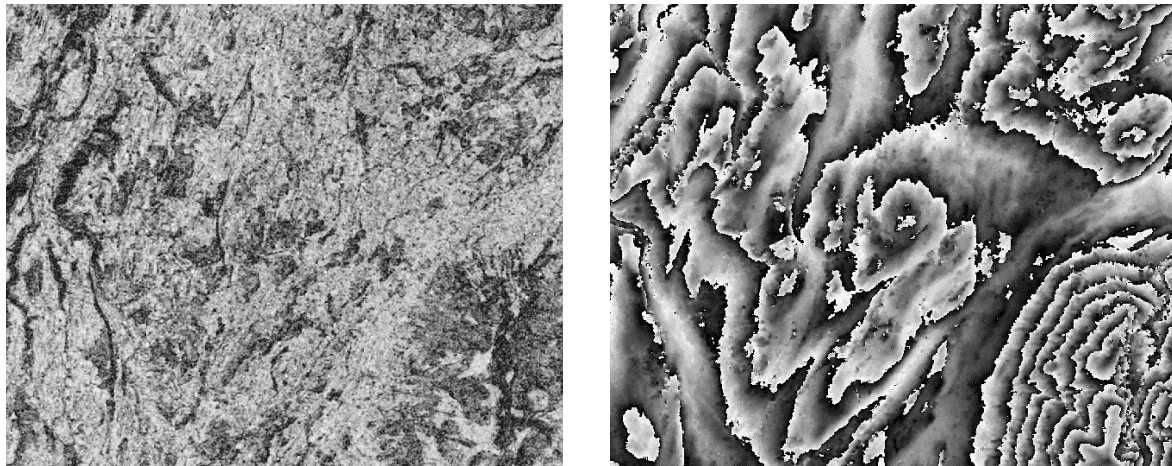

Fig. 6.8 SAR coherence and interferogram. The single day interval and the short baseline allowed resolving most part of the site. As indicated in the low coherence, problems occurred at the forests and in the mountainous part (lower right) of the site.

6.4.4   Comparison

ERS was able to deliver a complete DTM with an rms error of 11.7m, which is rather good for the encountered circumstances (Tab. 6.4). The influence of the vegetation on the error more significant than in the Spanish test sites, as indicated in the mean error. The bias over wooded areas is more than 20m in the ERS case, resulting in a global 2m rms error decrease, when comparing only the agricultural areas with the reference. The bias roughly corresponds to the top height of the firs and spruces found at the woods, although larger errors also occurred. Large measurement errors are also found along the gorge and on the mountain sides, facing the sensor (layover). Although the control points have been revised in respect to the prior results, an error remained due to the very few features, which could reliably discriminated for control point matching (Fig. 4.7).

For the purpose of comparing the data, the SPOT measurements have been interpolated to a 25m raster (some gaps have been left open). Despite the problems stated above, the result is at least quantitatively within the expectation (Tab. 6.4). Most matched points are found in the rolling and mountainous part of the terrain, where also the highest accuracy was achieved. Nevertheless, the amount of points indicates that large portions could not be interpolated and therefore delivered no redundancy. In part large matching errors were found in all over the scene.

6.4.5 DTM Fusion

Strategy As the weak SPOT performance permitted no direct fusion of measurements, a different strategy has been pursued. The SPOT measurements were used as far as possible as redundant source in the overlapping part of the site. Therefore, the 25m SPOT DTM was applied for a first fusion with the ERS measurements. As will be described in the following, the remaining part was filled with stand alone highly coherent ERS and SPOT measurements in order to achieve the best possible measurement distribution for the final interpolation. For that purpose, the error reduced SPOT measurements, now interpolated in a 100m grid, served as trend, which was removed from the fused DTM of the first pass, before least squares interpolation and filtering.

Alignment and Association A DTM in reference grid was derived from both sources. The problem was to preserve as many points as possible for the fusion, while detecting and removing blunders. In order to detect the coarse SPOT errors, a threshold of 20m has been applied for the difference between ERS and SPOT measurements. A systematic trend could not be identified during the association. The rejected values have been cross checked with the ERS coherence. In case that the difference was greater than the threshold and the coherence was greater than 0.3, the SPOT value was rejected, while the ERS one was allowed to enter the fusion procedure. In mountainous terrain, where the coherence was beyond 0.3 the SPOT value was taken. The rather low coherence boundary was set for the sake of keeping as many points as possible. In this way, only 40k points had to be interpolated. On the other hand, the accuracy of the points used for filling was in part very low. From the reduced SPOT data, a coarse 100m DTM has been interpolated. All procedures have been carried out automatically.

Fusion The fusion has been performed in two stages. Firstly, the surface was approximated with a second order polynomial in those parts of the site, which were covered by both sources. Afterwards, coherent ERS measurements were added to the result in the non overlapping part. The coarse SPOT DTM has then been subtracted from the measurements, in order to compensate the trend and a *complete* DTM for the map sheet was derived by interpolation. The results of the fusion and the sources are given in Tab. 6.4.

The fused DTM is superior in all categories. The rms is decreased by 5.5m or 46% in respect to the sources. As the coherence boundary was set rather low for association, the vegetation effect on this result must still be considered. The contribution of the vegetation to the rms error is approximately 2m, which means that the accuracy of the result is actually within the range of the reference.
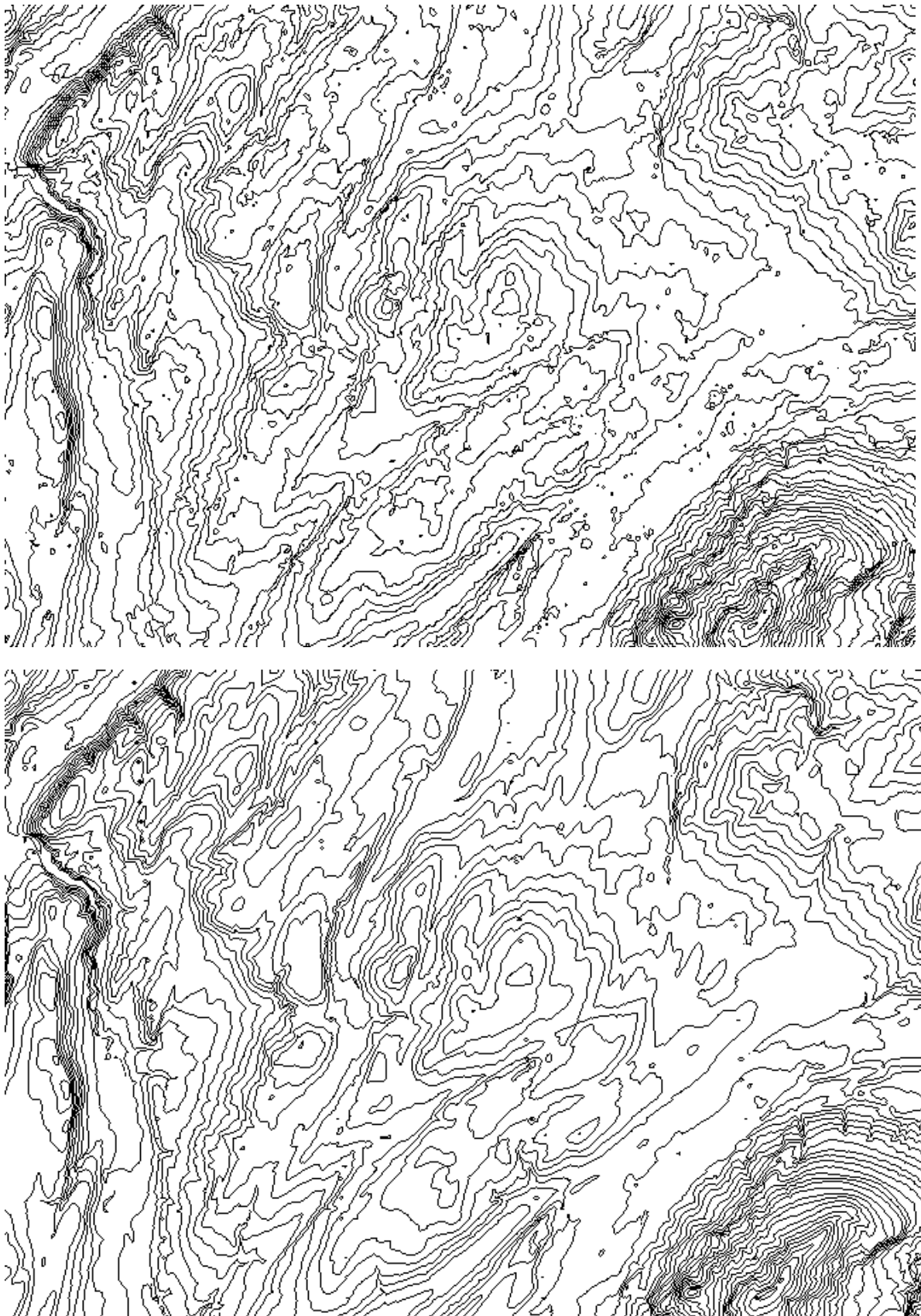
Fig. 6.9 Derived 20m contours of the fusion product (above) and the reference (below). The correspondence of the (unedited) product with the reference even in the steeper part indicates the measurement quality.

The 'bare soil' error assessment has been performed with help of the Swiss national Landsat orthomosaic (Fig. B2 (appendix)). The SPOT measurements approximated the coarse terrain shape rather well, which is indicated in the low mean of the fusion result. The number of extreme errors is much reduced in comparison to the initial measurements, especially those of SPOT. As expected, they occurred at the problematic regions of the site. A comparison of the contours of the reference an the unedited fused DTM are given in Fig. 6.9.

	SPOT	**ERS**	**Fused**
Σ posts	263'310	317'595	317'595
μ [m]	2.8	-3.6	-0.46
σ, rms [m]	11.1, 11.8	11.0, 11.7	6.3, 6.3
ΔH_{min} , ΔH_{max}	-132, 288	-79.4, 82	-43.6, 62.3
$\|\Delta H\| > 40m$ [%]	0.1	0.1	0

Tab. 6.4 Error statistics of the Swiss test site.

6.5 Results of the Test Site Spain II

6.5.1   Test site

The test site is located directly adjacent to the south of the Spain I site. It is situated within the Catalonian coastal chain, and consists of hilly and mostly of mountainous terrain (Fig. B3 (appendix)). The coastal chain stretches from southwest end of the site to the northeast end. The terrain morphology is mountainous, but not that steep like e.g. the Alps. The height difference between the minimal and maximal height is 1110m. The Ebro river, runs from north to south and passes the mountains in the scene center. The landscape is Mediterranean and rather dry in September, when images were taken. Only little agricultural landuse takes place in the northern and southern regions. Again, an area of approximately 950km^2 is covered.

6.5.2   ERS

The topography was hostile towards (ERS) InSAR DTM generation, the landcover favored it. Due to the climate, the 3-day repeat pass interval produced relatively high coherence (0.6) in the hilly part of the data set (Fig. 6.10a). The main problem posed of course the mountainous terrain, which covered most of the data set and separated the coherent parts in several unconnected subsets. Some coherent parts were trapped in the mountainous part, surrounded by extremely residue dense

regions. More than 23'000 residues remained in the scene *after* average filtering, which forced the branch cut unwrapping to leave large portions unwrapped (Fig. 6.10b). Although a separate unwrapping solution has been found for each coherent region, the resulting DTM patches have been of little use for enhancing the SPOT measurements. Hence, the interferogram simulation from the SPOT DTM served for connecting the regions and helped resolving as much terrain as possible (Fig. 6.10c). A detailed description of the processing is found in section 6.5.4.

After the fusion procedure, the InSAR DTM could be generated with very little interpolation. The results are given Tab. 6.5. Regarding the original problems with the site, the InSAR accuracy is rather high. The rms error reaches almost the SPOT result, although the error locations are different, due to the limited intervention during processing. However, most important is the fact that a complete DTM could be derived, which yielded redundant information for the final DTM fusion.

The baseline length in the center of the scene is 165m, which was in many cases too long to resolve the terrain. As reaction to the low quality of the propagated state vectors and the problem with the delivered control points, baseline has been computed from the DEOS state vectors and 6 control points were matched manually. The low coherence in the mountainous terrain hindered control point matching there.

The site has also been examined by other groups during the ORFEAS project (section C (appendix)). Phase flattening using the SPOT DTM has been tested for the ERS DTM. The result obtained by this procedure was a rms error of 12m in the InSAR DTM, after masking out all critical zones.

6.5.3   SPOT

The SPOT DTM processing has been described at the Spain I section. No clouds covered the Spanish sky in the late summer, when the images were taken. The results display the strength of photogrammetric DTM generation at this type of terrain. A complete DTM could be derived. Despite the topography, the mean and rms error of the DTM are 'normal' (Tab. 6.5). Typically, quite some outliers occurred randomly. Still, the error in the mountainous part is greater than in the hilly part of the site.

6.5.4   Fusion

Strategy The goal was to derive a DTM from ERS with support from SPOT, which could in turn be applied for enhancing the SPOT measurements. For that purpose, an interferogram has been simulated from the SPOT DTM, in order to handle those regions, which were without support inaccessible for the phase unwrapping. The baseline length favored the data fusion for phase unwrapping, as the ambiguity height is 55m and almost all SPOT measurements showed an error below that margin. Still, the simulations should only support the phase unwrapping procedure, but their interference with the InSAR generation process should be kept as little as possible in order to achieve InSAR information, which is to a great extent redundant.

Fusion during InSAR Processing

Alignment and Association The SPOT DTM has been converted to slant range and the heights to phases with the computed baseline model. After removal of the systematic ellipsoid contribution, an unwrapped solution was at hand. The unwrapping constant, due to the starting point of the InSAR phase unwrapping, has finally been removed in order to eliminate the bias between measurement and simulation. For the data association, the similarity declaration took advantage from the large ambiguity height. The gating value has been set to π, which means that practically all measurements were allowed to enter the fusion. Additional coherence checking avoided SPOT errors from entering the fusion process. Association was needed both for the detection and removal of atmospheric artifacts and for the phase reconstruction. As outlined in chapter 2, already small changes in the atmospheric conditions between the takes have great impact on short baseline measurements. Therefore, the relatively coarse gating value sufficed to detect those effects. The π gating reduced also the intervention of the simulation phase for restoration and unwrapping to an absolute minimum.

Atmospheric correction Deformations became visible after the removal of topographic fringes. The extent of the affected area was too large for leaving it out (Fig. 4.1). Although the flattening result was rather noisy, it could be unwrapped after some filtering. As also highly coherent areas have been affected, the polynomial approximation found enough points to generate a reasonable error surface, which was removed from the initial interferogram of the site (Fig. 4.2). This preprocessing is inevitable for the signal estimation during the unwrapping procedure, as additional fringes within the SAR interferogram would lead to estimation failure.
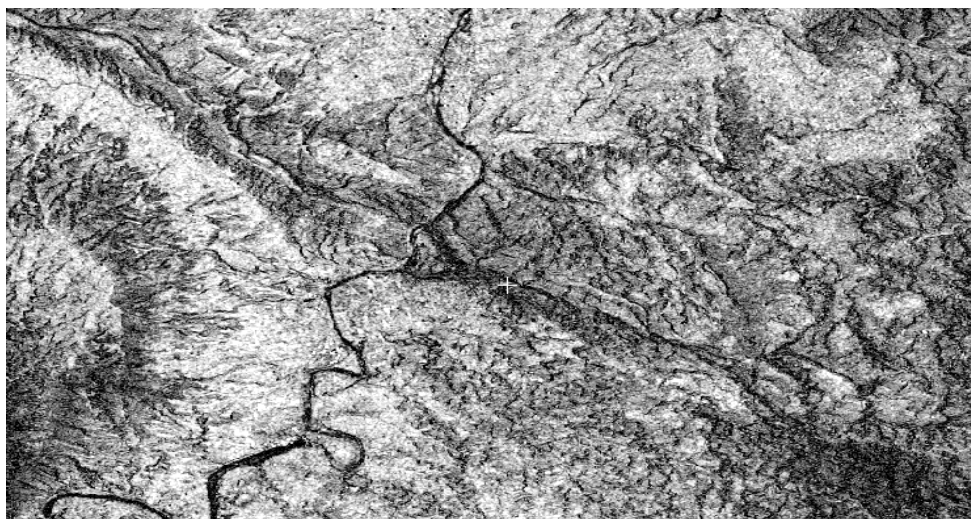
117

Fig. 6.10a Coherence at Spain II. Topography in connection with vegetation caused a coherence decrease all across the site.
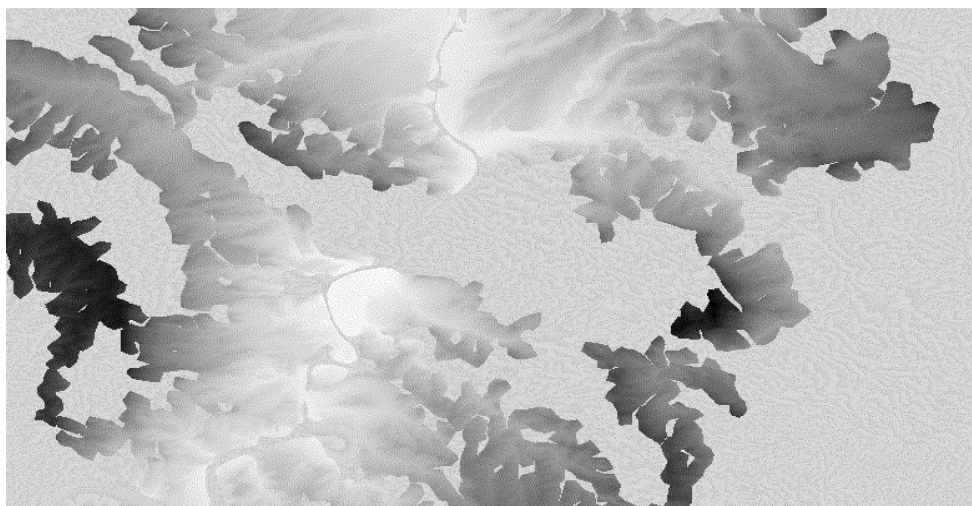

Fig. 6.10b Branch cut unwrapping result. Only the highly coherent parts could be unwrapped, the mountainous part remained inaccessible to a great extent.
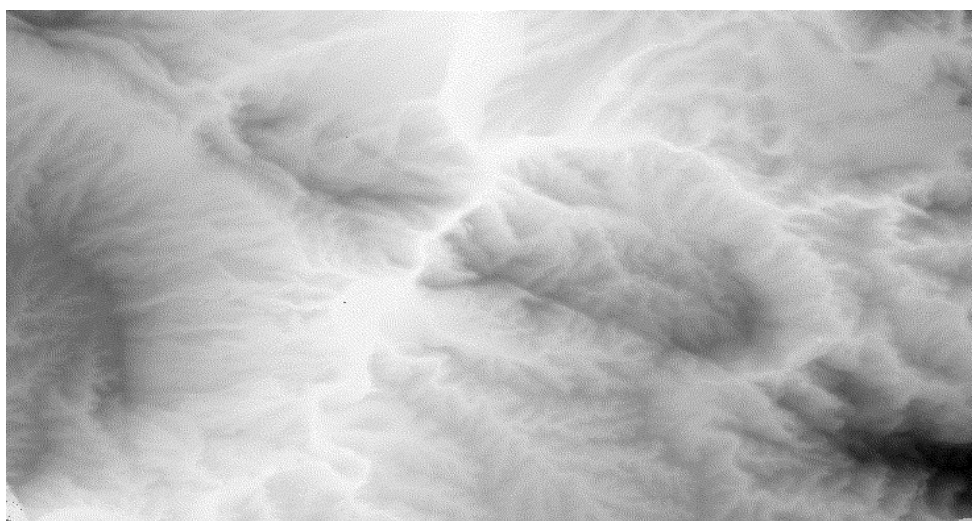

Fig. 6.10c Wiener unwrapping result after fusion. With support of the SPOT simulations, a complete unwrapping solution has been obtained. (See also Fig. 2.6)

Note that an erroneous simulation (e.g. due to insufficient baseline or measurement accuracy) would lead to a similar effect in the flattened interferogram. In fact, when applying the propagated state vectors for baseline modeling, two more residual (but in contrast regular!) fringes appeared after DTM flattening.

Wiener phase unwrapping Stand alone phase unwrapping was hardly feasible with the second Spanish site, due to foreshortening and layover effects in the coastal chain, which crossed through the scene. Due to the stable weather conditions between the takes, the effect of temporal decorrelation was only little. As the mountains were mostly wooded, the coherence decrease originated in most cases from a combination of spatial and volumetric decorrelation. As stated above, the topography is mountainous but not very steep, layover has been encountered, but to a much lesser extent than originally expected. The layover areas were indicated by their very low coherence, strong backscatter and from the simulation procedure and were left out for processing. The unwrapping was then performed with the Wiener method. The phase has been estimated adaptively, i.e. identifying automatically those areas, where the unwrapping algorithm was bound to fail. With the Wiener estimation method, an unwrapping solution could be derived for the whole scene. As the unwrapping has been performed automatically, no additional manual intervention was necessary. Some filtering examples contrasting the average filter with the Wiener solution are given in Fig. 6.11. The results of larger subsets are given in Fig. 6.12 and section B2 of the appendix.

The results of the Wiener phase restoration indicate the correctness of the proposed model. Both, averaging and Wiener filtering, reduce the random noise to a great extent. However, the assumption of only additive noise increases the problems after average filtering at those areas where the multiplicative corruption dominates. The erroneous additive noise model and filtering intensifies the fringe border corruption. Affected areas remain inaccessible for the phase unwrapping. The multiplicative effect occurred at this test site mainly due a combination of foreshortening and volumetric scattering. In fact, the fringes can be clearly discriminated at the Wiener results, indicating that the terrain is resolvable with the ERS viewing geometry. One concludes that these are not layover problems, thus the InSAR DTM will be able to contribute also to the SPOT DTM in the mountainous part. Fig. 6.12 illustrates the Wiener filtering capabilities at a larger subset. Again, the phase slope is very much preserved after filtering and the result is achieved completely automatically.
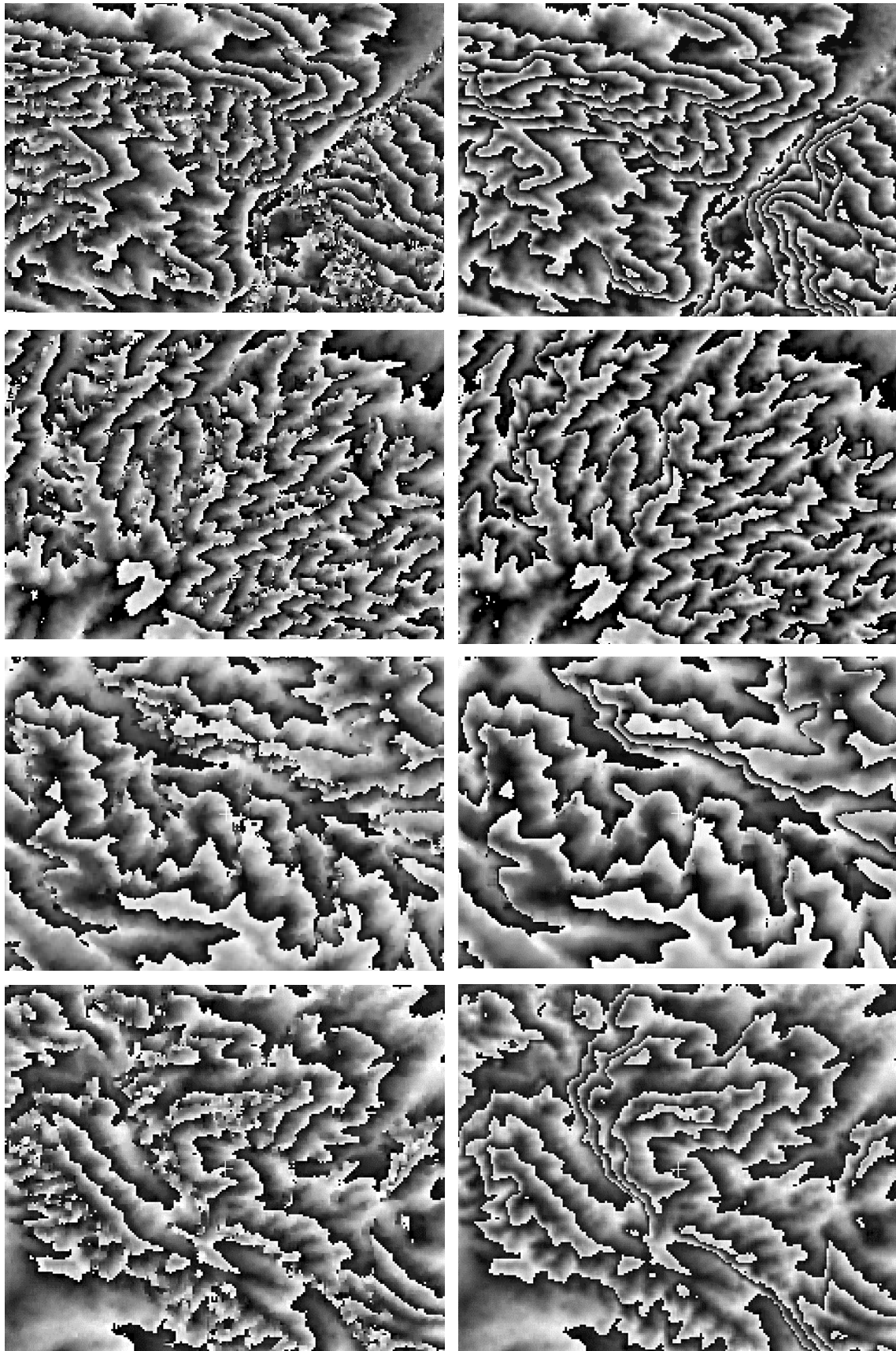
119

Fig. 6.11 Interferogram filtering results. **Left** column: averaging. The assumption of only additional noise led in part to extreme fringe border corruption. **Right** column: Wiener phase restoration of the same sites. The Wiener filter restored the shape even from extreme corruption by dealing with its additive and multiplicative part.
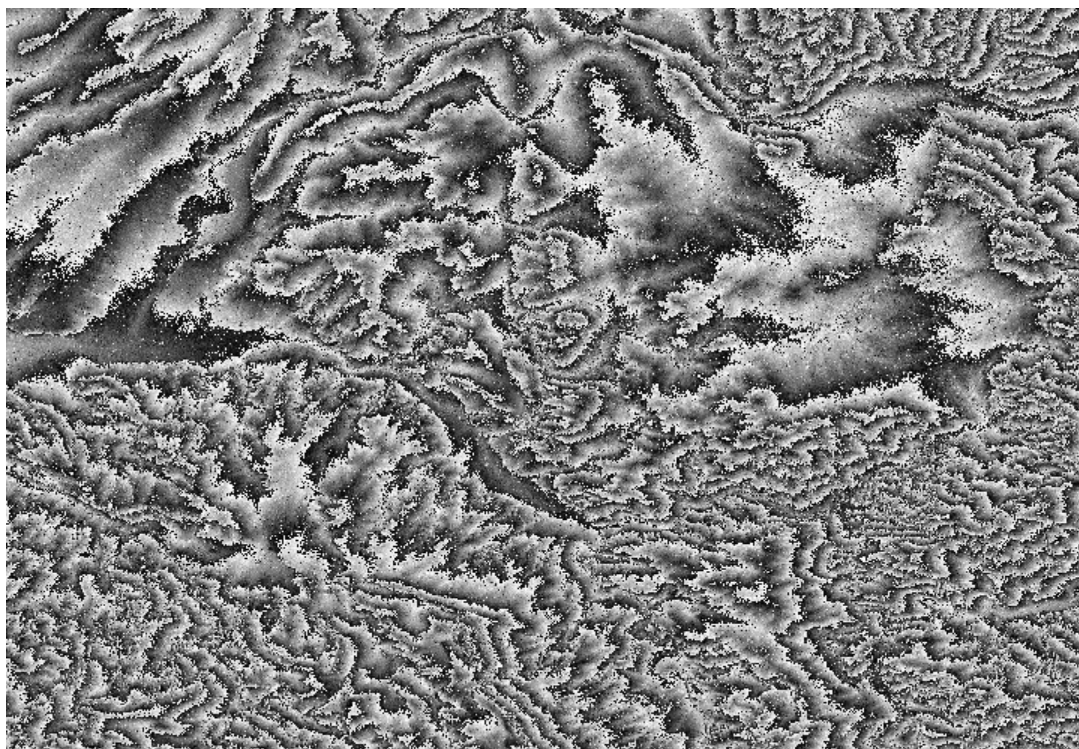
Fig. 6.12a The unfiltered interferogram of a subset of Spain II. A strong noise corruption is observed throughout the site. The steeper parts of the site (lower half of the image) forced for an information preserving filtering, as they were even worse affected, due to spatial decorrelation

Fig. 6.12b The (wrapped) result of the Wiener-based phase unwrapping. The whole site could be unwrapped with the Wiener method as the corruption has been treated correctly. Also the mountainous terrain is recovered and could successfully be used for the following DTM fusion. The SPOT DTM served only for constraining the unwrapping solution and for the computation of the parameters of the first (of four) Wiener filtering iteration.

DTM Fusion

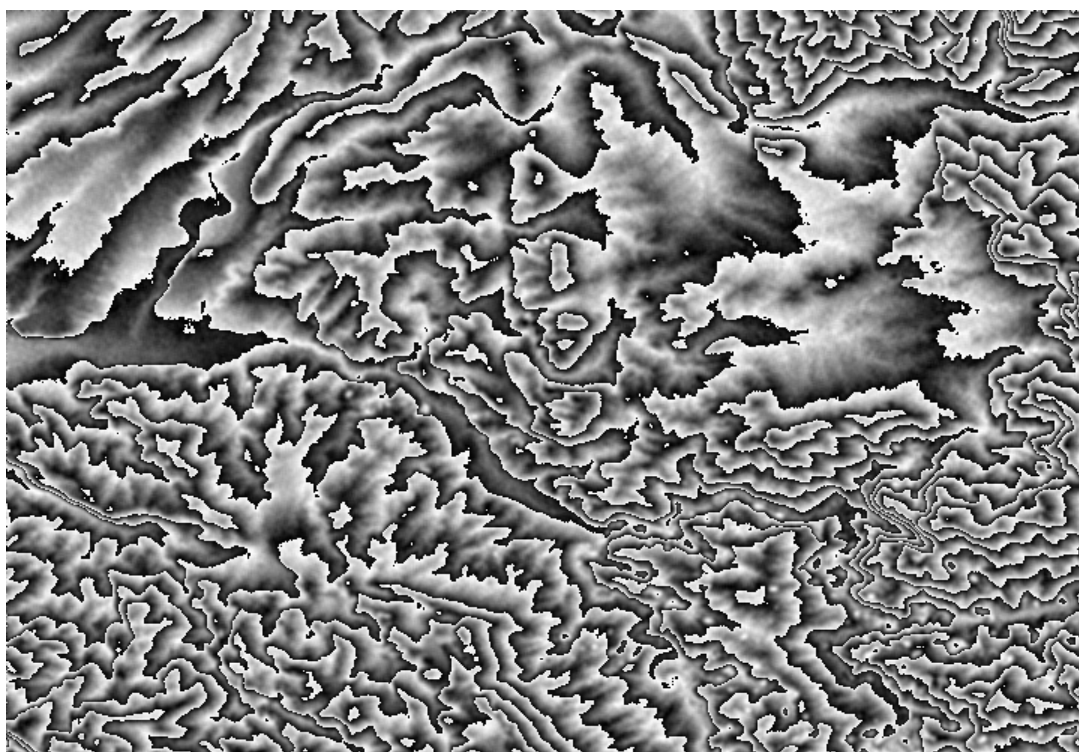**Association and Alignment** The DTMs were generated in the same 30m grid as the reference. Some planimetric adjustment has been performed in order to secure the point correspondence in the mountainous part of the site. The association procedure was the same as at the Spain I site, with a maximal permitted height difference of 20m, respecting the problematic terrain.

Fusion The DTMs have been fused using a local polynomial adjustment. Second and third order polynomials have been tested, yielding similar results. The fusion result is, much like the other cases, improved in all categories. The blunder reduction proves that the SPOT interference during the SAR DTM generation process was only little. The error is without editing around mapping standard for medium scales.

Although InSAR is expected to be only of limited use in such type of terrain, it is still capable to improve the SPOT measurements in practically all parts of the site. This improvement is visible, when one compares the SPOT stand-alone result (Fig. 6.13) with the fusion product (Fig. 6.14a, Fig. 6.14b). The error of practically all heights is less than 10m after the fusion. The result is clearly improved in the flatter regions, but the accuracy in the mountainous part also profited from the fusion. The applied thresholding for data association caused measurement losses along the slopes, where ERS failed. As the interpolation error depends on terrain shape and the extent of the gaps, direct interpolation was of little use to obtain a raster. The filling has instead been performed in the same way as at the Spain I site (section 6.3.5). In order to reduce the interpolation error mainly SPOT measurements in the mountainous region have been used. As an option, an additional InSAR DTM generated with images from the opposite viewing direction could be applied, which would increase the redundancy of the data and eases the decision, which sensor failed.

	SPOT	ERS	Fused	
			Similar points	Filled
Σ posts	642'730	642'730	414'442	642'730
μ [m]	1.6	0.1	1.3	1.5
σ, rms [m]	10.8, 10.9	13.2, 13.2	6.3, 6.5	7.5, 7.8
ΔH_{min} , ΔH_{max}	-153, 172	-192, 126	-65, 46.3	-67, 56.7
$|\Delta H| > 40m$ [%]	5.1	1.0	0	0.1

Tab. 6.5 Error statistics of the Spain II test site. The ERS results refer to the enhanced processing.
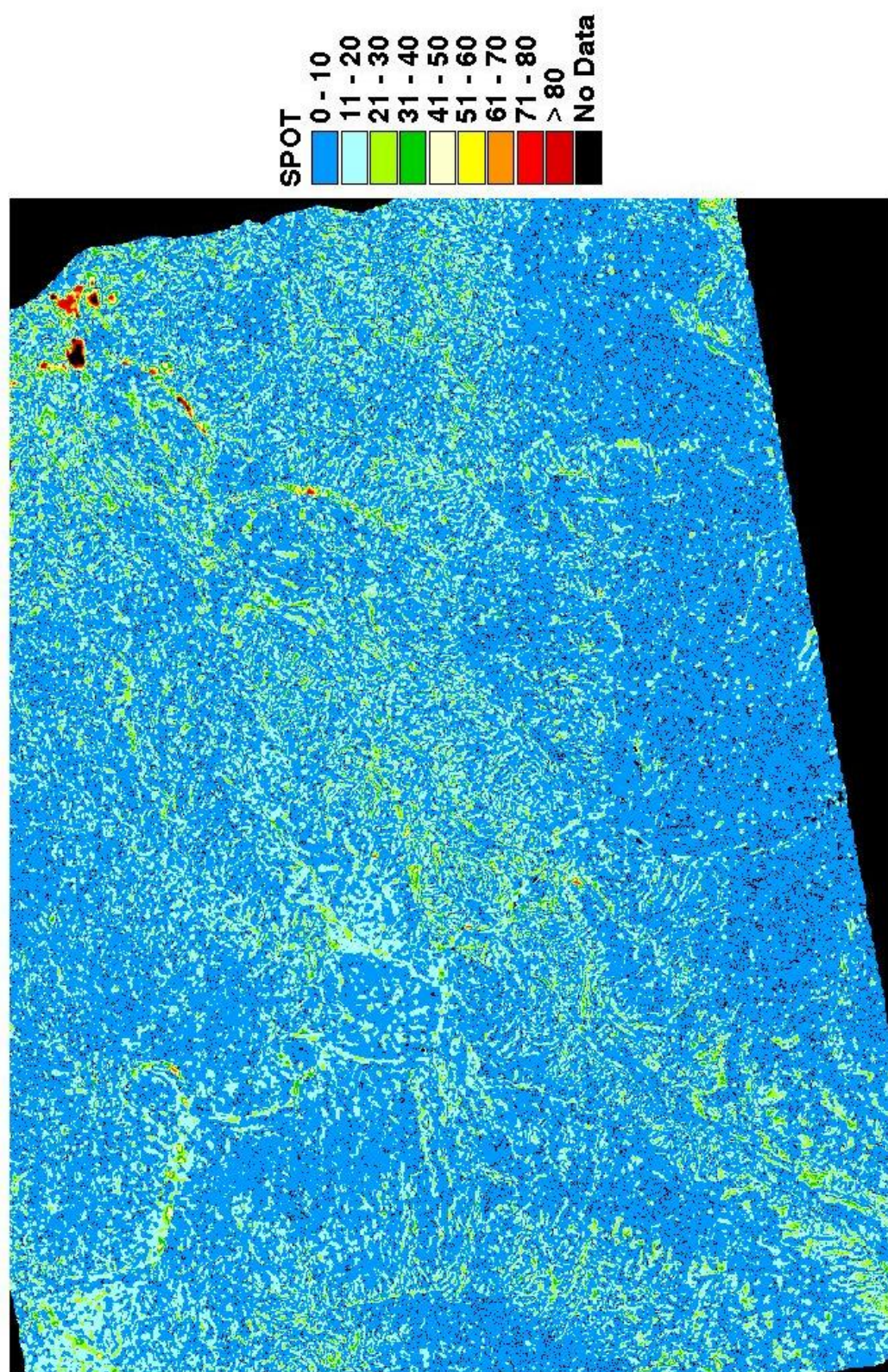
Fig. 6.13 Color-coded DTM difference (SPOT – reference). The vast majority of the differences is below 40m, most of them below 10m. The error is mainly randomly distributed, although most of the differences below 10m are found in the flatter part of the site, while the larger errors are concentrated along the river (which has not been edited) and in the mountainous part. The increase of errors in the mountainous part originates mostly from the raster interpolation.

123
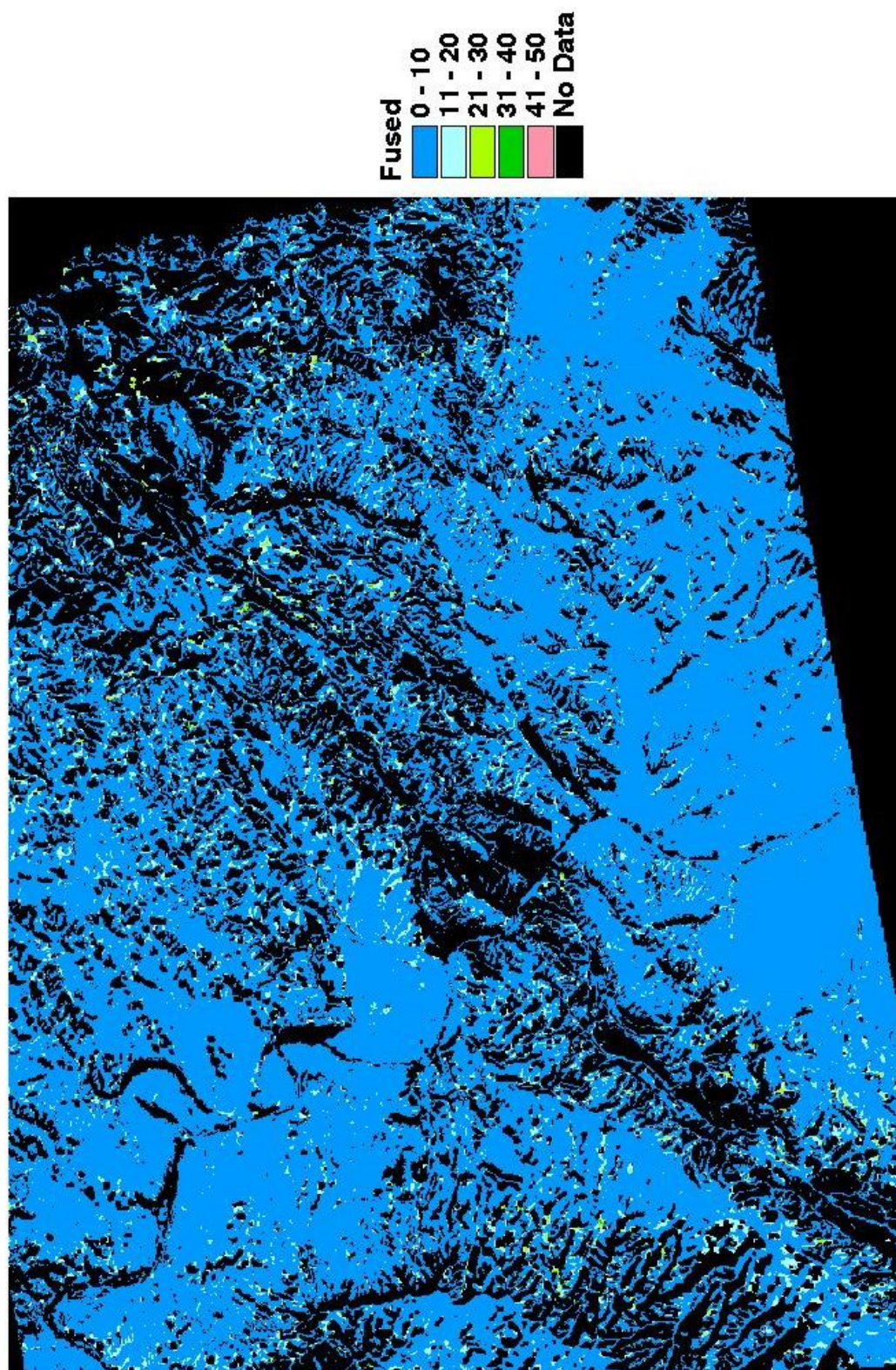
Fig. 6.14a Error of the fused DTM without interpolation. The vast majority of the differences in all parts of the site are below 10m. Outliers have been detected and removed. After the fusion with the InSAR measurements, the DTM improved mainly in respect to the random errors, which have been removed to a large extent. Also an improvement in the mountainous part is visible. Due to the strict decision logic for the similarity declaration ($\Delta H <$ |15m|) and as only a single InSAR DTM was available, some larger gaps remained after the fusion. The gaps are located at the mountain slopes, mostly due to InSAR measurement and geocoding inconsistencies.
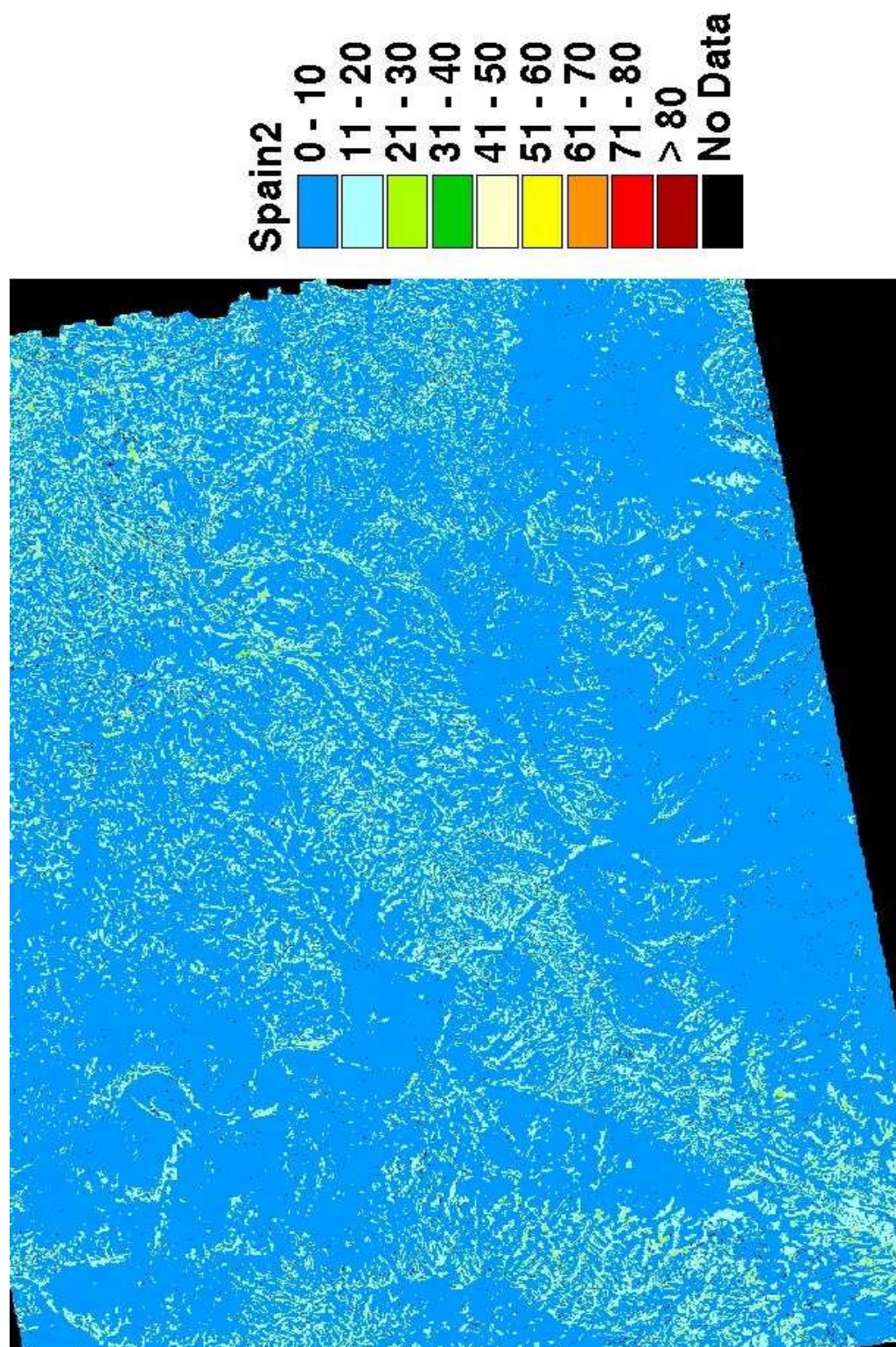
Fig. 6.14b Error of the fused DTM after filling with high quality points from each sensor and interpolation. Similarly to test site Spain I, the error in the filled areas is between 11 and 20m.. Only few larger errors emerged, mostly situated at steep slopes and along the Ebro river. The interpolation errors, which would otherwise occur especially in the mountainous part, could be reduced to a minimum in this way. The vegetation along the hillsides is certainly responsible for a good part of the error, as the fused DTM has been compared to a reference *elevation* model.

Quantitatively, the rms error decreases considerably in comparison to the sources and reaches sub-pixel accuracy. This decrease emphasizes that the synergy between InSAR and stereo-optical measurements is well exploited through the fusion approach even in demanding terrain. Most outliers are removed. But also approximately one third of the values has been rejected from the fusion. As mentioned above, the gaps mainly occurred in the mountainous region, the subsequent filling caused at the slopes an increase of the rms error. The total rms error rose to 7.8m after filling and raster interpolation. Again, landcover must to be taken into account, especially as the slopes are wooded. The rms error over sparsely vegetated terrain (including also parts of the mountains) has been determined to be 5.2m! One concludes that the method is able to deliver a product, which fulfills mapping standards also in complex terrain.

6.6 Summary

In this chapter, the data fusion concept and the proposed procedures have been tested. The results at the three test sites prove the synergy between a single ERS and SPOT DTM data. The effect of combining both DTM sources is a considerable increase of quality in all examined categories. Blunders are reliably detected with the association to the corresponding points of the counterpart. An improved representation of the terrain is achieved with the estimation of the height by taking advantage of the increase of redundant measurements. The observed systematic ERS corruption especially at the Spanish test sites could be eliminated with the SPOT DTM. The fused results came close to the quality of the reference data sets. The examined cases (normal quality SPOT and ERS, low quality of one with normal quality of the other source) cover the typical fusion scenarios in practice. Given two equivalent data sets, a very high DTM quality can be obtained. The rms error after fusion is below 5m over bare soil. With the frequency domain approach, the fused product reached with 3m the theoretical accuracy limit of InSAR. The use of ERS DTMs for improving the quality of existing SPOT data has been proved with the Swiss test site. A deficient SPOT DTM has been fused with an ERS tandem data set. Although topography and the quality of the existing data was rather problematic, the rms error of the fused result dropped by 50% in respect to the stand-alone results. All measurement gaps could be filled and a complete map sheet was derived. On the other hand, an existing SPOT DTM supported InSAR DTM generation, namely the derivation of a complete unwrapping solution at the very demanding second Spanish site. Wiener phase unwrapping has been extensively tested especially with this data set. The filtering results prove the correctness of the interferometric image model, which has been introduced in chapter 4. The

obtained InSAR DTM was in turn used in order to improve the SPOT measurements. The accuracy of the fused DTM was clearly higher than the stand-alone SPOT product.

C h a p t e r   7

SUMMARY, CONCLUSIONS AND OUTLOOK

7.1 Summary

The presented work aimed at the fusion of spaceborne SAR interferometric with stereo-optical DTM data. The measurement principles of both methods have been reviewed, the strengths and existing problems of each source have been pointed out. It has been concluded that the sensors and the techniques complement each other in respect to geometrical robustness and measurement density. The sensor model is more mature in the stereo optical case, which allows the direct relation between image and object coordinates and it is independent of the precision of the satellite state vectors on which SAR interferometry strongly depends. The advantages of InSAR are certainly the capability of the method to deliver a high measurement density almost automatically and the achievable measurement accuracy by exploiting the phase information.

The problem of fusing InSAR and stereo-optical DTMs is a special case of the general multi-sensor data fusion problem, dealing with the combination of redundant measurements of different sensors. The developed method takes advantage of the synergy of the sources and thus generates a product of superior quality. It consists of three main procedures, data alignment, association and estimation, which are subdivided in subprocedures. Alignment and association are essential preprocessing steps, relating the measurements to each other and sorting them according to their similarity, thus increasing the reliability of those entering the estimation process, which finally performs the combination of measurements. Two types of estimation are applicable for the discussed case: interpolation and prediction. While interpolation treats the individual sources

equally, prediction incorporates a priori knowledge, which makes this approach of special interest for data integration during the InSAR measurement process.

The fusion of existing measurements with interferometric phases has been demonstrated. After data alignment and association, atmospheric artifacts are reliably detected and removed even with a coarser DTM by computing the relationship between simulation and phase measurements in terms of coherence. The required DTM accuracy increases with the interferometric baseline length. Based on the model for optical imagery, an interferometric image model has been introduced, which covers both spatial decorrelation and random noise. It has been shown that the spectral shift between the ground reflectivity spectra, caused by spatial decorrelation, results in a local blur in the interferogram. The blurring and random noise are treated with the Wiener phase estimation during the unwrapping process. The Wiener estimator recovers the phases from the corruption and allows direct phase integration even in residue-dense regions. The error sensitive placing of branch cuts is completely avoided, if the unwrapping process is constrained with the SPOT DTM. Most important, only rough approximations derived from the stereo-optical DTM suffice for that procedure. The phase to height conversion is performed with the given DTM measurements by a polynomial approximation, respecting the crossing orbits of the two passes and reducing the baseline dependence of the InSAR DTM.

The three basic steps of the method have as well been performed in order to fuse InSAR and stereo-optical DTMs. Two options for height estimation in the spatial domain have been examined. The terrain is either approximated by a local polynomial, fit through all measurements, or by first removing the global trend from the measurements and afterwards performing a least squares interpolation of the relative heights. Both methods offer the option to combine the measurements and interpolate simultaneously. The polynomial approach being fast and efficient is useful for fusing DTMs of the same grid or supports the DTM interpolation from irregularly distributed points, while the least squares approach covers also the more general case of fusing dense InSAR with coarser stereo measurements. A new option for fusing the DTMs in the spatial frequency domain has also been proposed. It is a frequency domain realization of the least squares approach and aims at approximating the ideal transfer function by taking advantage of the complimentary error behavior of both sources. The less error affected low frequency band of the stereo-optical with the high frequency band of the InSAR DTM are combined.

The potential of the method and its procedures has been verified by fusing ERS with SPOT data at

three test sites in Spain and Switzerland. The sites comprised changing to mountainous terrain, posing considerable problems for both methods. The fusion options of combining DTMs of same grid and accuracy, combining ERS tandem measurements with a coarse SPOT DTM and the combination in mountainous terrain have been examined. InSAR processing profited from a priori knowledge in respect to the removal of atmospheric effects and the constrained phase unwrapping in problematic terrain, even when only a coarse terrain estimate was initially available. Several examples of the capabilities of the Wiener phase unwrapping have been presented. Even extremely corrupted phases could be reconstructed with that method. After the fusion of the DTMs, results with a root mean square error of 4 - 5m have been achieved even under problematic conditions, meaning a significant improvement of more than 50% in comparison to the stand-alone sources in all cases. The results also improved in respect to a decrease in mean and increase in reliability, as most outliers could reliably be detected and removed.

7.2 Conclusions

7.2.1   General

Data fusion permits the exploitation of the high accuracy potential of spaceborne stereo-optical and InSAR DTM data. When exploiting the proven data synergy between the sources, spaceborne InSAR height measurements are applicable to improve common stereo-optical DTM measurements. The InSAR technique in turn benefits during processing from existing height measurements, as the sensors and measurement techniques complement each other. Short baseline InSAR measurements are preferred for fusion with stereo-optical measurements, due to their moderate intervention and accuracy requirements during processing. The results indicate that high quality results are already achieved after the first iteration of the fusion procedure, which reduces the requirement of multiple baseline measurements in case of InSAR and the relatively high cost for new data in the SPOT case. Long baseline measurements, offering a higher accuracy potential, can optionally be applied in a second fusion cycle. The fusion result is a quantitatively (errors) and qualitatively (shape) improved DTM, reasonably applicable for follow up map products in the scale 1:50'000 or smaller.

7.2.2   DTM Integration during InSAR Processing

The InSAR measurement process profits strongly from almost any existing height measurements in order to overcome its sensitivity to noise and minimize systematic errors originating from baseline errors and atmospheric artifacts. Atmospheric artifacts have much stronger impact on short baseline measurements, but are there in turn easier to detect, permitting also the fusion scenario in

which only data of moderate accuracy and resolution are already available. The baseline dependency of the phase to height conversion and slant range to ground range conversion is avoidable with the existing measurements. Shorter baselines are also preferred for phase unwrapping in steeper terrain. As less fringes need to be unwrapped the need for intervention with existing measurements is much lower than with longer baselines. Due to the large ambiguity height, the accuracy requirements for fusing the existing data with a short baseline interferogram are comparatively low and are most likely to be matched with a SPOT DTM. The unwrapping problem is solvable, when an independent DTM is available. In respect to data synergy, a stereo-optical DTM is the source of choice, as the error mechanisms are differently. Hence, the Wiener parameters can reliably computed from that type of DTM.

7.2.3   InSAR and Stereo – Optical DTM Fusion

One concludes from the presented results that the fusion of stereo-optical and InSAR DTMs generates results of quality, which is hardly achievable with a single source data. It produces DTM results of better error statistics and shape as it increases the amount of valid measurements.

High quality results are achieved by fusing a single DTM of each source instead of using several DTMs from a single sensor source. The generated results indicate that high standards can operationally be matched with spaceborne data, offering a cost-effective opportunity to update databases especially in poorly mapped countries. As the DTM sources complement each other in respect to land cover (e.g. texture), form (e.g. terrain shape) and reasons of failure, data fusion produced improved results in all considered cases.

The major limitation of ERS is its inability to measure slopes larger than the viewing angle. A DTM improvement in steep terrain can therefore not be achieved with additional ERS scenes. SPOT stereo measurements are also error sensitive at slopes, but to a much lesser extent. As the ERS wavelength does not penetrate the vegetation, both techniques measure the surface height. A bias over e.g. forested areas has therefore to be taken into account after the fusion.

With the advent of systems having along track measurement capabilities (e.g. IKONOS), the issue of getting redundancy for spaceborne DTM generation is somewhat mitigated. Still, it has been shown that, by exploiting the InSAR and stereo-optical synergy, high quality results are achievable with fewer and less expensive data sets. If and how the sources complement each other in the aerial case remains to be examined.

132

7.3 Outlook

After a decade of boom triggered by the ERS mission, the SRTM marked the preliminary peak for spaceborne SAR interferometry for topographic mapping. The mission certainly benefited from the success of the ERS satellites. The ERS tandem mission ended only few weeks after, with the end of ERS-1. A series of new satellites with optical and SAR sensors is expected for the period of 2002/03. After its launch, planned for 2002, ENVISAT will take over the ERS mission. It is equipped, among other, with an improved SAR C-band instrument, which features full flexibility in the selection of polarization options and changeable viewing angle. ENVISAT will for the time being the last multi sensor, multi task mission. The trend is certainly shifting towards focussed, leaner missions, offering resolution in the scale of few meters. IKONOS-2, EROS and Quickbird demonstrate the potential of this new generation of sensors, spurring further missions of high resolution optical instruments. Among them, SPOT 5, scheduled for 2002, featuring 3m pixelsize and simultaneous stereoscopic image acquisition (along track). The lead of optical imagery in respect to resolution will be challenged by RADARSAT-2, which will deliver SAR imagery of 3m pixelsize in ultra fine mode. The resolution of SAR imagery will further increase, if the planned X-band missions (e.g. TerraSAR) are realized. Topographic mapping with SAR sensors will also profit from the X-band properties, which is more accurate (factor 2 - 3) than C-band.

DTM generation remains an issue for both high resolution SAR and optical missions. Radargrammetry benefits from the increase in SAR resolution, while interferometry remains the option of choice, especially for the expected L-band sensors (e.g. the planned Japanese ALOS mission) to come, which are more suitable for repeat pass SAR interferometry than ERS due to the longer wavelength, which is less change sensitive. The optical DTM generation is favored by the along track image acquisition capability of the new generation of sensors. With the experience gained from SPOT, the height accuracy of DTM generated with these sensors will be around pixel size. On the other hand, based on the experience with ERS, an accuracy of 1-3m can be achieved with a SAR pixelsize of 10m, which is within the reach of the coming missions. The results of the presented work indicate the synergy between the data, offering also the opportunity for fusion of high resolution data.

It has hardly been examined, how optical and SAR data sets can be combined in order to reduce the effect of vegetation on topographic measurements. E.g. forested terrain causes a bias in optical measurements. Longer SAR wavelengths, like L-band and P-Band, are able to penetrate the vegetation and measure the near surface response. On the other hand, the SAR resolution is lower

at those wavelengths. A fusion with high resolution optical DTMs would therefore be beneficial in respect to resolution and error.

The increase in resolution of spaceborne optical imagery offers another interesting option for data fusion. Airborne SAR imagery has approximately the same resolution but is much more cost effective (price/km^2) than current spaceborne high resolution optical imagery. Therefore, it may well serve as DTM source for orthoimage generation of newly acquired high resolution images. Moreover, as the accuracy of current airborne InSAR DTMs is similar to those of the high resolution spaceborne optical counterparts, the question arises, if some of the methods, presented in this work, are applicable for this case. Especially the fusion of vegetation penetrating L- and P-band DTMs with stereo-optical DTMs seems to be an interesting option. The examination of this type of fusion remains a topic for future research.

REFERENCES

ANGLERAUD C., BECEK, K., TRINDER, J. C., 1992. DEM determination from SPOT. Int. Archives of Photogrammetry and Remote Sensing, Vol. 29, Part B4, Comm. 4, pp. 969 -973

BALAN, P., 2000. The effect of baseline estimation on accuracy of interferometrically derived DEMs, Int. Archives of Photogrammetry and Remote Sensing, Vol. 33, Part B1 Comm. 1, pp. 29-36

BALTSAVIAS, E., 1991. Multiphoto geometrically constrained matching. Ph. D. thesis, Institut für Geodäsie und Photogrammetrie, ETH Zürich, Mitteilungen Nr. 49, 221p.

BALTSAVIAS, E., STALLMANN, D., 1992. Advancement in matching of SPOT images by integration of sensor geometry and treatment of radiometric differences. Int. Archives of Photogrammetry and Remote Sensing, Vol. 29, Part B4, Comm. 4, pp. 916 -924

BALTSAVIAS, E., STALLMANN, D., 1993. SPOT stereo matching for DTM generation. Proc. 2nd Swiss Symposium on Pattern Recognition and Computer Vision, pp. 61-72

BALTSAVIAS, E., 1999. Verfahren und Möglichkeiten der modernen Photogrammetrie zur DTM Generierung, Vortrag auf der Fachtagung "Digitale Geländemodelle: Technologie und Produkte", Zürich, Switzerland

BAMLER, R., HARTL, P., 1998. Synthetic aperture radar interferometry. Inverse Problems, Vol. 14, pp. R1 – 54

BUCHROITHNER, M., 1998. Geodata interrelations: Inventory and structuring attempt of taxonomic diversity. Proc. 2nd Int. Conf. Fusion of Earth Data, EARSeL SIG Data Fusion, Sophia Antipolis, France, pp. 11 - 15

BUNDESAMT FÜR LANDESTOPOGRAPHIE, 2001. Digitale Produkte: Höhenmodell DHM 25. http://www.swisstopo.ch/de/digital/dhm25.htm

CARRASCO, D., DIAZ, J., BROQUETAS, A., ET AL., 1997. Ascending descending orbit combination SAR interferometry assessment. Proc. 3rd ERS Symposium Florence, Italy. http://www.earth.esa.int/florence/participants/carrasco.html

CHEN, C., ZEBKER, H., 2001. Two dimensional phase unwrapping with use of statistical models for cost functions in nonlinear optimization. J. Opt. Soc. Am. A, vol. 18, No. 2, pp. 338 - 351

COSTANTINI, M., 1996. A novel phase unwrapping method based on network programming. IEEE Trans. Geoscience and Remote Sensing, vol. 36, pp. 813 –821

CROSSETTO, M., PEREZ, F., 1999. Radargrammetry and SAR interferometry for DEM generation: validation and data fusion. Proc. CEOS SAR workshop, CNES/ESA, http://www.estec.esa.nl/CONFANNOUN/99b02/index.html

CURLANDER, J. C., 1982. Location of spaceborne SAR imagery. IEEE Transactions on Geoscience and Remote Sensing Vol. 20 , No. 3, pp. 359-364

DARE, P., DOWMAN, I., 2000. A new approach to automatic feature base registration of SAR and SPOT images. Int. Archives of Photogrammetry and Remote Sensing, Vol. 33I, Part B2 Comm. 2, pp. 125-130

DAY, T., MÜLLER, J.P., 1988. Quality assessment of DEMs produced by automatic stereo matchers from SPOT image pairs. Int. Archives of Photogrammetry and Remote Sensing, Vol. 27, B3, pp. 148-159

DOWMAN, I., GUGAN, D., MULLER, J.-P., PEACEGOOD, G., 1987. The use of SPOT data for mapping and DEM production. SPOT 1 Utilisation des images, bilan, resultats. CNES Paris, France, pp. 1213-1220

DOWMAN, I., (ED.), 1991. Test of triangulation of SPOT data. European Organization for Experimental Photogrammetric Research, OEEPE Publication No. 26, 206p.

DURAND, D., 1995. Digital elevation models. Stereoscopic aspects of SPOT. Groupement pour le Développement de la Télédection Aérospatiale, http://ceos.cnes.fr:8100/cdrom-00/ceos1/science/science.htm

EARSeL, 1998. Definition developed by the EARSeL Special Interest Group (SIG) Data Fusion, Workshop in Sophia Antipolis, France

FELUS, Y., CSATHO, B., 2000. Multi-source DEM evaluation and integration at the Antarctica transantarctic mountains project. Int. Archives of Photogrammetry and Remote Sensing, Vol. 33I, Part B1 Comm. 1, pp. 117-123

FERRETTI, A., MONTI GUARNIERI, A., PRATI, C., ROCCA, F., 1997. Multi-baseline SAR interferometry for automatic DEM reconstruction. Proc. 3rd ERS Symposium, Florence, Italy, http://www.earth.esa.int/florence/participants/ferretti.html

FERRETTI, A., PRATI, C., ROCCA, F., 1999. Multibaseline InSAR DEM reconstruction: The wavelet approach. IEEE Transactions on Geoscience and Remote Sensing vol. 37, I 2 Part 1, pp. 705-715

FÖRSTNER, W., 1986. A feature based correspondence algorithm for image matching and least squares matching. Int. Archives of Photogrammetry and Remote Sensing, Vol. 26, part 3, pp. 150-166

FÖRSTNER, W., 2000. Image preprocessing for feature extraction in digital intensity, color and range images. In: Dermanis, Grün, Sanso (ed.'s): Geomatic methods for the analysis of data in earth sciences. Lecture notes in earth sciences No. 95, Springer Verlag, Berlin, pp.165-189

FORSTER, B., TRINDER, J.C., FARRINGTON, R., 1987. Mapping and urban multi-experimental assessment of SPOT – Mapping results. Colloque SPOT 1. Image utilization, assessment, results. Paris, France, pp. 1289 – 1296

FRASER, C., BALTSAVIAS, E., GRÜN, A., 2001. IKONOS Geo Images: Geometric potential and suitability for building reconstruction. Proc. DGPF Jahrestagung 2001: Geodaten schaffen Verbindungen, Konstanz, Germany, on CD

GABRIEL, A., GOLDSTEIN, R., 1988. Crossed orbit interferometry: Theory and experimental results from SIR-B. Int. Journal of Remote Sensing, Vol. 9, No. 5, pp. 857 – 872

GATELLI, F., MONTE GUARNIERI, A., PARIZZI, F., ET AL., 1994. The wavenumber shift in SAR interferometry. IEEE Trans. Geoscience and Remote Sensing, Vol 32, pp. 855 – 865

GENS, R., 1998. Quality assessment of SAR interferometric data. PhD. Thesis, ITC Publication No. 61, 141 p.

GEUDTNER, D., SCHWÄBISCH, M., 1996. An algorithm for precise reconstruction of InSAR imaging geometry: Application to flat earth phase removal, phase-to-height conversion and geocoding of InSAR derived DEMs. Proc. EUSAR Königswinter, Germany, pp. 249 -252

GHIGLIA, D., ROMERO, C., 1989. Direct phase estimation from phase differences using fast elliptic partial differential equation solvers. Opt. Lett., Vol. 15, pp. 1107 - 1109

GHIGLIA, D., ROMERO, C., 1994. Robust two-dimensional weighted and unweighted phase unwrapping that uses fast transforms and iterative methods. J. Opt. Soc. Am., Vol. 11, No. 1, pp. 107-117

GOLDSTEIN, R., ZEBKER H., WERNER C., 1988. Satellite Radar Interferometry: Two dimensional phase unwrapping. Radio Science, Vol. 23, No.4, pp. 713-720

GOLDSTEIN, R., 1995. Atmospheric limitations to repeat track radar interferometry. Geophysical Research Letters, vol.22, no. 18, pp. 2517-2520

GONCALVES, J., DOWMAN, I., 2001. Use of mixed SAR-SPOT pairs for topographic mapping. Proc. of Conference of Remote Sensing and Photogrammetry Society, London, UK, on CD

GRAHAM, L., 1974. Synthetic interferometer radar for topographic mapping. Proc. IEEE, Vol. 62, pp. 763 - 768

GRÜN, A., 1985. Adaptive least squares correlation: a powerful image matching technique. South African Journal of Photogrammetry, Remote Sensing and Cartography, Vol. 14, No. 3, pp. 175 – 187

GRÜN, A., 1986a. Photogrammetrische Punktbestimmung mit der Bündelmethode. Institut f. Geodäsie und Photogrammetrie, ETH Zürich, Mitteilungen Nr. 40, 87 p.

GRÜN, A., 1986b. High precision image matching for digital terrain model generation. Int. Archives of Photogrammetry and Remote Sensing, Vol. 26(3/1), pp. 284-296

GUIDON, B., ADAIR, M., 1992. Analytic formulation of spaceborne SAR image geocoding and "value added" product generation procedure using digital elevation data. Canadian Journal of Remote Sensing, Vol. 18, pp. 2 - 11

HAGBERG, J., ULANDER L., 1993. On the optimization of interferometric SAR for topographic mapping. IEEE Transactions on Geoscience and Remote Sensing, Vol. 31, No. 1, pp. 303 - 306

HALL, D., 1992. Mathematical techniques in multisensor data fusion. Artech House Inc., Boston, 1st ed, 295 p.

HARTL, P., 1991. Application of interferometric SAR data of the ERS-1 mission for high resolution topographic terrain mapping. GIS 2/91, pp. 8 – 19.

HENDERSON, F., LEWIS, A., (ed.) 1999. Principles & applications of imaging Radars. Manual of remote sensing, J. Wiley & Sons Inc. N.Y., 3rd edition, Vol. 2, 866 p.

HONIKEL, M., 1998. Fusion of optical and Radar digital elevation models in the spatial frequency domain, Proc. 2nd Int. Workshop on Retrieval of Bio- and Geophysical Parameters from SAR Data for Land Applications, pp. 537-543

HONIKEL, M., 1999. Data fusion strategies for the fusion of InSAR and stereo-optical DEMs, Int. Archives of Photogrammetry and Remote Sensing, Vol. 32, Part 7-4-3 W6, pp. 83-89

HONIKEL, M., 2000. Wiener-based interferometric signature reconstruction. Int. Archives of Photogrammetry and Remote Sensing, Vol. 33I, Part B1 Comm. 1, pp. 148-155

KALMAN, R., 1960. A new approach to linear filtering and prediction problems. Transactions of the ASME, Journal of basic engineering, pp. 35 – 45

KIM, T., 2000. A study on the epipolarity of linear pushbroom images. Photogrammetric Engineering and Remote Sensing, Vol. 66, No. 8, pp. 961 - 966

KOCH, K., 1980. Parameterschätzung und Hypotesentests in linearen Modellen. Dümmler Verlag, Bonn, 270 p.

KONECNY, G., LOHMANN, P., ENGEL, H., KRUCK, E., 1987. Evaluation of SPOT imagery on analytical photogrammetric instruments. Photogrammetric Engineering and Remote Sensing, Vol. 53, No. 9, pp. 1223 -1230

KORNUS, W., LEHNER, M., SCHRÖDER M., 2000. Geometric in-flight calibration of the stereoscopic line CCD scanner MOMS-2P. ISPRS Journal of Photogrammetry and Remote Sensing, Vol. 55, N 1, pp. 59-71

KRATKY, V., 1989. Rigorous photogrammetric processing of SPOT images at CCM Canada, ISPRS Journal of Photogrammetry and Remote Sensing, Vol. 44, pp. 53 – 71

KRAUS, K., 1973. Ein allgemeines digitales Geländemodell – Theorie und Anwendungen. From F. Ackermann: Numerische Photogrammetrie, Sammlung Wichmann, Neue Folge, Band 5, H. Wichmann Verlag Karlsruhe, p. 225-254

KRAUS, K., 1982. Photogrammetrie Band 1: Grundzüge der Photogrammetrie. Dümmler Verlag, Köln, p. A 2.7-1

KRAUS, K., 2000. Photogrammetrie Band 3: Topographische Informationssysteme. H 3, Dümmler Verlag, Köln, 409 p.

LEBERL, F., 1999. Radargrammetry. In (Henderson, 1999), Chapter 4, pp. 183 – 268

LI, D., CHENG, J., 1988. Bundle adjustment of SPOT imagery. Proc. XVI Congress ISPRS, Kyoto, Japan, Vol. B3, pp. 449 - 455

MADSEN, S., ZEBKER, H., 1999. Imaging Radar Interferometry. In (Henderson, 1999), Chapter 6, pp. 359 – 380

MASSMANN, F., REIGBER, C., KÖNIG, R., et al., 1993. ERS-1 orbit information provided by D-PAF. Proc. 2nd ERS-1 Symposium, Hamburg, pp. 765 – 770.

MASSONNET, D., VADON, H., ROSSI, M., 1996. Reduction of the need for phase unwrapping in Radar interferometry. IEEE Transactions on Geoscience and Remote Sensing Vol. 37, No. 2, pp. 489 – 497

MIKHAIL, E. M., 1976. Observations and least squares. IEP-A Dun-Donnelley Publisher, New York, 1st ed., p. 393

MORLEY, J., WALKER, A., MULLER, J. P., et al., 2000. Landmap: Creating a DEM for the British isles by SAR interferometry. Int. Archives of Photogrammetry and Remote Sensing, Vol. 33I, Part B4b Comm. 4, pp. 686 - 693

PATIAS, P. (ed.), 1998. ORFEAS, Optical Radar Sensor Fusion for Environmental Applications, Final EU Project Report, Contract no. ENV4-CT95-0150, 169p.

PERLANT, F., 1992. Example of SPOT/ERS-1 complementarity, Proc. First ERS-1 Symposium – Space at the service of our environment, Cannes, France, pp. 563-568

PRATI, C., GIANI, M., LEURATTI, N., 1992. SAR interferometry: A 2D phase unwrapping procedure based on phase and absolute values information. Proc. IGARSS Washington DC, USA, pp. 2043 - 2046

PRATI, C., ROCCA, F., MONTI-GUARNIERI, A., PASQUALI, P., 1994. ERS-1 Interferometric Techniques and Applications, ISPRS Proc. of Primary Data Acquisition and Evaluation, 30(1), pp. 123-126

PRATT, W. K., 1991. Digital image processing. John Wiley & Sons New York, 2nd ed., pp. 384 - 385.

RENAUDIN, E., 2000. Evaluation of DEMs from SAR interferometry and SPOT stereoscopy for remote sensing applications. Diploma thesis, Institut f. Geodäsie und Photogrammetrie, ETH Zürich, 54p.

RENOUARD, L., PERLANT, F., 1993. Geocoding SPOT products with ERS-1 SAR geometry. Proc. 2nd ERS-1 Symposium - Space at the service of our environment, Hamburg, Germany, pp. 653 - 658.

RENOUARD, L., PERLANT, F., NONIN, P., 1995. Comparison of DEM generation from SPOT stereo and ERS interferometric SAR data, EARSeL advances in remote sensing, proc. Topography from Space, Göteborg, Sweden, Vol. 4, No. 2, pp. 103 – 109

RODRIGUEZ, E., MARTIN, J., 1992. Theory and design of interferometric synthetic aperture radars. IEE Proceedings, Vol. 139, No. 2, pp. 147 – 159

ROGERS, D., SENUS, W., HENNIG, T., 2001. Global terrain mapping with shuttle radar topography mission (SRTM). Proceedings ISPRS WG II/2 Workshop on Three dimensional mapping from InSAR and Lidar, Banff, Canada, on CD.

ROSEN, P., HENSLEY, S., JOUGHIN, I., et al., 2000. Synthetic Aperture Radar Interferometry. Proc. IEEE, Vol. 88, No. 3, pp. 333 - 382

SCHARROO, R., VISSER, P., METS, G., 1998. Precise orbit determination and gravity field improvement for the ERS satellites. Journal for Geophysical Research, 103, C4, pp. 8113-8127

SCHUT, G. H., 1976. Review of interpolation methods for digital terrain models. Invited paper 13 ISP Congress, Helsinki, Finland, 23 p.

SMALL, D., WERNER, C., NÜESCH, D., 1995. Geocoding and validation of ERS-1 InSAR-derived digital elevation models. EARSeL advances in remote sensing, Proc. Topography from Space, Göteborg, Sweden, Vol. 4, No. 2 , pp. 26 – 39

SMALL, D., PRATI, P., FLÜGLISTALER, S., 1996. A comparison of phase to height conversion methods for SAR interferometry. Proc. IGARSS Lincoln, USA, pp. 342 - 344

SMALL, D., 1998. Generation of DEMs through spaceborne SAR interferometry. Ph.D. Thesis, Remote Sensing Laboratories, Univ. of Zurich, Remote Sensing Series Vol. 30, 143 p.

TANNOUS, I., LE GOFF, F., PENICAND, C., 1996. Fusion of ERS 3D information for DEM generation. Proc. Fusion of Earth Data, Cannes France, pp. 45 –51

TEGUH, H., 1994. Untersuchungen zur Stereoauswertung von SPOT-Satellitenaufnahmen mit Hilfe der digitalen Bildverarbeitung. Dissertation, Wissenschaftliche Arbeiten der Fachrichtung Vemessungswesen der Universität Hannover, Nr. 206, 69 p.

TEMPFLI, K., 1982. Genauigkeitsschätzung digitaler Höhenmodelle mittels Spektralanalyse. Geowissenschaftliche Mitteilungen, Heft 22, 102 p.

THEODOSSIOU, E., DOWMAN, I., 1990. Heighting accuracy of SPOT. PERS, Vol. 56, No. 12, pp. 1643-1649

TOUTIN, T., 1985. Analyse mathematique des possibilites cartographiques du systeme SPOT. PhD Thesis, Ecole Nationale des Sciences Geographique, Paris, 163 p.

TOUTIN, T., 1995. Multisource data fusion with an integrated unified modeling. EARSeL advances in remote sensing, Proc. Topography from Space, Göteborg, Sweden, Vol. 4, N 2 , pp. 118 – 129

TOUTIN, T., 2001. Block adjustment of Landsat-7 ETM images. Proc. Joint ISPRS WG I/2, I/5 and IV/7 Workshop, High resolution mapping from space, Institute for Photogrammetry and Geoinformation, University Hannover, Germany, on CD

ULANDER, L., DAMMERT, P., HAGBERG, J., 1995. Measuring tree heights with SAR interferometry. IEEE Transactions on Geoscience and Remote Sensing, Vol. 33, No. 3, pp. 2189 – 2191

U.S. DEPARTMENT OF DEFENSE, 1991. Data Fusion definition developed by the Data Fusion Subpanel of Joint Directors of Laboratories, Technical panel of C^3 , Data fusion lexicon.

U.S. DEPARTMENT OF THE INTERIOR, 1992. Standards for digital elevation models. National Mapping Program, Technical Instructions, Part 2, Specifications, http://www.charttiff.com/pub/standard/dem/2DEM0198.PDF

VASS, P., BATTRICK, B., (ed.), 1992. ESA Product Specification. 1. Synthetic Aperture Radar image mode. ESA publication division, ESTEC, Noordwijk, pp. 1-6 – 1-11

VEILLET, I., 1990. Block adjustment of SPOT images for large area topographic mapping. Int. Archives of Photogrammetry and Remote Sensing, Vol. 29, Part 3/2, pp. 926 – 935

VEILLET, I., 1992. Accuracy of SPOT triangulation with very few or no ground control point. Int. Archives of Photogrammetry and Remote Sensing, Vol. 27, Part B4, Comm. 4, pp. 448-450

WALD, T., 1998. Data fusion: a conceptual approach for an efficient exploitation of remote sensing images. Proc. 2nd Int. Conf. Fusion of Earth Data, EARSeL SIG Data Fusion, Sophia Antipolis, France, pp. 17 – 23

WALD, T., 1999. Definitions and terms of reference in data fusion. Int. Archives of Photogrammetry and Remote Sensing, Vol. 32, Part 7-4-3 W6, pp. 2 - 6

WALTZ, E., LLINAS, J., 1990. Multisensor data fusion. Artech House Inc., Boston, 1st ed., 464 p.

WEGMÜLLER, U., WERNER C., 1995. SAR interferometric signatures of forest. IEEE Geoscience and Remote Sensing, Vol. 33, No. 5, pp. 1153-1161.

WEIDNER, U, 1994. Information preserving surface restoration and feature extraction for DEMs. Proc. ISPRS Com. III symposium on spatial information from digital photogrammetry and computer vision, SPIE, pp. 908-915

WERNER, C., 1992. Techniques and applications of SAR interferometry for ERS-1: Topographic mapping, change detection and slope measurement. Proc. 1st ERS-1 Symposium, Space at the Service of our Environment, pp. 205-210

WIESMANN, A., RIBBES F., HONIKEL M., et al., 2001. Forest storm damage assessment with ERS Tandem data. Submitted to Int. Journal of Remote Sensing.

XIA, Y., 1996. Bestimmung geodynamischer Effekte mit Hilfe der Radarinterferometrie. DGK, Reihe C, Dissertationen, Heft Nr. 467, 88p.

ZEBKER, H., GOLDSTEIN, R., 1986. Topographic mapping from interferometric SAR observations. Journal of Geophysical Research, Vol. 91, B5, pp. 4993-4999

ZEBKER, H., VILLASENOR, J., 1992. Decorrelation in interferometric radar echoes. IEEE Transactions on Geoscience and Remote Sensing, Vol. 30, No. 5, pp. 950 - 959

ZEBKER, H., WERNER, C., ROSEN, P., 1994. Accuracy of topographic maps derived from ERS-1 interferometric Radar, IEEE Transactions on Geoscience and Remote Sensing, 32(4), pp. 823-836

ZEBKER, H., ROSEN, P., HENSLEY, S., 1997. Atmospheric artifacts in interferometric SAR surface deformation and topographic maps, Journal Geophys. Res., Solid Earth, Vol. 102, 7547 - 7563

ZEBKER, H., LU, Y., 1998, Phase unwrapping algorithms for radar interferometry: residue cut, least squares and synthesis algorithms, Journal of the optical society of America A, Vol. 15, I 3, pp. 586-598

144

APPENDIX

A Symbols

(N, E, H)	DTM coordinates
(r, a)	Range, azimuth SAR image coordinates
(u, v)	Fourier transformed image coordinates
(X, Y, Z)	Coordinates in the ECR system
(x, y)	Image coordinates
A	Coefficient matrix
A	Amplitude
a	Semi major ellipsoid axis
B	Degradation matrix
B	Baseline magnitude
$B_\perp$	Perpendicular baseline component
$B_{||}$	Parallel baseline component
$\underline{b}$	Bias vector
b	Semi minor ellipsoid axis
$\underline{e}$	Error vector
$\underline{f}$	Uncorrupted measurements
f_o	Central SAR frequency
f_p	Doppler frequency
$\mathbf{g}$	Observation vector
H	DTM height
H_S	Satellite altitude
$h_{2\pi}$	Ambiguity height
h	Height above ellipsoid
I	Identity matrix
$\mathbf{K_{gg}}$	Auto-covariance matrix
$\mathbf{K_{fg}}$	Cross-covariance matrix
k	Wavenumber

A2

k_{gr}	Ground range wavenumber projection
$\mathbf{N}$	Coefficient matrix
$\underline{n}$	Noise vector
$\mathbf{P}$	Weight matrix
$\underline{P}$	Point vector
prf	Pulse repetition frequency
$\mathbf{R}$	Rotation matrix
R	Range distance satellite target
$\underline{r}$	Random error vector
r	Redundancy
r_r	Slant range pixel size
r_g	Ground range pixel size
S	Satellite position
$\underline{s}$	Terrain microstructure
SNR	Signal to noise ratio
$\underline{v}$	Residual vector or elevation vector relative to the trend
v_c	Speed of light
$\mathbf{W}$	Deconvolution matrix
W	Bandwidth
$\underline{X}_o$	Projection center position
α	Terrain slope angle
ε	Phase constraint distance
ϕ	Interferometric phase
ϕ_{abs}	Absolute phase
ϕ_{atm}	Atmospheric phase contribution
ϕ_d	DTM flattened phase
ϕ_{ell}	Ellipsoid phase contribution
ϕ_{sim}	Simulated phase
ϕ_{unw}	Unwrapped phase
γ	Coherence
φ	Target phase

κ	Scale
λ	Wavelength
μ	Mean error
θ	Angle of incidence
ρ	Correlation coefficient
σ	Error
ω_o	Cut-off frequency

B Test Data Sets

B 1 Data Sets

Test site 1: Spain 1		
Sensor	**ERS-1**	**SPOT**
Data, raw pixelsize	Single look complex, 20x4m	PAN, 10m
Scene	Orbit 829 / 872, Frame 819	42 - 267
Date	12. / 15. September1991	3. / 7. September 1986
Baseline / B/H	150m	1
Area (km^2)	30 x 25 km^2	30 x 25 km^2

Test site 2: Swiss 1:25'000 Map sheet 1224		
Sensor	**ERS-1 / 2**	**SPOT**
Data, raw pixelsize	Single look complex, 20x4m	PAN, 10m
Scene	Orbit 22326/2653, Frame 294	51 - 256
Date	26., 27. October 1995	20. July, 27. August 1988
Baseline / B/H	106m	0.8
Area (km^2)	12 x 10 km^2	12 x 10 km^2

Test site 3: Spain 2		
Sensor	**ERS-1**	**SPOT**
Data, raw pixelsize	Single look complex, 20x4m	PAN, 10m
Scene	Orbit 829 / 872, Frame 819	42 - 267
Date	9., 12. September 1991	3., 7. September 1986
Baseline / B/H	150m	1
Area (km^2)	30 x 25 km^2	30 x 25 km^2

Fig. B1 Site Spain I, DTM and topographic map 1:250'000 © Institut Cartographic de Catalunya
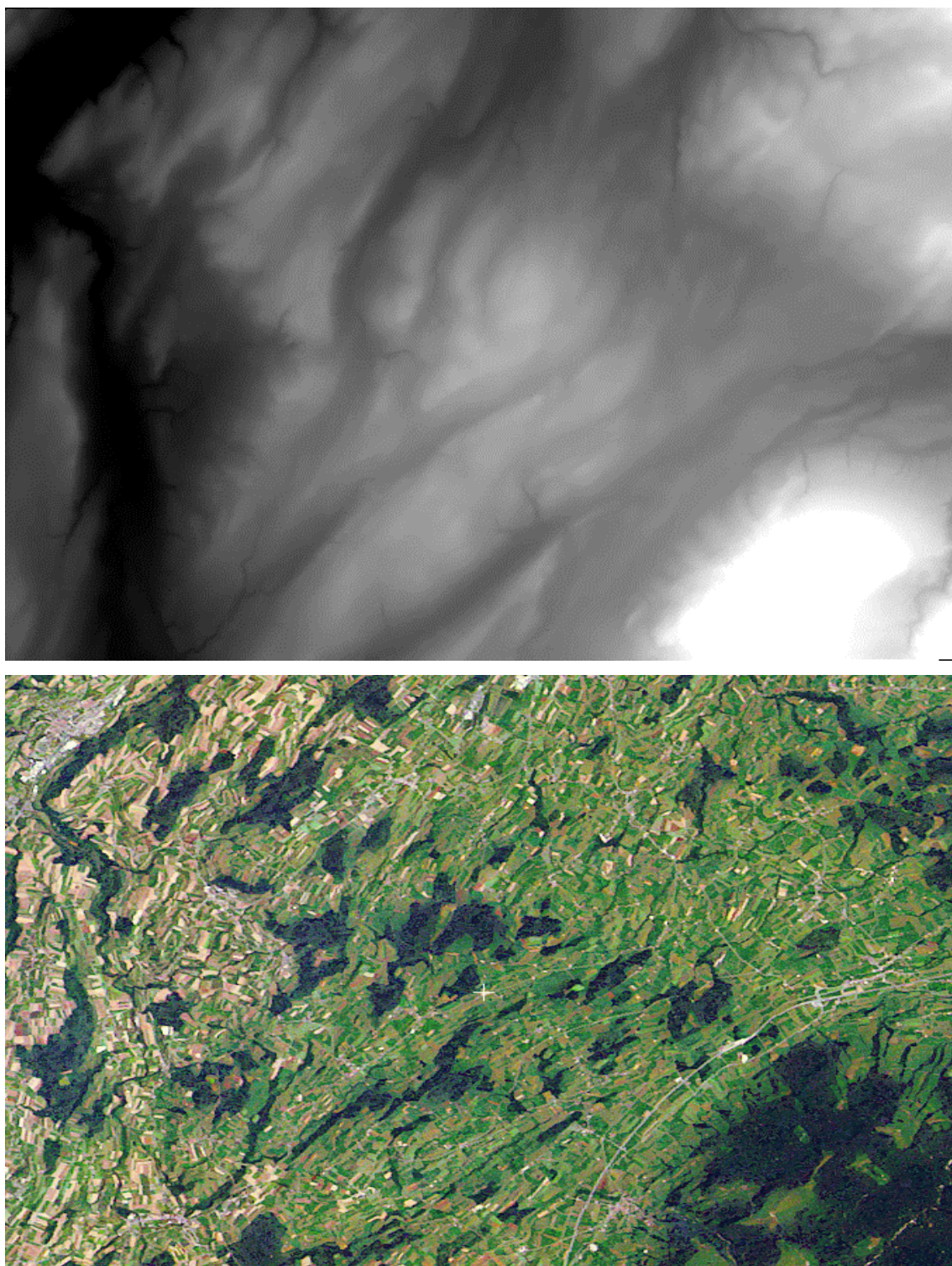
Fig. B2 DTM and Landsat TM scene view on the Swiss test site. © ESA 1990-94/ NPOC/ Eurimage/ Bundesamt für Landestopographie
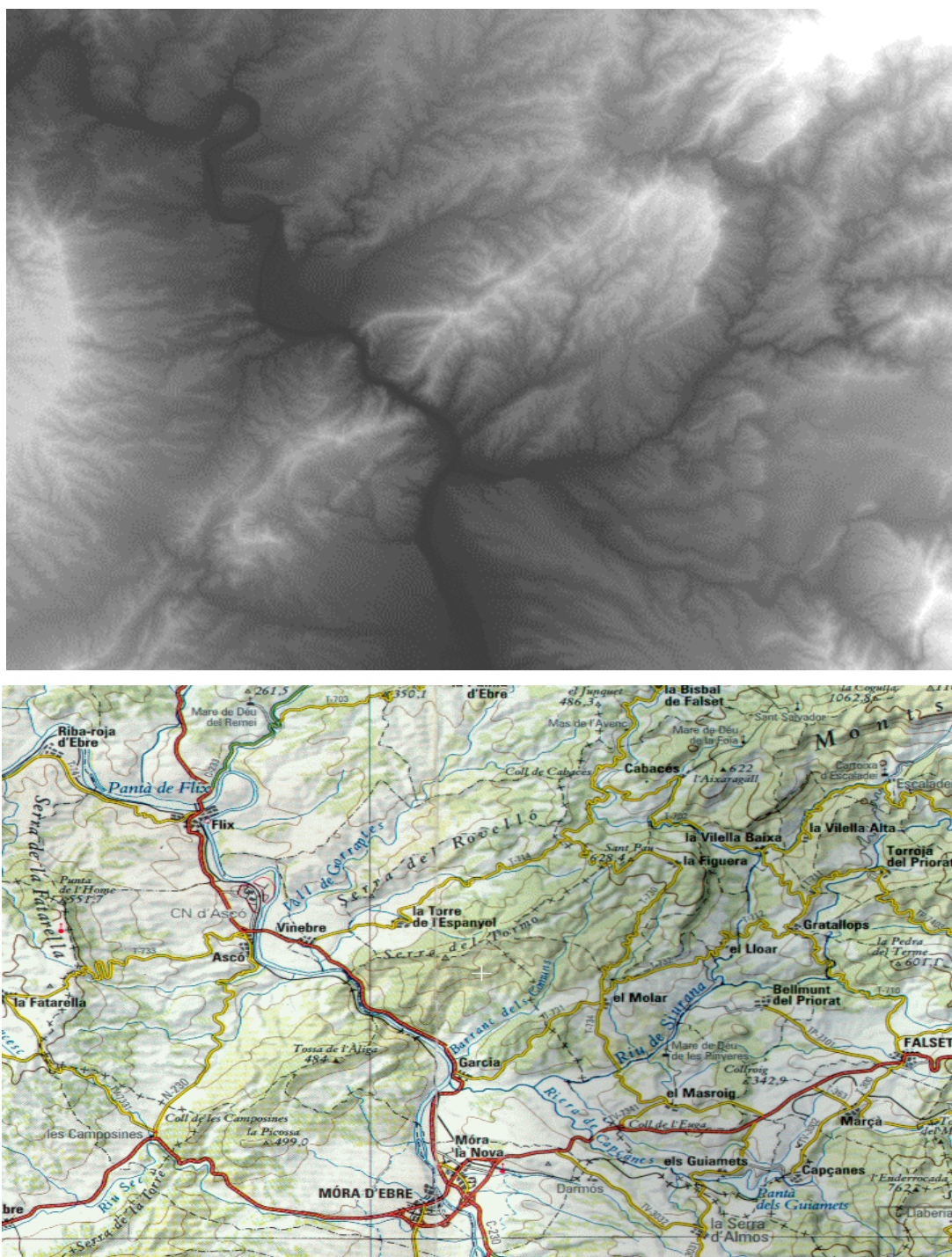
Fig. B3 Site Spain II, DTM and topographic map 1:250'000 © Institut Cartographic de Catalunya

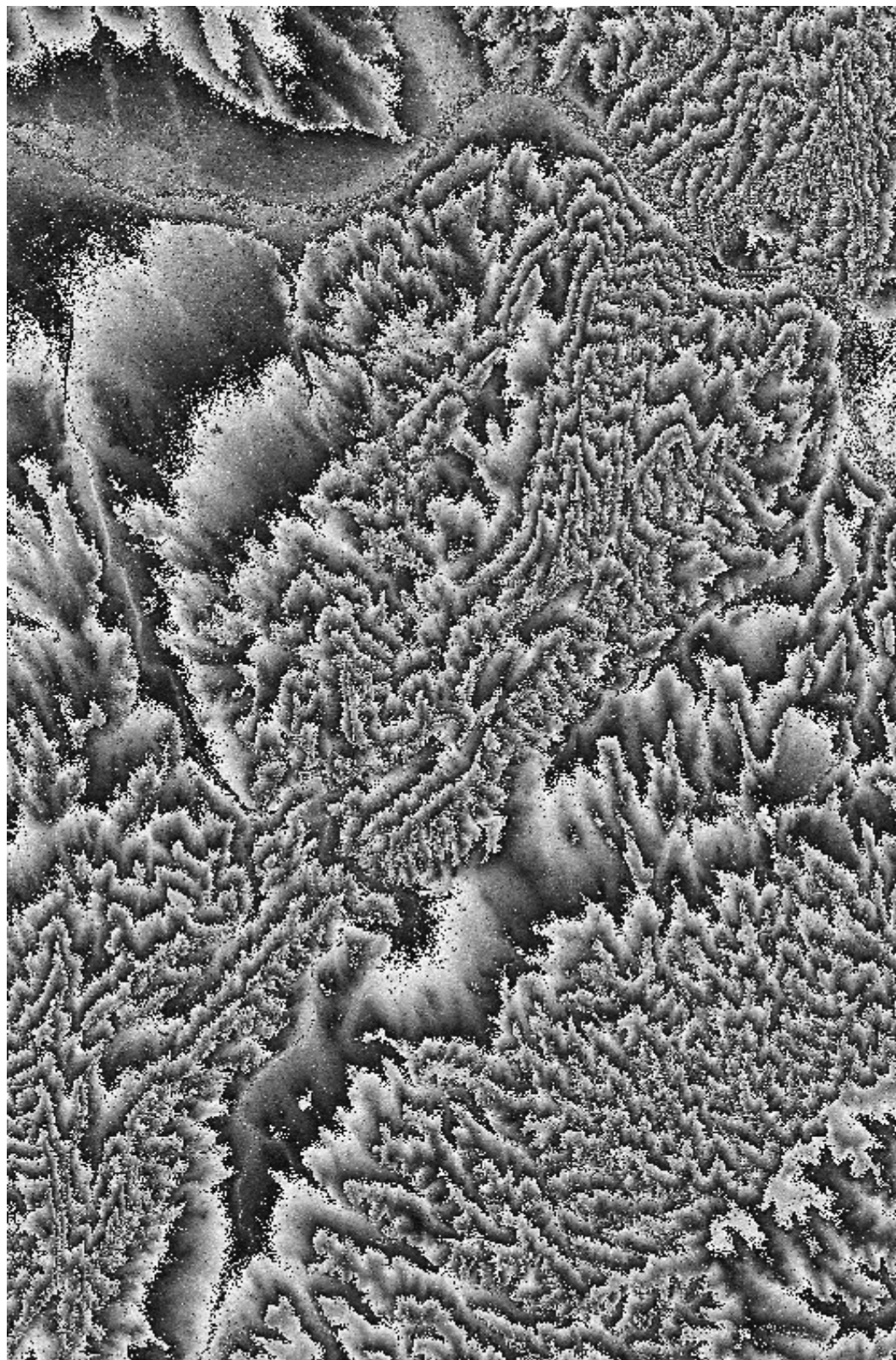**B2 Example: InSAR data and unwrapping result of test site Spain II**

Fig. B4 Ellipsoid flattened interferogram subset of site Spain II. The subset corresponds to the lower left quarter of the DTM. A single fringe line equals a height difference of approximately 60m. Despite the rather short baseline, the additive noise component is well visible all over the site, resulting in a high amount of residues. Multiplicative effects like volume scattering and foreshortening in the mountainous part of the site corrupt the fringe borders, which vanish in part and must be restored during the filtering operation in order to make unwrapping feasible also in the steeper part.
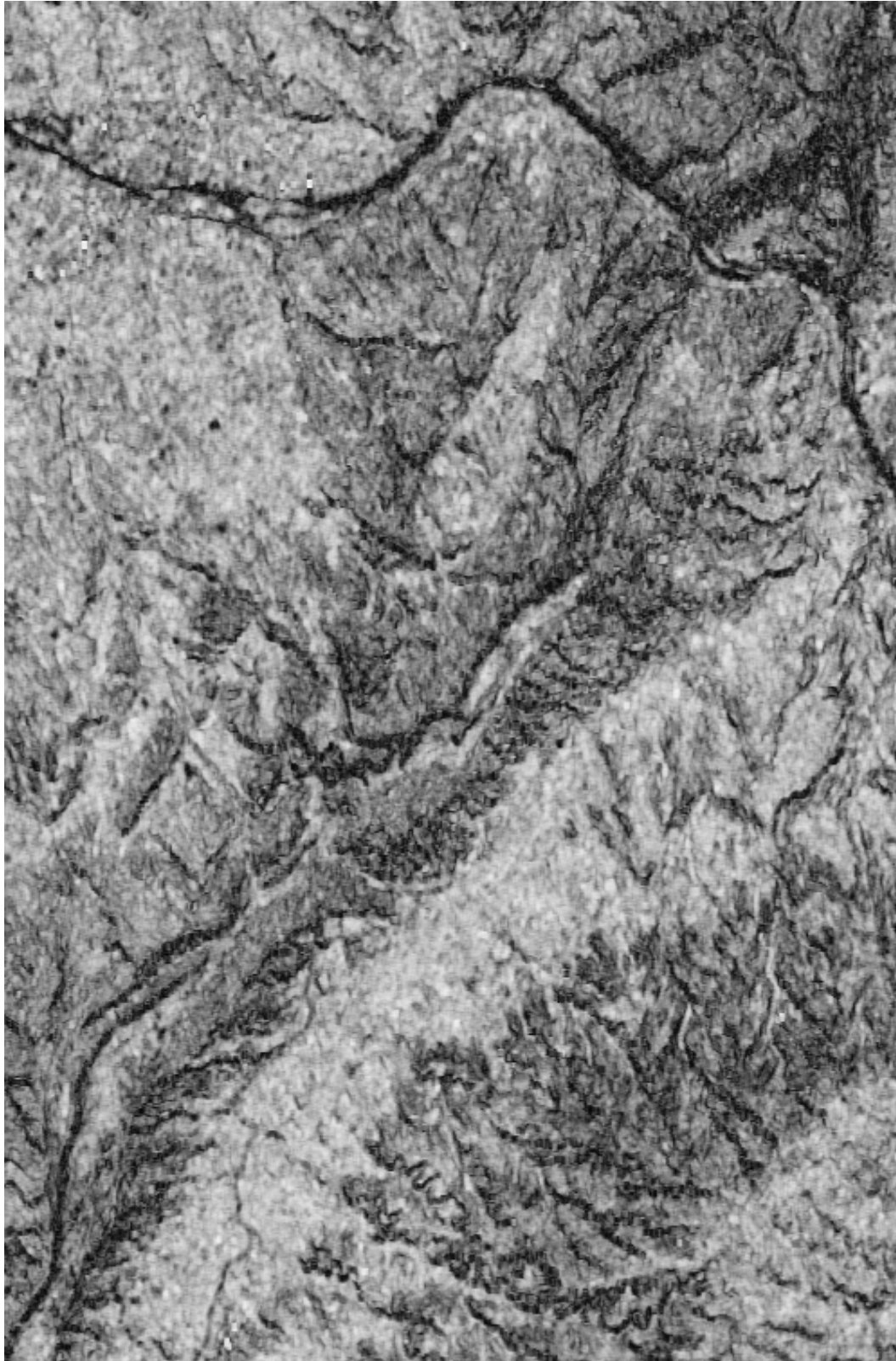
Fig. B5 Calculated coherence of the site. The values varied between 0.9 and 0.05. As expected, the highest values are found in the flat parts of the site, while the lowest values are found at the river and in some steep areas. Spatial decorrelation due to the combination of topography and vegetation led in large parts to a coherence decrease, indicated by values between 0.3 and 0.5. According to the introduced interferometric noise model, the phase are corrupted in those areas both additively and multiplicatively.
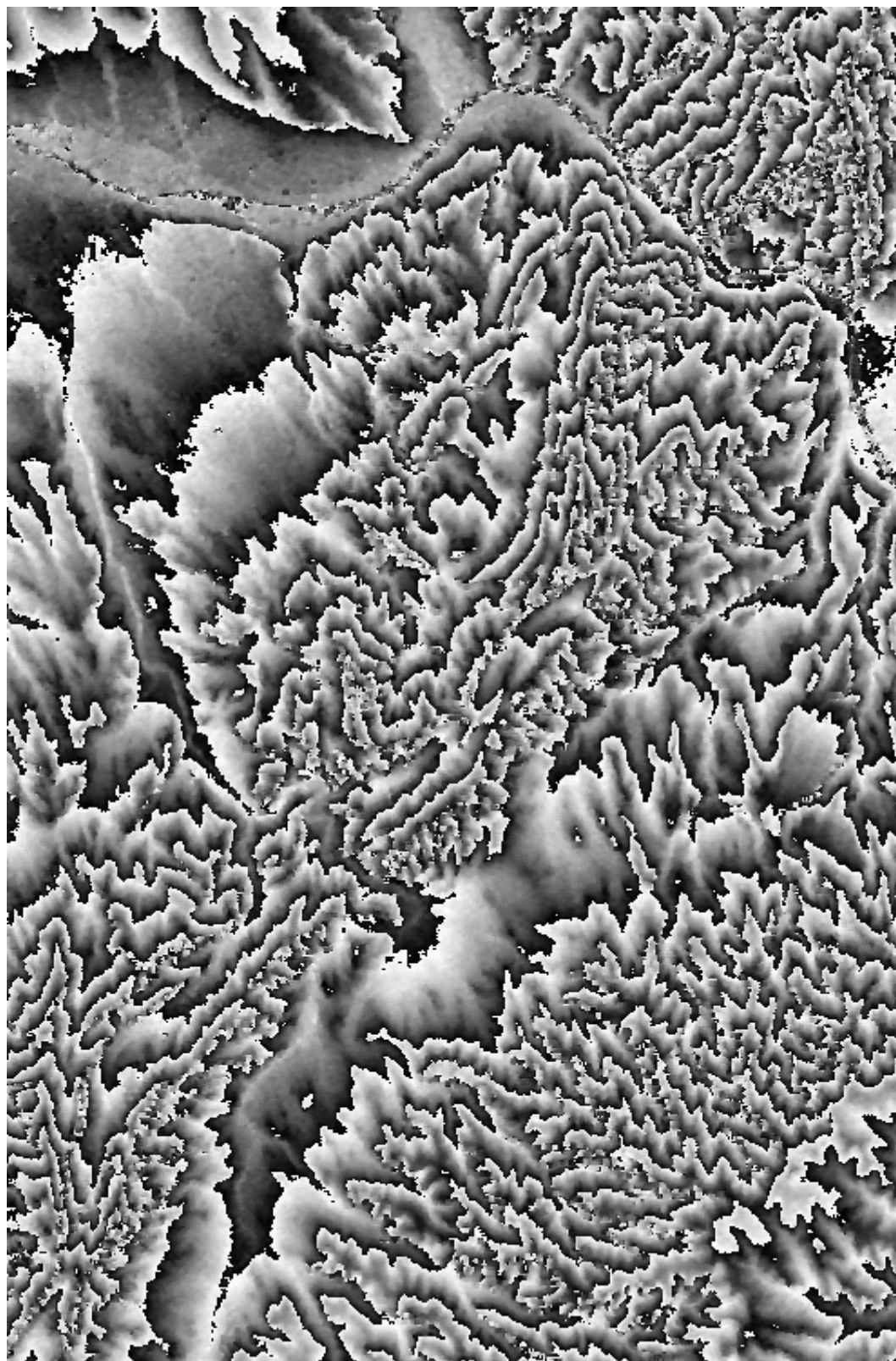
Fig. B6 Filtered interferogram. The shortcoming of common filtering approaches becomes visible. Due to the incomplete noise model only the additional noise component has been removed to a great extent, while the multiplicative part due to spatial decorrelation is erroneously treated and therefore corrupts large parts of the site. The result is a fringe border corruption, which strongly affected phase unwrapping. Except the completely decorrelated areas, the corruption in many areas can be removed, if adequate filtering is performed.
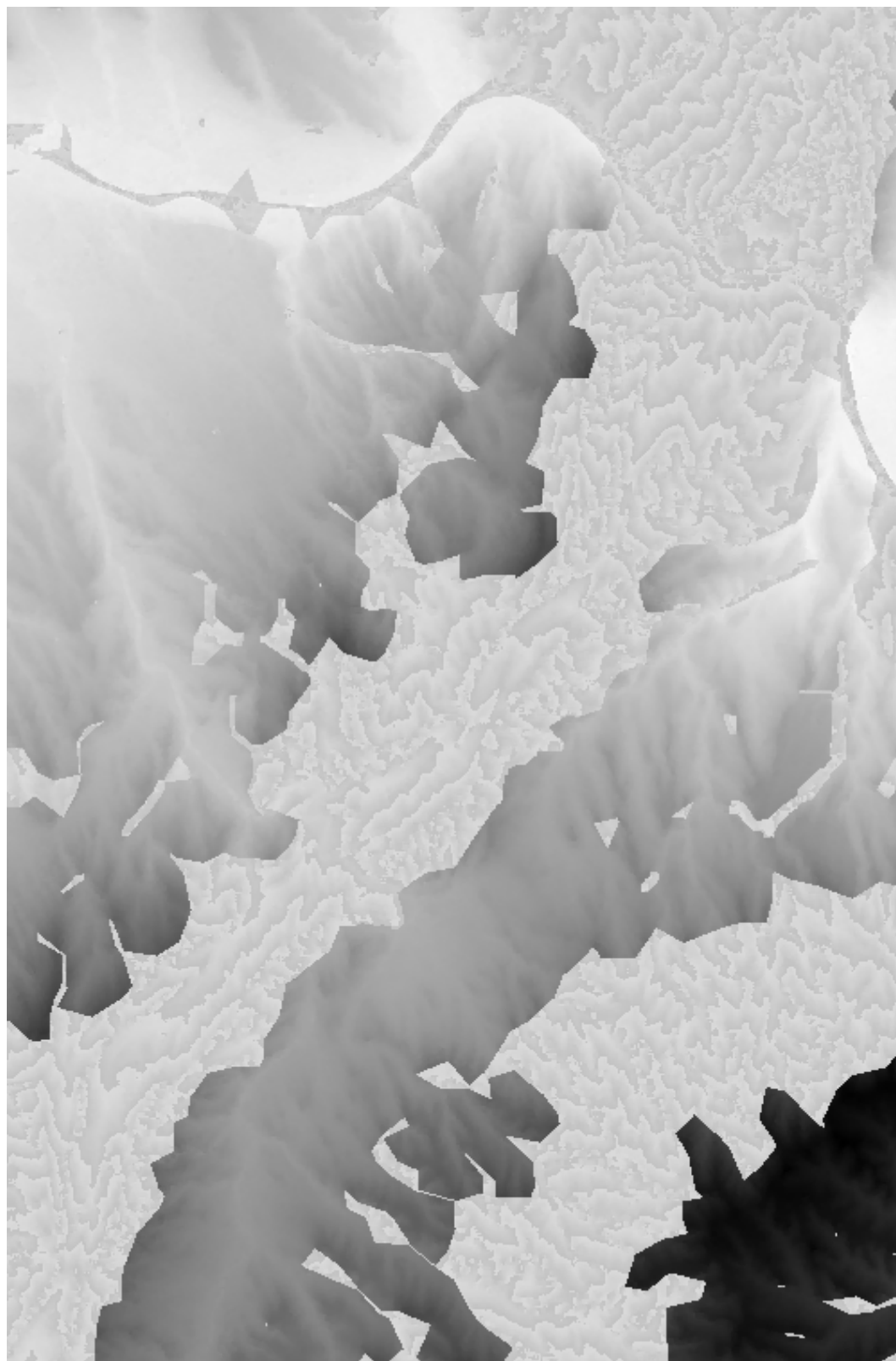
Fig. B7 Phase unwrapping result. After applying the branch cut algorithm for the unwrapping of the filtered interferogram (Fig. B6), large parts of the site remained inaccessible, as only the highly coherent part could be unwrapped. As the residue dense areas could not be accessed, the result is split in three unconnected regions, which were of little use for further DTM generation.
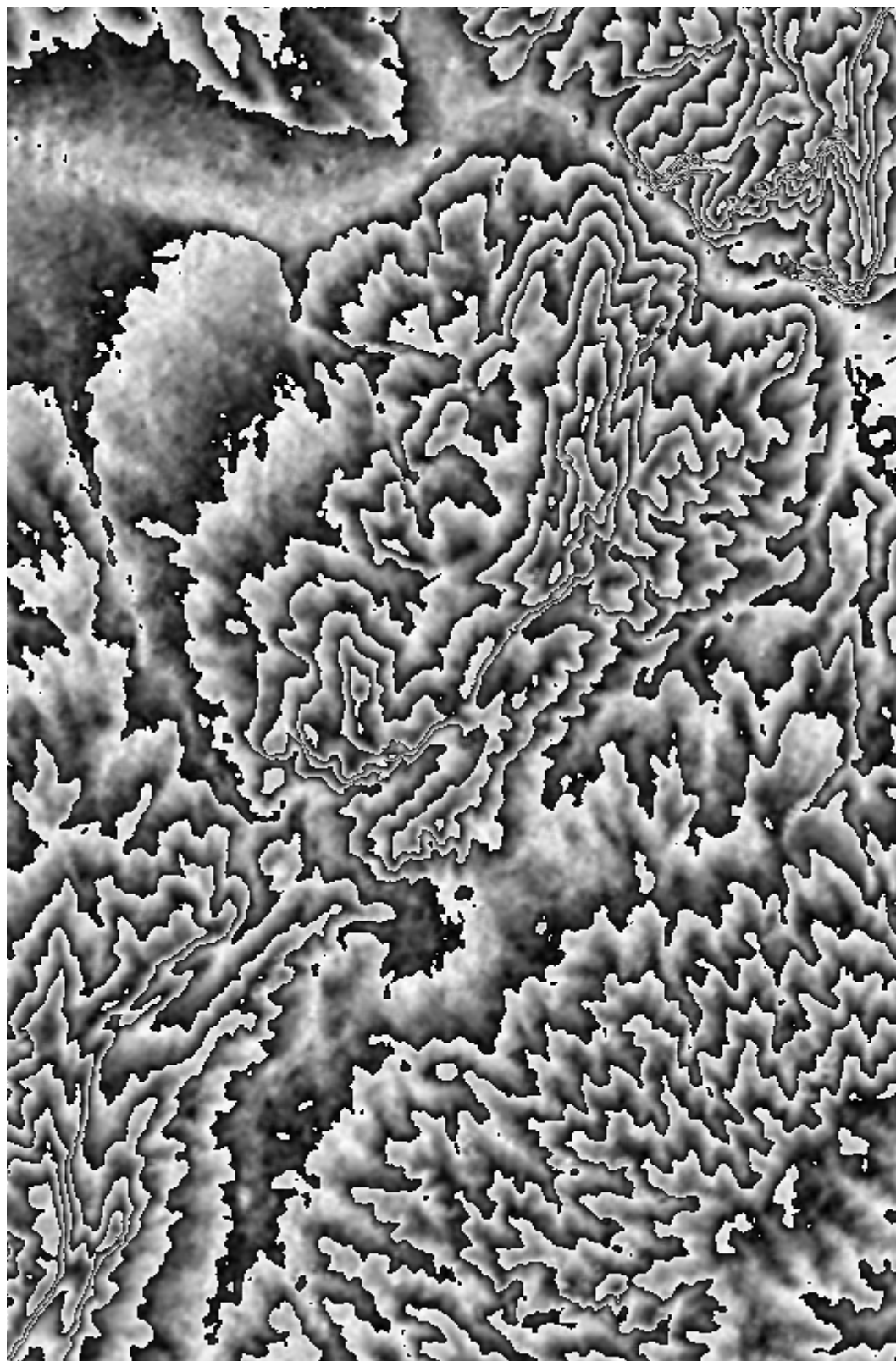
Fig. B8 Simulation derived from the SPOT DTM. Due to the interpolation required to derive the raster, the simulation displays the topography of site less detailed than the interferogram, but offered an approximation in the steeper part of the site, where InSAR failed. In order to prevent an error leakage from the simulation into the interferometric measurements, it has been used only for the constrained unwrapping and the derivation of the parameters for the first filtering iteration.
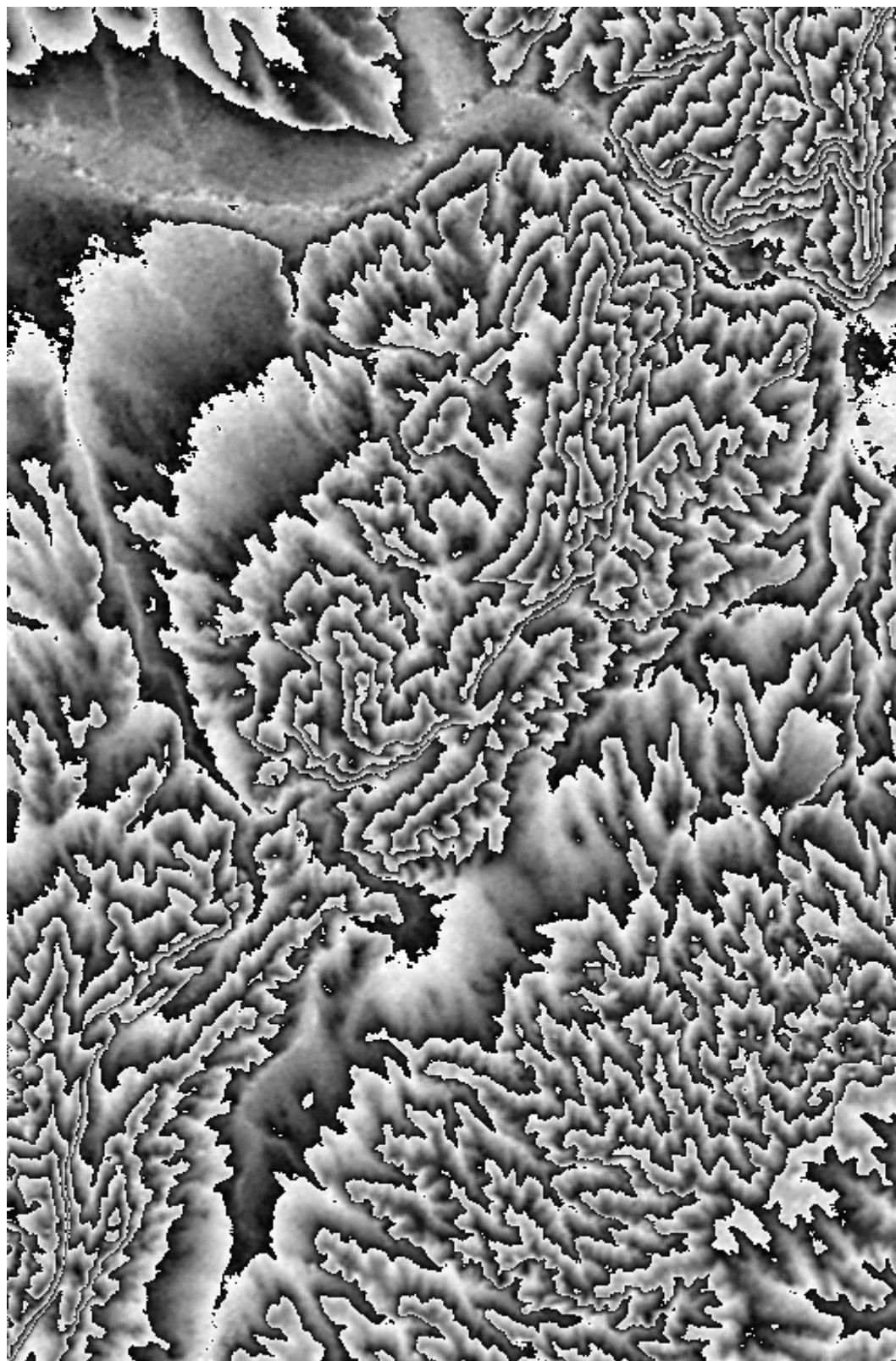
A13

Fig. B9 Result after the Wiener filtering. The unwrapped phases are wrapped in the 2π interval in order to facilitate the comparison with the original interferogram. Because of the noise adaptation of the Wiener filter, the phase slope is well preserved in the highly coherent regions, while the fringe borders are recovered from the noise corruption in the steeper part of the site. Note that due to the estimation, the filtering result corresponds closely to the original interferogram, although the simulation is in part of a completely different shape.
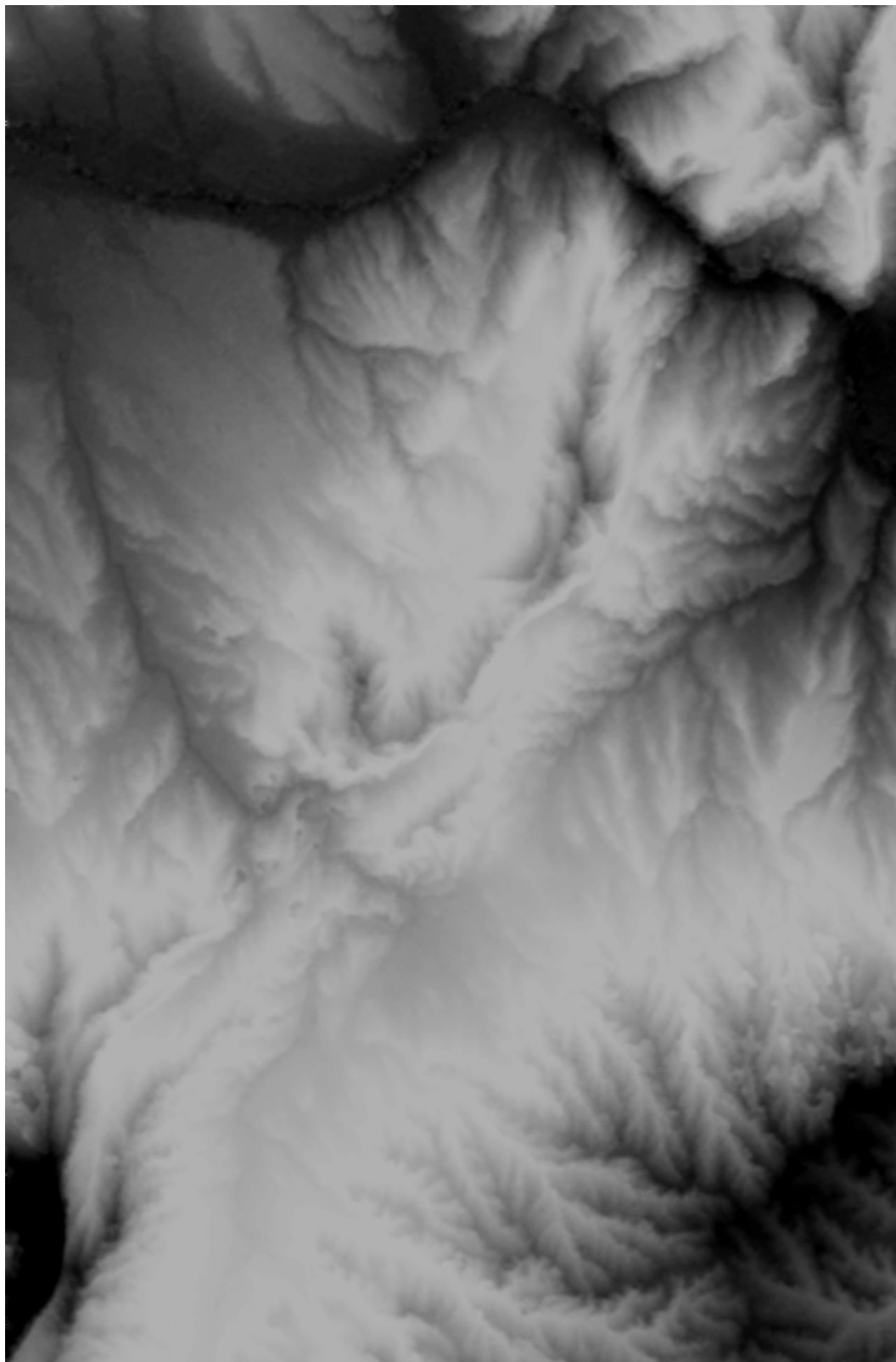
A14

Fig. B10 The unwrapping result. As the corruption has been treated with the Wiener estimation, a complete solution could be achieved for the site. The solution has been achieved in three iterations, in which the simulation was only used during the first one. As the algorithm requires in contrast to the branch cut algorithm no residue detection and clustering, the solution is achieved completely automatically.

A15

C Projects

C 1 EU concerted action ORFEAS
Optical Radar Fusion for Environmental Applications

Period: 01.03.1996 – 30.05.1998

Partner Universities

Aristotele University of Thessaloniki (GR); Institut Cartographic de Catalunya (ESP); TU Graz (AUT); Politechnico di Milano (IT); ETH Zurich (CH)

Abstract

Monitoring environmental changes is an issue which is not only rapidly gaining importance, as awareness of its value and demand for it are increasing, but is also becoming more complicated and challenging when considering the modern, accelerated rate of environmental change. Supported by recent research advancements, photogrammetry and radargrammetry have established themselves as key methodologies for monitoring the environment, as they provide an abundance of data and updating abilities. In addition to sharing objectives, photogrammetry and interferometry are quite compatible and therefore can both benefit from mutual cooperation.

To improve the effectiveness of research for environmental monitoring within these two disciplines, and to acquire a better perspective of European needs in this matter, this concerted action for coordination of research was performed on the issue of modelling and monitoring the environment with digital elevation model generation and geocoded image production of an test area in Catalonia/Spain by using radar and electrooptical sensors. Ways of combination of these two complementing techniques will be identified by comparing their performance in terms of accuracy, investigating their synergetic use and identifying the potential for transferring

A16

methodologies between them in order to optimize environmental monitoring in an European context.

Research Interest

DTM generation

The generation of digital terrain models (DTM) is an important issue of satellite remote sensing and is needed in many applications. Reliable elevation information is inevitable for applications like geocoded image production and is substantial for environmental and land system monitoring and management (e.g. within a GIS). Traditionally the DTM is derived stereoscopically from an optical sensor image pair (Fig. C1). With the ERS mission, SAR data became available regularly, which paved the way for a new technique for DTM generation, the SAR interferometry (InSAR) (Fig. C2). Today, both satellite stereoscopy and interferometry exist in parallel and are applied independently of each other, although several synergies to overcome the limitations of each technique can be identified.

This project focused especially on synergetic effects between optical and Radar sensors, in order to improve satellite DTM accuracy. As both techniques for DTM generation suffer from distinct limitations, the use of independent data during each DTM processing and for DTM fusion will help to overcome the single sensor problematic and result in DEMs of higher accuracy.
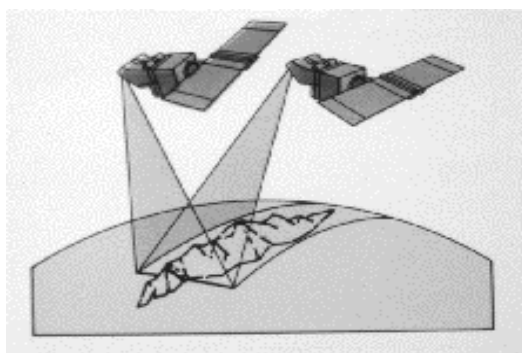

Fig. C1 SPOT stereo viewing scheme. The images are taken from opposite viewing directions.
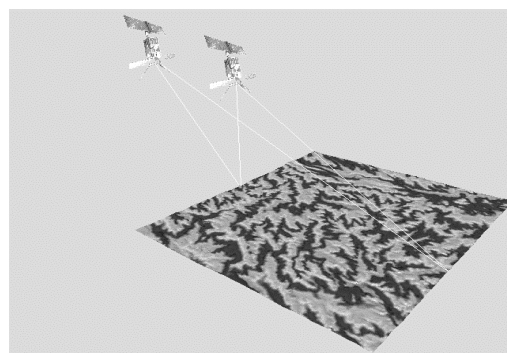

Fig. C2 InSAR viewing scheme. Both images are taken from slightly different positions

Data Fusion

In order to take advantage of the independent measurements an estimation of height errors is needed for any fusion process, which wants to profit from both sensors. For that purpose a

measure for the reliability of each point, which is directly related to the measurement error has been developed. This measure is used to define a weight, according to which the different DTMs can be fused pointwise.

By fusing the DTMs according to these weights, the resulting DTM improves in respect to general accuracy, reduction of measurement holes and outliers (Fig. C3, C4).
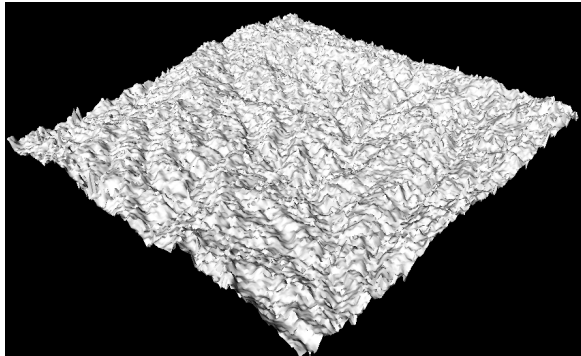

Fig. C3 Stereo-optical DTM. Height errors, appearing as spikes, reduce the usability of the DTM
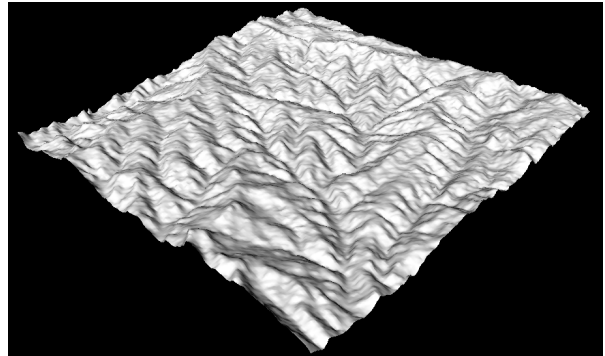
Fig. C4 DTM after the fusion. The errors are replaced by valid measurements from the InSAR counterpart

C2 KTI Project CIRSTEN

Combined Remote Sensing Natural Disaster Monitoring

Period: 1.1.2000 - 1.5.2002

Project Partner:

Gamma Remote Sensing, Institute of Geodesy and Photogrammetry, ETH Zurich

Abstract

Recent natural disasters like landslides, flooding or forest fires have shown the need for natural risk management not only in Switzerland but also in whole Europe, as they endanger directly public health and cause severe damages on the national economy. In order to improve the efficiency of existing hazard management practices, we propose a natural hazard and disaster monitoring service for sensitive areas. The project addresses the localisation and mapping of natural hazards using SAR and optical data from earth observation satellites. Remote sensing data offer a regular information for prevention and damage assessment of natural disasters and provide large scale environmental monitoring and updating capabilities. The results are stored as information layers in a geographic information system (GIS), which enables a user friendly access and compatibility with pre-existing databases. The final product is a fast, inexpensive and ready to use service for the prevention and management of natural hazards.

Research Interest

DTM generation

Stereo-optical DTM generation provides the elevation data needed, as stereoscopy is robust and accurate in most types of terrain. The high degree of automatisation and the little terrain dependency of the accuracy make stereo-optical DTM generation the DTM source of choice. During this project, we will test and adjust our matching algorithms to achieve the highest possible

accuracy, as an accurate DTM is essential for the correct georeferencing of the other information layers. We will focus on the reduction of the amount of mismatched points (appearing as spikes in the DTM), which hinder the correct cross-correlation determination between the SAR amplitude image and the simulated SAR image from the DTM, the key step for the georeferencing of the SAR images.

SPOT is the preferred satellite sensor for optical imagery at the moment and offers a multi-time data coverage of the whole world. This redundancy offers the opportunity to select appropriate stereo pairs (e.g. little cloud coverage) for DTM generation over the affected area.

SAR interferometry is expected to provide additional DTM information, which will be fused with the stereo data.

Data Integration

Both SAR change detection and stereo-optical DTM generation are mature and already proven techniques. A central scientific goal of the project will is the creation of an interface between the data, which takes advantage of the positive properties of optical and SAR data. Optical and SAR data synergy is scarcely used today; therefore, a combined use of this data will be established and evaluated during the project (Fig. C5).

Fig. C5 Storm Lothar forest damage at Murtensee (CH). Damages (red) have been detected by SAR coherence change due to the deforestation.

Curriculum Vitae

Dipl.-Ing. Marc Wolfgang Honikel
Institute for Geodesy and Photogrammetry
ETH Zürich
8093 Zürich

Personal
Date of birth: February 23rd, 1969
Nationality: German

Formation
1989-91   Mechanical Engineering at TU München
Degree: Bachelor I
1991-93   Electrical Engineering at TU München
Degree: Bachelor
1993-97   Electrical Engineering at TH Karlsruhe
Degree: Master
Diploma Thesis: „Evaluation and Further Improvement of a Novelty Detection Filter" at Fraunhofer - Institut für Informations- und Datenverarbeitung (IITB), Karlsruhe
1997-2002   PhD student at the Institute for Geodesy and Photogrammetry at ETH Zürich
Ph.D. Thesis: Fusion of spaceborne stereo-optical and interferometric SAR data for digital terrain model generation

Projects
ORFEAS (1997-99):   EU concerted action „Optical Radar Fusion for Environmental Applications"
Responsibility: Project Scientist
CIRSTEN (2000-02):   Swiss KTI project „Combined Remote Sensing Natural Disaster Monitoring"
Responsibility: Principal Investigator

Award
Young author's award of the International Society of Photogrammetry and Remote Sensing (ISPRS). Awarded by Commission I for the publication „Wiener Based Interferometric Signature Reconstruction", published in the proceedings of the XIX ISPRS Congress, Amsterdam, 2000.

Publications
10 publications at conferences and journals since 1997. A complete list of publications is available at: http://www.photogrammetry.ethz.ch/research/orfeas/pub/publications.html